

N O T I C E

THIS DOCUMENT HAS BEEN REPRODUCED FROM
MICROFICHE. ALTHOUGH IT IS RECOGNIZED THAT
CERTAIN PORTIONS ARE ILLEGIBLE, IT IS BEING RELEASED
IN THE INTEREST OF MAKING AVAILABLE AS MUCH
INFORMATION AS POSSIBLE

(NASA-CR-165050) THE SEISMOTECTONICS OF
PLATE BOUNDARIES Final Report, 1 Nov. 1973
- 30 Jun. 1981 (California Univ., San Diego,
La Jolla.) 85 p HC A01/MF A01 CSCI 08G

N82-14690

Unclass

G3/46 08576

THE SEISMOTECTONICS OF PLATE BOUNDARIES

J. Berger, J. N. Brune, J. Goodkind*,
F. Wyatt, D. C. Agnew

Institute of Geophysics and Planetary Physics
*Physics Department
University of California, San Diego
La Jolla, California

and

C. Beaumont

Department of Oceanography
Dalhousie University
Halifax, Nova Scotia



FINAL REPORT

NGR 05-009-246
11/01/73 - 06/30/81

National Aeronautics and Space Administration
David Smith, Technical Officer
Goddard Space Flight Center
Greenbelt, Maryland 20771

THE SEISMOTECTONICS OF PLATE BOUNDARIES

J. Berger, J. N. Brune, J. Goodkind*,
F. Wyatt, D. C. Agnew

Institute of Geophysics and Planetary Physics
*Physics Department
University of California, San Diego
La Jolla, California

and

C. Beaumont

Department of Oceanography
Dalhousie University
Halifax, Nova Scotia

FINAL REPORT

NGR 05-009-246
11/01/73 - 06/30/81

National Aeronautics and Space Administration
David Smith, Technical Officer
Goddard Space Flight Center
Greenbelt, Maryland 20771

TABLE OF CONTENTS

	Page
Abstract	3
1.0 Introduction to Report	4
2.0 Seismotectonics of Southern California: Piñon Flat Observatory	6
2.1 Seismic Setting	10
2.2 Instrumentation	15
2.2.1 Optical Anchor	22
2.3 Results	29
3.0 Seismicity Studies Related to the Gulf of California	44
4.0 Development of the Superconducting Gravimeter	47
5.0 Earth Tide Studies	54
5.1 The Ocean Tides	56
5.2 Strain Tides	60
5.3 Elastic Structure — Local Departures from Radial Symmetry	68
References	80
Bibliography: List of papers supported by this grant	83

ABSTRACT

This report describes the research conducted over the past seven years by three groups at the University of California, San Diego, on the seismotectonics of plate boundaries. The project involved both instrumental development and an observational program designed to study various aspects of the seismotectonics of southern California and the northern Gulf of California. Dr. Jon Berger and Frank Wyatt were primarily involved with the development of the Cecil and Ida Green Piñon Flat Observatory. Dr. James N. Brune and his group worked on the interpretation of the seismotectonics of southern California and Baja California. Dr. John Goodkind and Dr. Richard Warburton further developed a unique superconducting gravimeter and were supported under this program for the deployment and operation of these instruments at several sites. Each of these three sub-programs are reviewed separately in Sections 2, 3, and 4 of this report while Section 5 discusses the work of Dr. Duncan Agnew and Dr. Christopher Beaumont on earth tides.

1.0 Introduction to the Report

This project, involving three groups at the University of California, San Diego, was basically an instrumental and observational program designed to increase our knowledge of the seismotectonics of plate boundaries. Dr. Jon Berger and Mr. Frank Wyatt were primarily involved with the development of the Cecil and Ida Green Piñon Flat Observatory (PFO). Dr. James N. Brune and his group worked on the interpretation of the seismotectonics of southern California and Baja California. Dr. John Goodkind and Dr. Richard Warburton further developed a unique superconducting gravimeter and were supported under this program for the deployment and operation of these instruments at several sites. Each of these three sub-programs will be reviewed separately in Sections 2, 3, and 4 of this report while Section 5 discusses the work of Dr. Duncan Agnew and Dr. Chris Beaumont on earth tides.

Each of these projects was, in different ways, involved in the support of NASA's study of the seismotectonics of the San Andreas Fault System.

The general tectonics of the San Andreas Fault (SAF) system, and the basic mechanics of faulting and earthquakes, have been fairly well established in recent years. The SAF forms part of the boundary between the Pacific plate and the North American plate. Faulting occurs as a result of shearing between these plates as they drift past one another upon a weak, lubricating asthenosphere at a depth of about 50-100 km. The frictional resistance resulting from the pressure of one side of the fault against the other causes the fault to "chatter" on a large scale. Strain energy is stored while the fault is locked and is released when slip occurs.

Slip along the fault which relieves these stresses can occur seismically or aseismically. Slow slip (creep) does not produce earthquakes under normal circumstances. However, if the slip proceeds at a speed comparable with the velocity of propagation of elastic waves then seismic waves are excited and an earthquake occurs. Since earthquakes are highly dangerous to life and property, it is essential to understand the underlying differences between these two modes of strain release. The estimation of seismic risk, the prediction of earthquakes and ultimately the prevention of disastrous events all hinge on a thorough understanding of fault motion mechanisms. Specifically, we must determine the processes by which: 1) strain energy is stored in the earth preceding large earthquakes, and 2) strain energy is released by creep.

Our studies have involved monitoring strain accumulation of some southern California faults which form at the plate boundaries. Here we differentiate between 1) the high seismic risk surficial creep, or creep at depth where the surficial region is locked; and 2) the low seismic risk creep that occurs at low stress throughout the plate boundary.

The major uncertainties that remain in our mechanical picture of the plate boundary are:

On a large scale,

1. What are the driving forces responsible for the plate motions and how are they distributed in space and time?
2. What are the current rates of relative plate motion both across San Andreas Fault (SAF) and at the centers of the plates? Do the motions agree with one another and with the geological rate of 5-6 cm/yr?
3. What is the tectonic relationship between fault motion along the SAF in California and the opening of the Gulf of California? Is this motion occurring predominantly seismically or aseismically?

And on a smaller scale,

4. If there is a significant difference between the motions of the plate centers and the motions at the boundary, where does the plate distortion occur? Is it near the fault, distributed throughout the plate, or on the fault zones?
5. How is aseismic slip accomplished below the zone of earthquakes? Is it steady or episodic? Does a significant part of the energy in large earthquakes come from this zone? Are large earthquakes triggered by premonitory deformation in this zone?

6. Is there a significant amount of aseismic movement accompanying earthquakes and if so how can we measure the total moment?
7. Are there premonitory changes in the elastic properties in earthquake source regions as the dilatancy models suggest, and can these changes be used to predict earthquakes?

Recent development of theories of plate tectonics point to the Gulf of California as one of the most important areas in which to study the mechanism and characteristics of plate boundaries and ocean-floor spreading process. The Gulf is underlain by an oceanic ridge and is itself the result of sea-floor spreading processes related to this ridge. Nowhere else in the world is such an area so easily accessible to study with detailed land-based seismic and geodetic arrays. At the same time, the Gulf's evolution has progressed to the point where its spreading processes are probably very similar to those of ridges in the centers of the major ocean basins. The tectonic history of the Gulf of California is intimately related to that of the San Andreas fault system and full understanding of this system demands a better knowledge of the mechanics of the ocean-floor processes at its two extremities.

In the sections that follow, we will describe the activities supported by the grant under the headings:

- Section 2. The seismotectonics of southern California — Piñon Flat Observatory.
- Section 3. Seismicity studies related to the Gulf of California.
- Section 4. Development of the superconducting gravimeter.
- Section 5. Earth tide studies.

2.0 The Seismotectonics of Southern California: Piñon Flat Observatory

There are several distinct methods of investigating the seismo-tectonics of the earth's crust. Traditionally, seismic studies have perhaps yielded the most results. Here, naturally occurring earthquakes are the sources used to investigate both the earthquake process itself and the general tectonic fabric. Recently, geodetic surveys have been used rather extensively in California to study the spatial and temporal pattern of strain accumulation in the crust. If the crust is an elastic material, the strain field will be simply related to the stress field and that in turn is a key factor in understanding the plate motions in general and the earthquake process in particular. A third method of investigation is the development of continuous recording instrumentation of high sensitivity and stability to measure the surface deformations directly.

This element of the NASA supported program involved the development and operation of precision instrumentation to monitor crustal deformations. For Dr. Berger's group, it represented a continuation of work begun at Camp Elliott, near La Jolla, in the late sixties on the laser strainmeter (Berger and Lovberg, 1969). In 1971, we began to deploy this type of instrumentation in a more geophysically interesting site with three major goals in mind:

1. The development of new instrumentation to measure crustal dynamics.
2. The establishment of a reference station consisting of the most stable and sensitive instrumentation available in an attempt to determine true ground deformation rates and thus improve the limits of detectability of anomalous tectonic behavior.
3. The monitoring of the tectonic and seismic activity near PFO — an area of unusually high seismic activity.

These goals are quite fundamental to our understanding of the dynamics of the faulting process. Further, the specific program embarked upon and supported by NASA is a necessary element in the interpretation of geodetic measurements of crustal deformation. While the scale of the measurements (~ 1 km) is small by geodetic standards, the problems addressed are common to any observations of crustal dynamics. The goal of monitoring stress changes in the earth's crust is currently limited by the noise in the observations—noise which tends to mask tectonic and seismic effects. Our efforts are directed towards identifying, reducing and, when possible, eliminating some of these noise sources in order to examine the underlying signals of interest.

It is perhaps worth reviewing the relevance of this research to NASA's goals in Crustal Dynamics and related studies. NASA's involvement in this subject arises from the techniques they have developed to measure the position of points on the earth's surface relative to earth satellites and extragalactic sources. The research goals of these studies relate to seismic and tectonic activity, polar motion and rotation rate.

Our goals at PFO are directed towards the understanding of both seismic and tectonic motions and their interconnections. We are pursuing an observation program that involves the development and testing of new instrumentation and measurement techniques. We are observing strain, tilt and gravity continuously with what we believe are the most sensitive and stable instruments currently available. This program has, over the past few years, provided consistent upper limits to the spectrum of crustal deformations occurring (at least) in the area of the observatory. This is an area of high tectonic activity, high seismic risk, and is very likely typical of southern California.

While our measurements are made over rather short (by NASA standards) baselines, the sensitivity and stability is rather high. Figure 2.1 compares the capabilities of observatory measurements, land based EDM (Electromagnetic Distance Measurement) techniques (such as utilized by the USGS in their trilateration networks), and extraterrestrial surveying techniques. The trade off between baselength and resolution is obvious. But what is not obvious is the spatial aliasing and temporal aliasing to which long baseline, infrequent measurements might be subject.

In the case of the USGS trilateration networks (see Savage *et al.*, 1981), the survey areas are irregular figures with typical dimensions of 100 km. (The Palmdale net is a notable

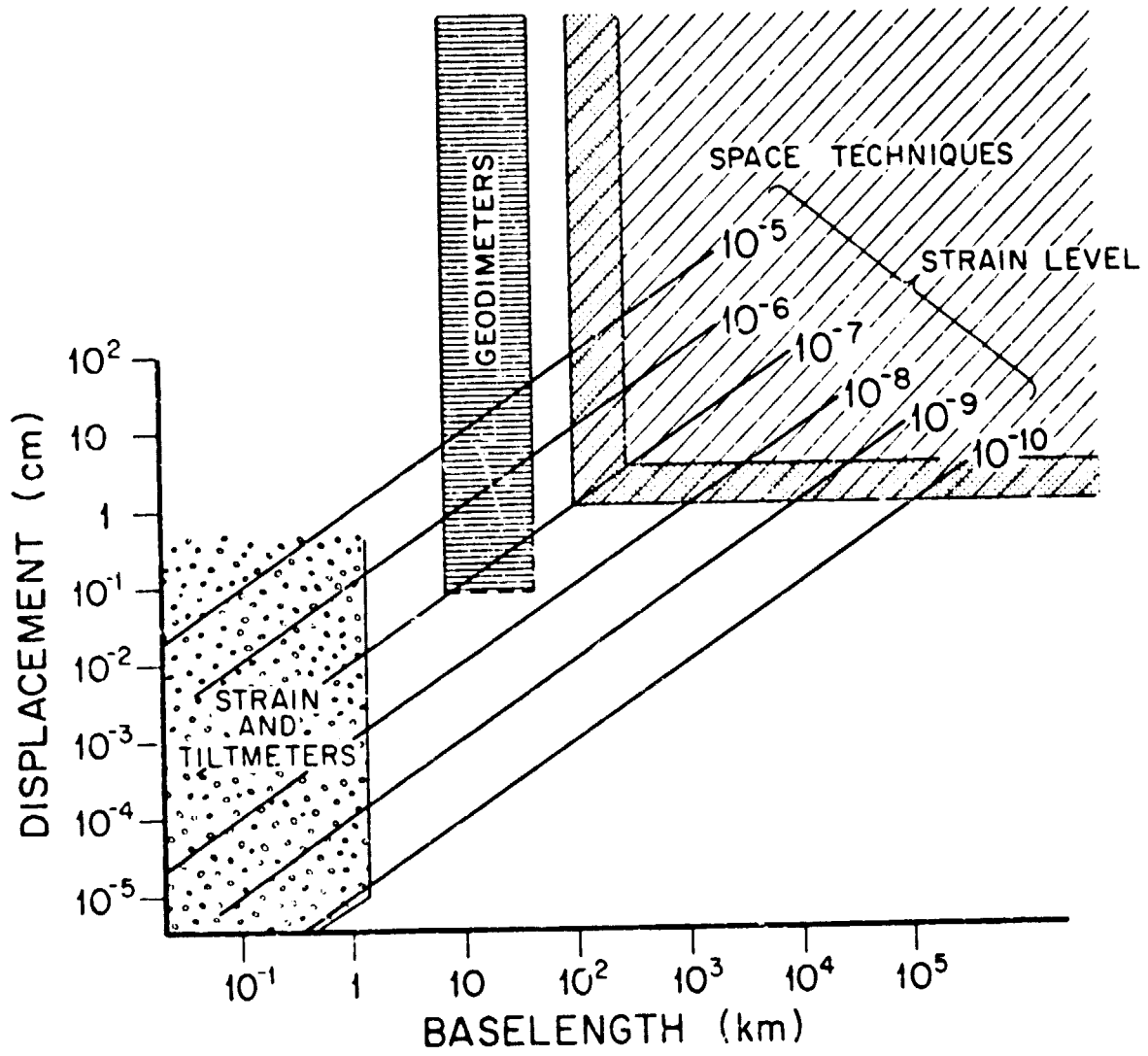


Figure 2.1 A comparison of strain measuring techniques

exception.) The time taken to survey a single network completely is usually many weeks. The data are reduced under the assumption of spatially uniform strain and constant strain rate (Prescott *et al.*, 1979). Whether the tectonic strain fields approximate the assumptions of spatial uniformity and temporal rate constancy has yet to be determined, but the impact of these assumptions to NASA's Crustal Dynamics observational program is considerable.

What strain rates should we expect to see in such a tectonically active area as southern California? The rather substantial body of trilateration data collected in this area over the past seven years or so (Savage *et al.*, 1981) clearly indicates that the normal secular strain rates (normal over this period at least) are $1-2 \times 10^{-7}/\text{yr}$. The NASA SAFE experiment monitoring the length of a line from Otay Mountain near San Diego to Quincy, California observed on the average a strain rate of $10^{-7}/\text{yr}$ over that 900 km distance (Smith, 1980). Our observations indicate that on a 1 km baselength the same result is obtained. Crudely, then, the strain rates of about $10^{-7}/\text{yr}$ are observed over baselines of 1 km to 1000 km at least in this area.

Fluctuations about these average strain rates might be expected to occur if the tectonic stress is not accumulating uniformly in time. Obviously, the occurrence of earthquakes introduce sudden perturbations into the ambient stress field if only due to the local release of strain energy. If an earthquake occurs, roughly speaking, the strain change will be proportional to the stress drop.

$$\Delta\epsilon = \kappa \frac{\Delta\sigma}{\mu} \left(\frac{r_0}{r} \right)^3$$

where κ is a constant close to one
 $\Delta\sigma$ is the stress drop, typically, 10 bars (10^6 N/m^2)
 μ is the rigidity usually taken as $3 \times 10^{10} \text{ N/m}^2$
 r_0 is the earthquake rupture dimension
 r is the hypocentral distance

As the stress drop is independent of seismic moment, bigger earthquakes do not necessarily involve bigger strain changes; only the area affected is bigger. As an example, for a moderate earthquake in California such as the Borrego Mountain, recent Imperial Valley, or San Fernando earthquakes, the pertinent dimension is about 10 km to 15 km, the depth of faulting. Farther away than this, the strains will be smaller than 10^{-6} . Figure 2.2 shows the expected average strains as a function of distance and seismic moment (and magnitude).

We might expect that coseismic strain changes and post seismic strain changes would be on the same order of magnitude as a result of redistribution of stress in the lower lithosphere. Post seismic surface slip about the same size as the coseismic slip has been reported (Crook *et al.*, 1980) for the 1979 Imperial Valley earthquake, and strain observations strongly suggest an exponential strain change with a time constant of about 14 hrs and an amplitude of ~ 3 times the coseismic strain change for that event (Wyatt, 1982b). Preseismic strain changes, if they occur, will not likely be much larger. Thus, we conclude that unless instruments are located within the near field of an earthquake, strains of more than a few times 10^{-7} should not be expected. Our observational and instrumental strategies should be based on this premise.

The results of this premise are:

1. Extraterrestrial geodetic techniques with an accuracy goal of 1 cm will likely produce useful measurements of the strain field related to the faulting process only over baselines of 100 km and greater. This applies to existing Very Long Baseline Interferometry (VLBI) and Satellite Laser Ranging (SLR) techniques as well as the proposed Global Positioning Systems (GPS)
2. Terrestrial EDM (Electronic Distance Measurement) techniques currently limited to statistical errors of a few parts in 10^{-7} (in the case of trilateration nets or two color ranging devices) must be improved in order to resolve strains at least an order of magnitude smaller. Further, it is possible that the spatial averaging and infrequent

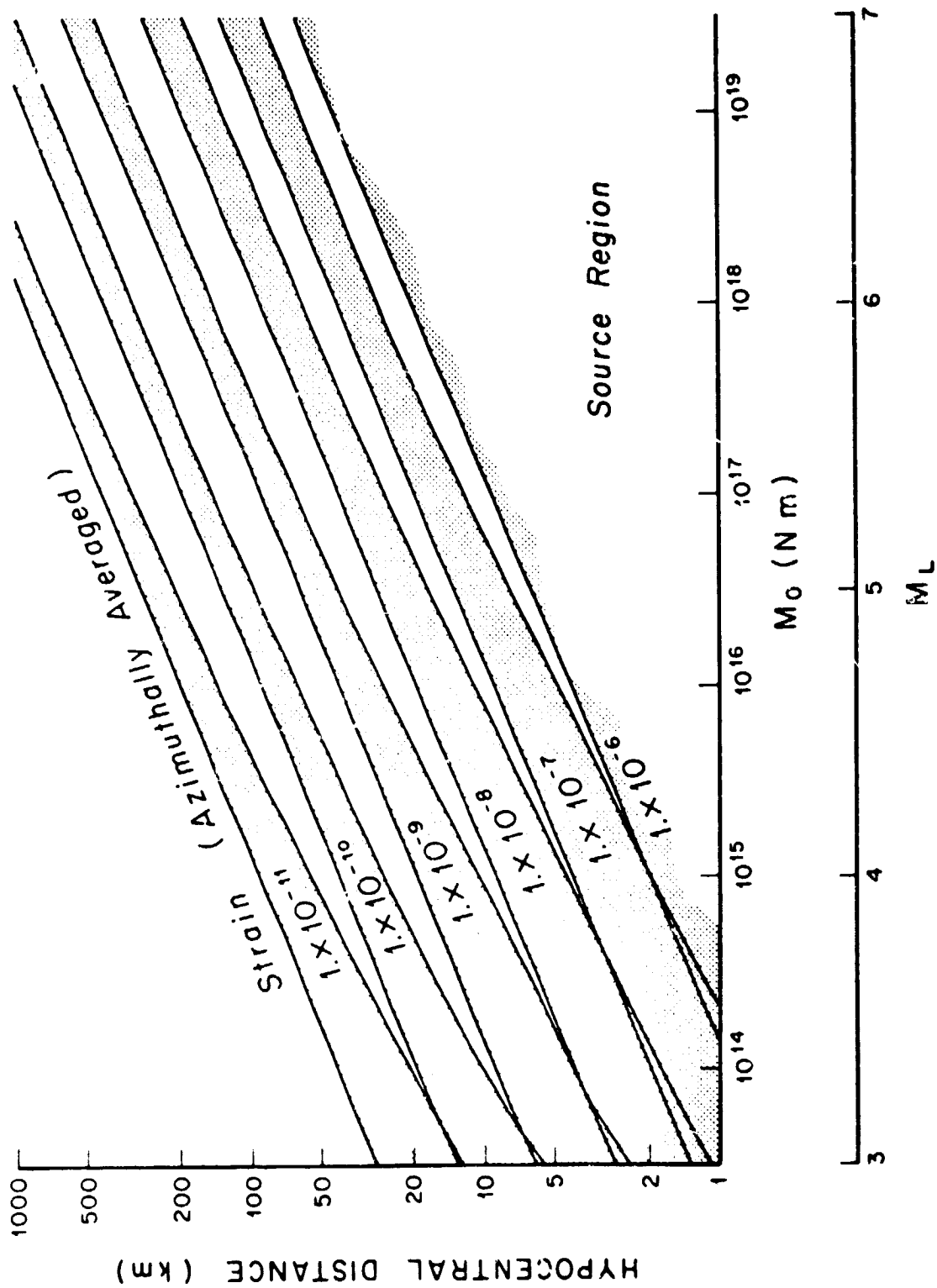


Figure 2.2 Azimuthally averaged (root mean square) strains from a buried strike slip dislocation for a given moment and distance. The width of the shaded area indicates the range of the various components of strain and tilt. The magnitude scale was determined using the moment-magnitude relation of Thatcher and Hanks (1973).

sampling of the trilateration nets may obscure many tectonic signals. If this is so, then densification and more frequent re-surveys of the networks are needed.

3. Observatory based instrumentation must be improved to provide lower noise levels -primarily to distinguish environmental signals from tectonic signals.

2.1 Seismotectonic Setting

Pinyon Flat lies at the junction of the San Jacinto Mountains and the Santa Rosa Mountains, in the northern section of the peninsular ranges of southern California. Located some 20 km south of Palm Springs, California (Figure 2.3), it is between the San Andreas and the San Jacinto fault zones in an area of considerable tectonic interest.

The behavior of the aseismic stretch of the San Andreas Fault south of Parkfield is of considerable importance in view of its past seismic history (the 1857 mag > 8 Fort Tejon earthquake) and the high density of population in the area of southern California. It has long been recognized that somehow strains must be accumulating in this general area to accommodate the inter-plate motions that are so clearly evident both to the northwest and southeast. The trend of the San Andreas Fault swings from NW-SE to nearly EW as it cuts through the southern end of the Transverse Mountain Range. This change of direction may present an impediment to the gradual release of strain accumulation by creep and small seismic events.

The San Jacinto fault, however, offers a contemporary alternate fault which can accommodate at least some of the strain accumulation. Indeed, in many respects, this fault seems a more likely candidate for the principal plate boundary than the San Andreas. As Sharp (1967) has pointed out, the San Jacinto fault is the only fault that cuts the Transverse Ranges and yet maintains the northwest-southwest trend that the plate boundary has on the large scale. Further, it is clearly the most seismically active fault in southern California, having been ruptured by eight moderate ($6 < \text{mag} < 7$) earthquakes since 1897. (Allen *et al.*, 1965; Thatcher *et al.*, 1975). In contrast, the San Andreas fault has experienced only one mag ≥ 6 event south of the great 1857 earthquake in historic times: the 1948 Desert Hot Springs event.

The problem, however, with assigning the San Jacinto Fault as the major plate boundary is the magnitude of the cumulative horizontal motion which has taken place across it. Sharp (1967 and 1981) has estimated the total slip in this fault at 24 km of right lateral motion. Pleistocene slip rates are estimated at 0.8 to 1.2 cm/yr, considerably less than the 6 cm/yr deduced as the average North American-Pacific Plate motion in this area (Minster and Jordan, 1978). However, Sharp (1980) also points out that in the last few hundred years, there is evidence that the slip rate on the San Jacinto Fault may have been as great as 5 cm/yr. He concludes that, "If the San Jacinto and adjacent segments of the San Andreas fault alternately assume dominant roles in absorbing motion between the Pacific and American plates, perhaps even more recently than 400 years ago, the San Andreas fault in the northern Salton Trough expressed most of the motion but has since become relatively inactive."

In their study of the historic seismicity along the San Jacinto Fault, Thatcher *et al.* (1975) demonstrated that sequence of events along the fault since 1890 has ruptured the fault along nearly its entire length. Two gaps apparently remain, one at the northern end of the fault and the other in the region of the town of Anza (Figure 2.3). There was a moderate earthquake near Anza in 1937, but its moment of 2×10^{22} dyne-cm. indicates that it could hardly be considered a major rupture of the area. The U.S. Geological Survey periodically re-surveys some seven trilateration networks in southern California utilizing laser distance measuring devices. The networks are irregular figures with typical dimensions of 100 km and it usually takes many weeks to complete one resurvey. For each network, the individual line length changes are least squares fit to a model of homogeneous strain where it is assumed that the strain field is uniform over the network and over the interval (i.e., in space and time) (Prescott *et al.*, 1979).

Savage *et al.*, 1981, reported their most recent results which span the years 1973-1980. Figure 2.4 shows their results for the principal strain rates averaged over this period. The average strain rates for all of southern California during this period were 1.8×10^{-7} /yr. north-south

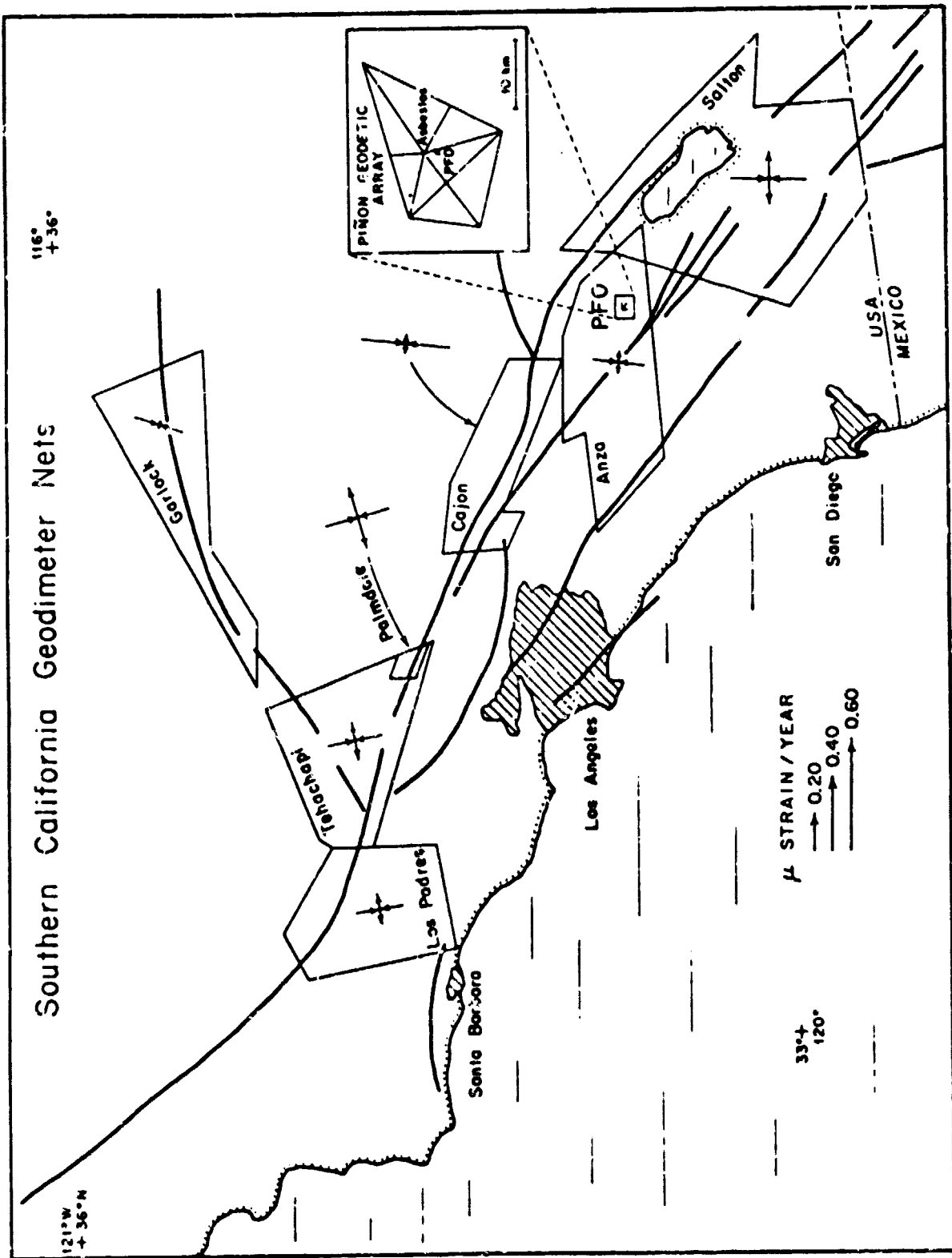


Figure 2.4 Southern California geodimeter nets

contraction coupled with a 0.8×10^{-7} /yr. east-west extension. However, Savage *et al.*, 1981, point out that certain regional variations in this picture are suggested by the data. Prior to the 1978-79 interval, the strain rates averaged to 2.6×10^{-6} north-south contraction with an undetectable east-west extension. The change in the strain rates appeared first on the southern networks and then migrated northwards. It is interesting to note that the seismicity of the area for several years prior to the 1978-1979 period was anomalously low (Bufe and Toppozada, 1980) and since then has been significantly higher.

With the tectonic and seismic setting in mind, we chose the exact site of the observatory (PFO) from more mundane considerations. We sought a suitable site for the installation of long baseline (1 km) instrumentation which translated into a requirement for a fairly flat piece of land of approximately 160 acres. Further, it was important to locate the observatory on competent material away from large accumulations of alluvium. Finally, we sought a relatively remote area to reduce cultural interference, and to make the acquisition of suitably sized parcel of land a practical matter.

Pinyon Flat, which is located some 12 km northeast of the San Jacinto fault system and 25 km southwest of the San Andreas fault zone (33.609°N , 116.455°W), is an area that has the desired properties. The flat is situated on the northern-most flank of the Santa Rosa Mountains in the Peninsular Range Province. Roughly 12 km^2 in area, the flat is bounded by Asbestos Mountain to the north, Deep Canyon to the east, Santa Rosa Mountain to the south, and Palm Canyon to the west. Figure 2.5 (after Wyatt, 1982a) shows a generalized map of the pertinent geological features and a sectional profile of the area, indicating the smooth topography of the flat between "PFO" and "Edge."

As Wyatt (1982a) points out, there are several possible explanations as to why such an isolated flat surface is found at these elevations (1300 m). Undoubtedly part of the reason is the nature of the crystalline rocks which underlie the area. The rocks are composed of Pinyon Flat Granodiorite (Foster, 1976) of middle Cretaceous age (90-100 Ma b.p.). This rock is unusually rich in biotite which causes rapid weathering because of its expansion when exposed to moisture (Isherwood, 1976). Weathering causes the near surface rock to decompose (via granular disintegration) to grus.

Jahns (1954) suggested three possible mechanisms for the development of low relief surfaces on pre-Cenozoic terrain of crystalline rocks in the Peninsular Range Province: 1) The areas may be remnants of a single extensive peneplain, called the Southern California peneplain, that have been differentially uplifted by Quaternary faulting. 2) Some of the surfaces may be exhumed features that were originally formed in pre-Quaternary time and only recently re-exposed. Some support for this mechanism is available near Pinyon Flat (see lower portion of map in Figure 2.5) where Quaternary terrace deposits are isolated on older rocks. 3) Finally, the surfaces may have formed locally by erosion to a new base-level. Such a surface of low relief on exposed bedrock, when formed in a semi-arid region and situated between an alluvial valley and a mountain, is commonly called a pediment (see, for example, Cooke and Warren, 1973). The concave form of the topography (towards the SW), the thin veneer of weathered material, and the size of the area are all features in common with pediments. Absent from the Pinyon Flat area is a base-level defined by an alluvial plain.

This unusual situation may be explained by considering a mechanism presented by Wahrhaftig (1965). Wahrhaftig observed that exposed granites weather much more slowly than those rocks which are buried, and hence are moist for longer periods of time. Perhaps the relatively unweathered outcrops exposed on the southwest edge of the flat tend to act as a local base-level. Another possibility is that the change in lithology near the edge of the flat is responsible for reducing the erosion in that area.

Whatever the cause or combination of causes responsible for the creation of the surface, the most significant process currently affecting the surface layers is weathering. The near surface (at a depth of .5 m) is subject to a yearly temperature range of 18°C , with daily variations on the order of $.3^{\circ}\text{C}$. On rare occasions ground frost will reach a few cm in depth. The average annual rainfall has been 25.4 cm, for the period 1971 through 1980. Normally this

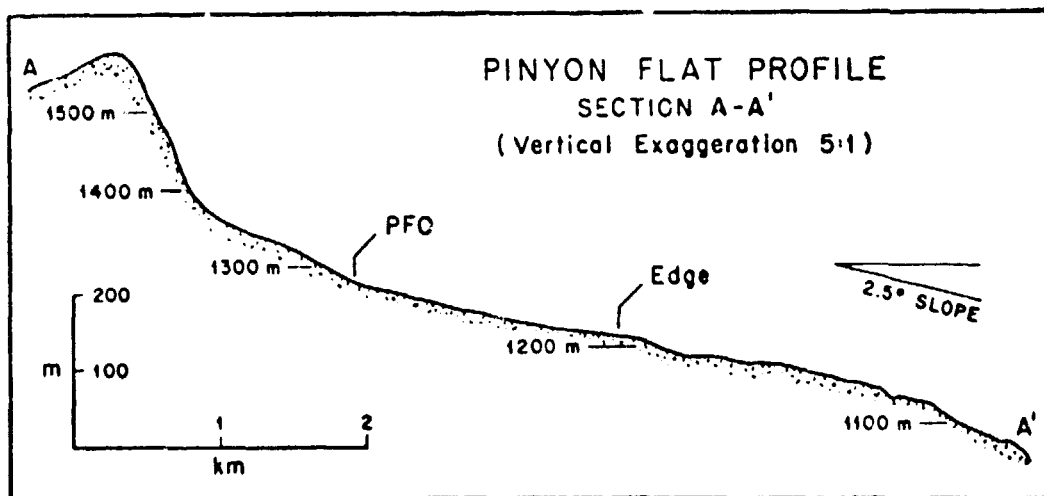
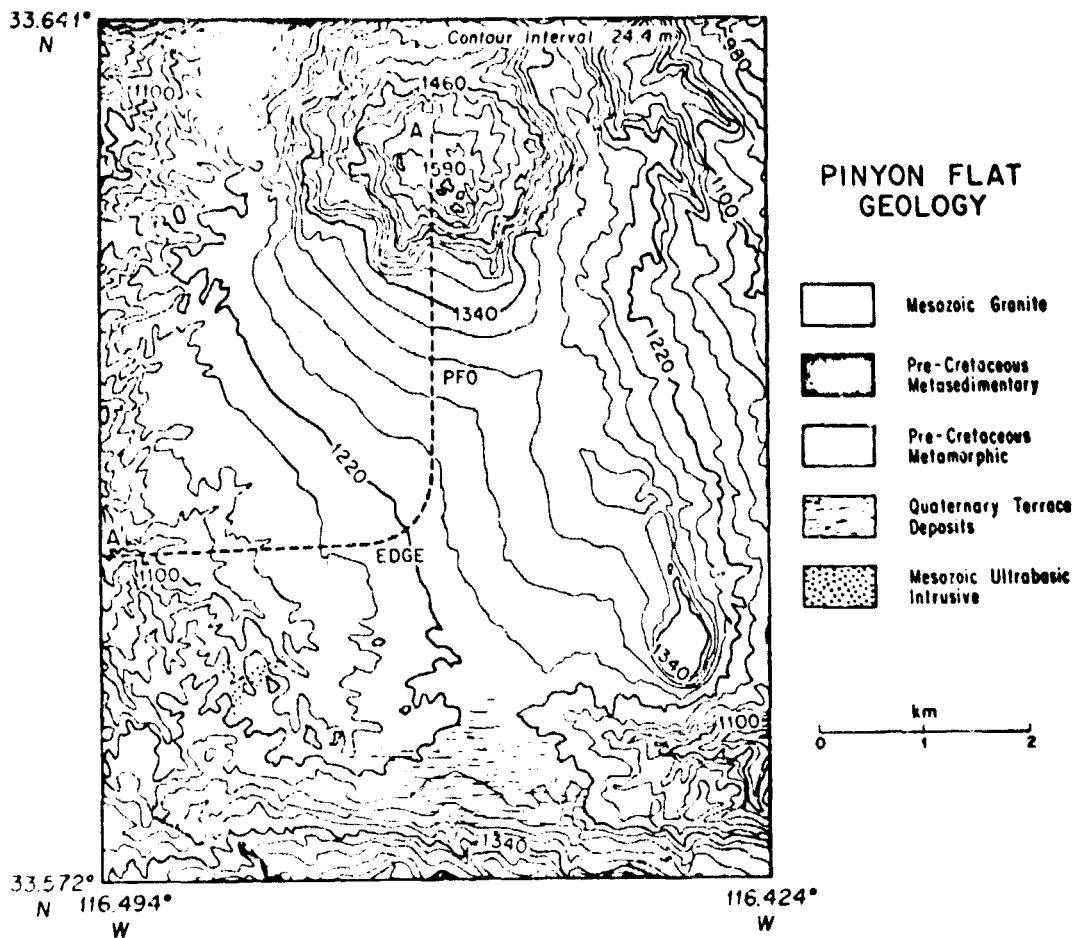


Figure 2.5 Generalized map of the geologic features at Pinyon Flat, California and a sectional profile from Asbestos mountain (A) to Palm Canyon (A') (after Wyatt, 1982)

precipitation occurs in the form of infrequent (but intense) thundershowers in the months of August and September, along with less substantial prolonged winter storms. The top 1 m of ground at the site is nearly fully decomposed granodiorite. Below this level the weathered rock grades to highly competent grus at a depth of roughly 3 m. This material has decomposed in situ; dikes and other features of the rock are readily identifiable. At this depth standard soil moving machinery is no longer effective in excavating material. However, once a section of rock is removed it is found to be friable. The majority of the reference monuments at PFO were emplaced in the material at this depth. Conventional benchmark rods reach the depth of refusal in this layer (1-3 m). Evidence provided by drilling suggests that below 3 m to a depth of 25 m the material grades from grus to grus with corestones, and finally to jointed granodiorite as illustrated in the right half of Figure 2.6.

Wyatt (1982a) conducted a shallow seismic refraction survey at PFO which supports these observations. Figure 2.6 presents the possible range of the compressional seismic velocities for two locations at Pinyon Flat. These velocity corridors were determined using a procedure described by Garmany *et al.* (1979). The heavy solid lines are the extremal bounds on the solution to the seismic travel time inverse problem at PFO, based on the limited and inexact nature of the field observations. The dashed lines are the bounds at Edge. All possible models of the velocity profile lie within these bounds. The light solid lines indicate particular models that may be used to generate the observed travel times. It is unlikely that the layering shown in these models exists; rather the velocities probably increase smoothly with depth, as the effects of weathering diminish.

There is a marked difference between the seismic velocities at PFO and Edge. Velocities less than 2 km/sec, normally associated with sediments, are limited to depths of 8 m at Edge, but may extend as deep as 18 m at PFO. The PFO profile is representative of the majority of the area, while the Edge data are more characteristic of the material at the limits of the flat, where outcrops (tors) are prevalent. Evidently the weathering is less near the edge of the flat, supporting Wahrhaftig's hypothesis for the formation of such surfaces.

Below 20 m the velocities at both locations tend to values that are characteristic of granodiorite subjected to low confining pressures (~ 0.5 MPa) (Birch, 1966). Analysis of a core sample from PFO established the seismic velocity at a depth of 38 m to be 4.8 km/sec (C. Sondergeld, personal communication, 1980). This value is in excellent agreement with the mean velocity obtained by extrapolating the linear trend of the extremal bounds in Figure 2.6, and is representative of crustal rock velocities. We may assume that instruments not adequately coupled to the rock below the material with low velocities (~ 20 m at PFO) will be sensitive to the displacements inherent in the weathering process.

2.2 Instrumentation

While PFO today contains some 20 independent sensors, and experiments run by a number of different organizations (UCLA, UCSB, L-DGO, NASA/JPL, AFGL, Leighton and Associates, CIRES, National Geodetic Survey, Cambridge, and Carnegie Institution) (see Figure 2.7), we will confine our comments in this report to the results from the long laser strainmeters (LSM). These instruments were the first to be installed at the observatory and have undergone continual refinements in an effort to increase their accuracy and lower their noise levels.

Berger and Lovberg (1970) described the basic LSM design which was built and operated near the UCSD campus in San Diego, California. The optical configuration of the strainmeters is that of a Michelson Interferometer with a 732 m arm (see Figure 2.8). The changes in length of this arm are thus measured in terms of the wavelength of the laser light. We use a Spectra Physics Model 119 for the light source as it provides a unimodal single frequency output. The laser radiation is, of course, highly monochromatic, but the center frequency is determined by the mechanical properties of the laser resonator. Hence, the long term wavelength stability is dependent upon this resonator's mechanical ability which is probably good only to about a part in 10^6 over long periods. To achieve a stability sufficient to measure earth strains,

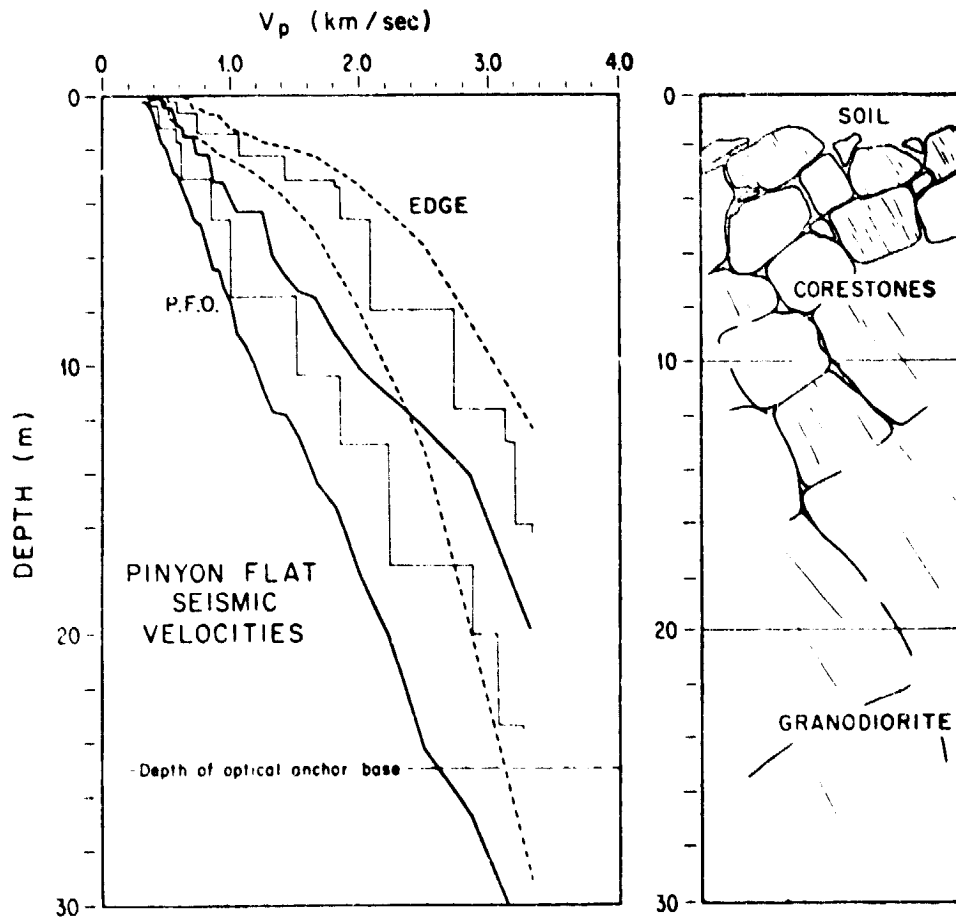


Figure 26 Range of near surface compressional velocities for two locations at Pinyon Flat. Dashed lines indicate the range at Edge (see Figure 1) and the solid lines indicate the range at P.F.O. Also shown is an illustration of the structure as suggested by borehole drilling observations (after Wyatt, 1982).

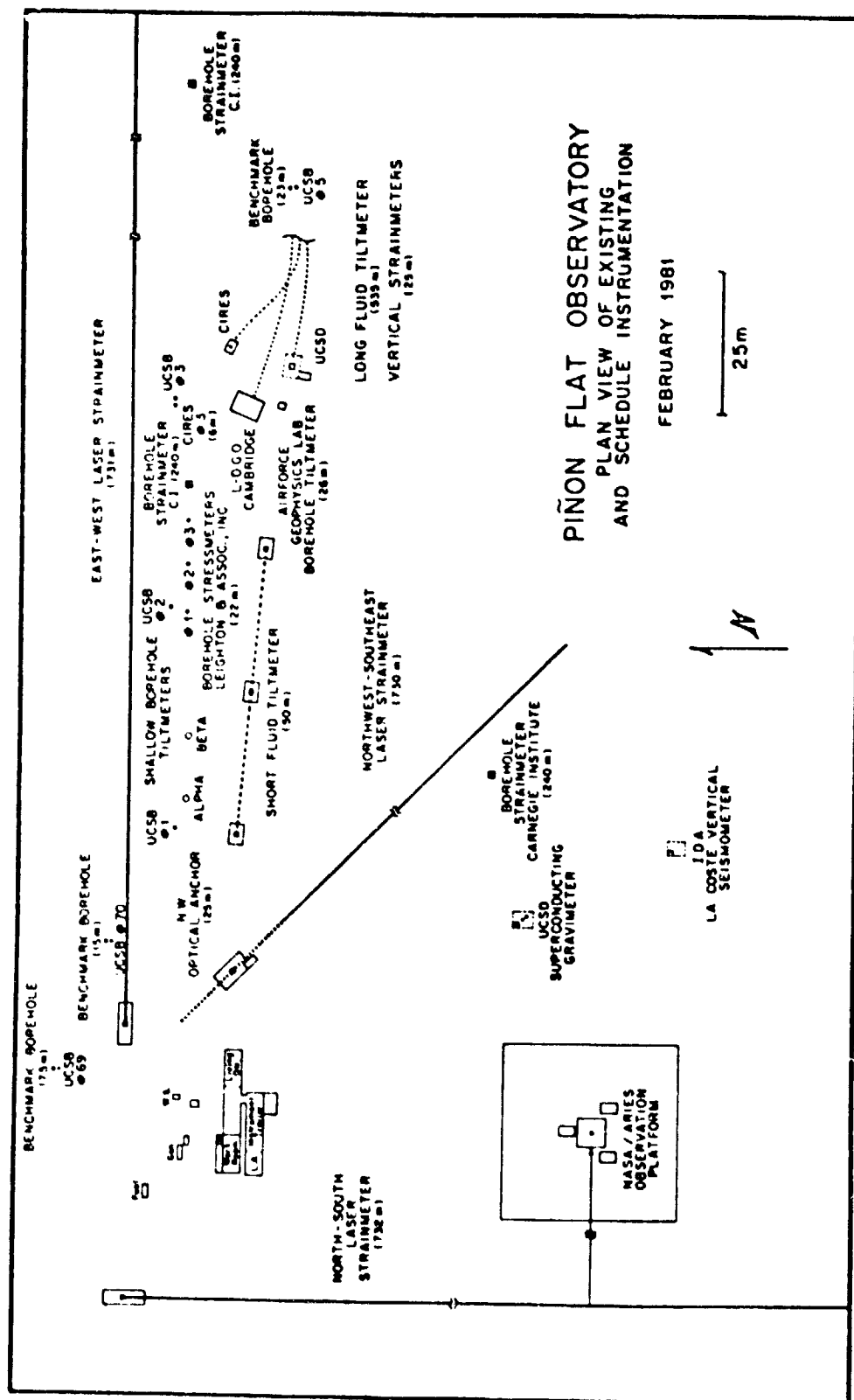


Figure 2.7 Plan view of existing instrumentation at PFO

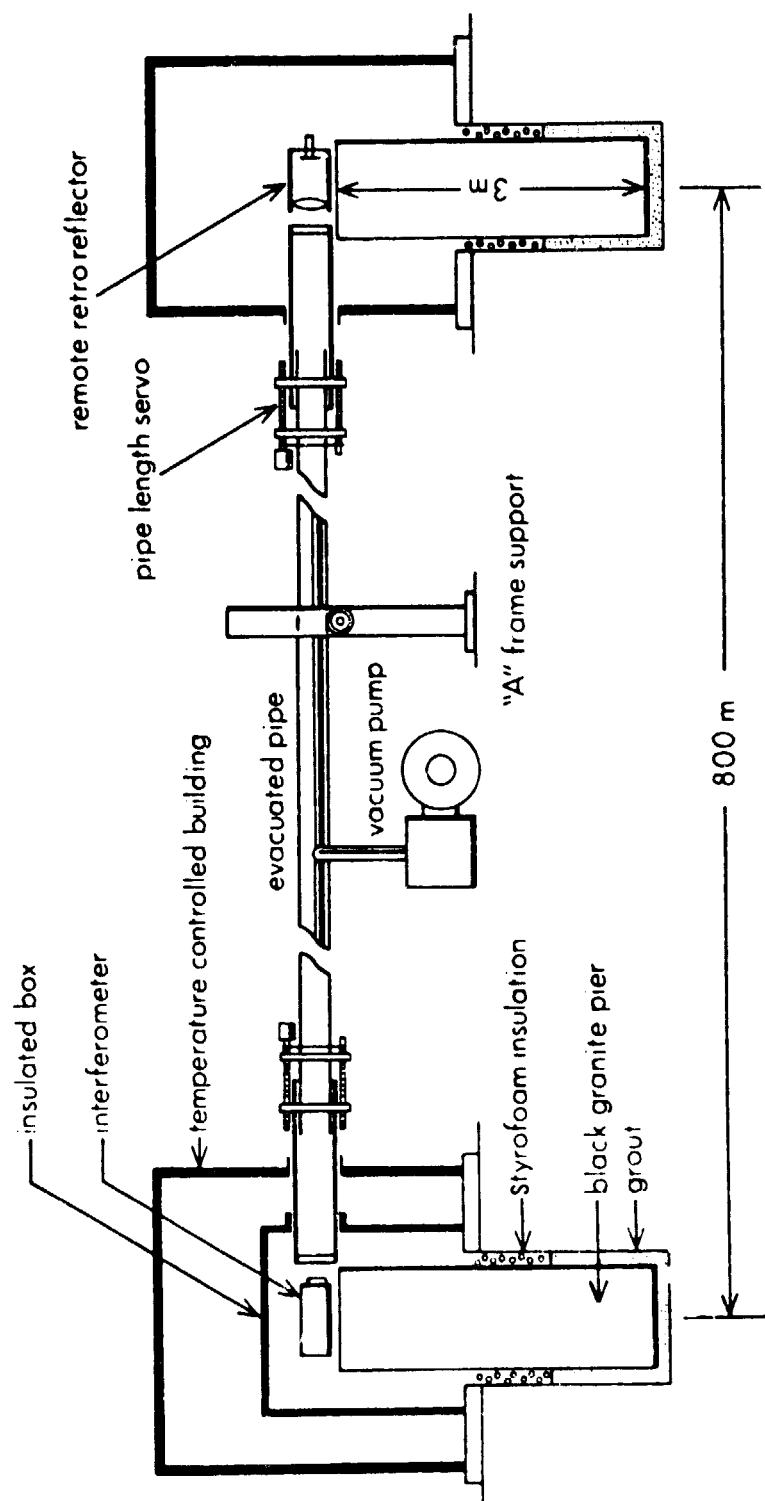


Figure 2.8 N-S and E-W strainmeters

the wavelength of the laser radiation was locked to the length of a fused silica Fabry-Perot resonator, contained in a controlled environment. The length standard, then, for these experiments, is a 30 cm tube of fused quartz. Each of the three strainmeters is independently stabilized, but periodically the Fabry-Perot stabilizers are exchanged between the three strainmeters and the records examined for concurrent changes in the secular strain rates. The lack of any such changes gives us a high degree of confidence that, at least to the levels of strain rate we report herein, the length standards do not contribute to the secular strain observed.

Following this basic design, with a few minor changes, three of these devices were installed at PFO, one each year in 1971, 1972 and 1973. The instrumental statistics for these are given in Table 2.1.

Both the NS and NW instruments are installed along concave topography and so it was necessary to re-steer the beam part way along its length in order to keep it close to the ground. There are two prisms mounted in a housing at the center point (the low point) of the vacuum tube. Each may be independently rotated so that the beam may be re-steered from this point. During construction the beam is steered to the center point, through the air, half the vacuum tube constructed and then, with a window at the steering prism and half the length evacuated, the beam is steered to the retro-reflector pier again through the air.

The first two strainmeters, the N-S and E-W, utilized the end pier design as shown in Figure 2.8. Holes about 1 m in diameter were drilled into the surface to a depth where the drill rig (a caisson rig) could no longer penetrate. Rectangular columns of black granite, quarried to size, were then set into these holes with a non-expansive grout cementing the bottom meter or so to the hole walls. The remainder of the space between the column and the hole sides was filled with styrofoam balls. The column with its optics on top was covered with an insulated box and the whole apparatus enclosed in a temperature controlled building.

The NW-SE strainmeter has a somewhat different end design. In an attempt to alleviate the effect of tilt of the end columns, it was decided to use roughly cubical end piers and bury the entire end structures in a vault. Figure 2.9 illustrates the NW strainmeter layout.

During 1973, quartz tiltmeters (Wyatt, 1982a) were installed on each of the six strainmeter piers for reasons given later.

The tilt transducers consist of three pieces of fused quartz that form a three-element differential capacitive transducer. Two of the elements are clamped together and plated with platinum electrodes to form the fixed plates of the capacitor. The third piece is plated on both sides and is suspended by two fine wires between the two fixed plates with a separation of .25 mm on each side. The effective pendulum length is 6.75 cm with associated free period of 1/2 sec and it is heavily overdamped.

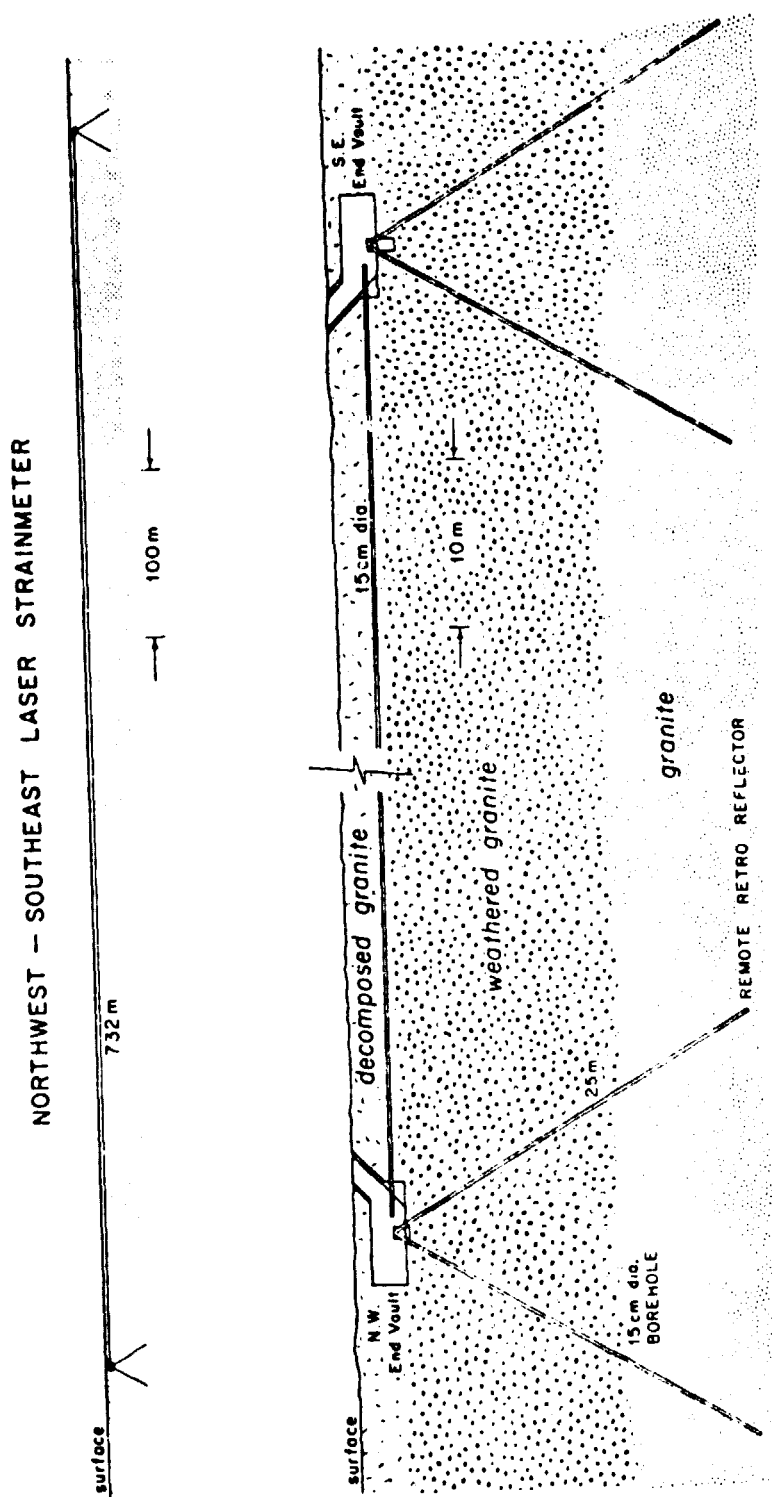
This whole assembly is clamped to a ground section on the side of the strainmeter granite piers. The unit is hermetically sealed and temperature controlled.

One of these instruments is mounted on each of the six strainmeter end piers. The instruments are readily calibrated by pushing on the piers and noting both the tiltmeter output and the strainmeter output, thus giving a tilt produced strain coefficient for each column. Typical motion induced at the top of the pier, with a strenuous push is 6×10^{-6} m with a corresponding tilt for a 3m column of 2×10^{-6} rad.

After corrections to the strain records were made for the local tilt of the piers as measured by the pier tiltmeters, significant changes in the strain were still observed, correlated with heavy precipitation, as we shall discuss in Section 2.3. These perturbations were especially obvious in the corrected records of the NW-SE strainmeter. The inability of the pier tiltmeters to correct for the local motions of the cubical piers of this strainmeter led us to the design of a device to measure the displacement of the piers relative to points some 24 m below the ground surface. An "optical anchor" (Wyatt *et al.*, 1982) was installed at the northwest end of the NW-SE strainmeter early in 1980.

Table 2.1
Strainmeter Parameters NS, EW and NW

Component	NS	EW	NW
Azimuth	180.28°	90.44°	135.26°
Dip	3.0°	-0.73°	0.7°
Length (m)	732.2	730.8	730.4
Height of end piers (m)	3.8 (N) 2.9 (S)	4.7 (W) 4.7 (E)	1.2 (NW) 1.7 (SE)
Depth of end piers (m)	1.2–2.7 (N) .8–1.8 (S)	1.0–3.2 (W) 1.0–2.7 (E)	3.4 (NW) 3.3 (SE)
Gain (strain/l.c.)	1.7610×10^{-10}	1.7713×10^{-10}	1.7666×10^{-10}
Filter time constant (s)	507	506	521



Schematic of Optical Anchoring System

Figure 2.9 NW - SE strainmeter.

2.2.1 Optical Anchor†

Figure 2.10 is a schematic diagram of the optical anchor. A laser interferometer is used to monitor the difference in length between the two paths P_0P_1 and P_0P_2 . The horizontal shear strain can be computed from the change in this distance, provided that the points P_1 and P_2 are either well coupled ($\vec{d}_1 \approx \vec{d}_2$) or are undergoing much smaller displacements than P_0 . Geologic evidence suggests that the near-surface at PFO is much less stable than the material at depth (Wyatt, 1982a), so that both of these assumptions are likely to be true.

Formally, we may describe the measurement in terms of a coordinate system in the bedrock below the instrumentation (Figure 2.10). The x axis is aligned in the direction of the shear measurement, the x_2 axis is in the vertical plane of P_0 , P_1 , and P_2 , and the x_3 axis is perpendicular to both. For this instrument, where the optical path lengths are much larger than the displacements to be monitored, the quantity recorded is:

$$D = (\vec{d}_0 - \vec{d}_1) \cdot \hat{P}_1 - (\vec{d}_0 - \vec{d}_2) \cdot \hat{P}_2, \quad (1)$$

where \vec{d}_0 , \vec{d}_1 , and \vec{d}_2 are the displacement vectors for the points P_0 , P_1 , and P_2 respectively, and \hat{P}_1 and \hat{P}_2 are the unit vectors along the two optical paths. To simplify this expression we assume that $(\vec{d}_0 - \vec{d}_1) = (\vec{d}_0 - \vec{d}_2) = d$. This is justified when the end points P_1 and P_2 are located in material more stable than P_0 ($|\vec{d}_1|, |\vec{d}_2| \ll |\vec{d}_0|$). Given that $\theta_2 = \pi - \theta_1$ equation (1) reduces to

$$D = 2 \cos \theta_1 \times d \cdot \hat{x}_1 \quad (2)$$

Finally, for $\theta_1 = 60^\circ$, equation (2) becomes

$$D = d \cdot \hat{x}_1 \quad (3)$$

which is simply the horizontal displacement of point P_0 relative to "fixed" points P_1 and P_2 .

Figure 2.11 illustrates the arrangement of the optical anchor in the northwest vault of the Northwest-Southeast (NW-SE) strainmeter at PFO. Two boreholes, inclined at 30° from vertical, were drilled some 26 m from a point 2.5 m below the surface. The holes were drilled in the vertical plane aligned with the azimuth of the strainmeter axis, and intersected at a point roughly 1 m above the vault floor. A cement monument approximately 1 m^3 in volume was formed at the top of the boreholes and a granite optics table placed on this pad. Reflectors mounted near the bottom of the boreholes served as the fixed reference points for the instrument.

Proper orientation and alignment of the two boreholes were essential to the operation of the instrument. The driller (Rex Anderson Corp., Julian, California) was successful in the initial attempt at this operation. A top-head drive drilling rig was positioned above the strainmeter vault, locked at an angle of 30° from vertical, and the holes were bored with an 16.5 cm air rotary percussion drill. To maintain a straight hole the hammer bit was followed by a 6.4 m stabilized drill rod. (The stabilizer was made by welding three steel bars in a spiral along a standard drill section so that the overall diameter was 16.5 cm.) The profiles of both holes had nearly uniform curvature, with a deviation of less than 5 cm from the straight line connecting the end points. The final clear aperture, necessary for the laser to illuminate the center of both remote reflectors, was 3.5 cm, barely larger than the beam diameter (2 cm). Table 2.2 presents other physical and instrumental parameters.

The most difficult part of the instrument design was devising a method to attach the remote reflectors to the sides of the boreholes in a stable manner. Although positioning an optical component with a stability of $40 \text{ } \mu\text{m}/\text{year}$ (corresponding to a strain rate of 50 nstrain/year on the 731 m instruments at PFO) is easily accomplished in the laboratory, the

† This section is taken from Wyatt *et al.* (1982)

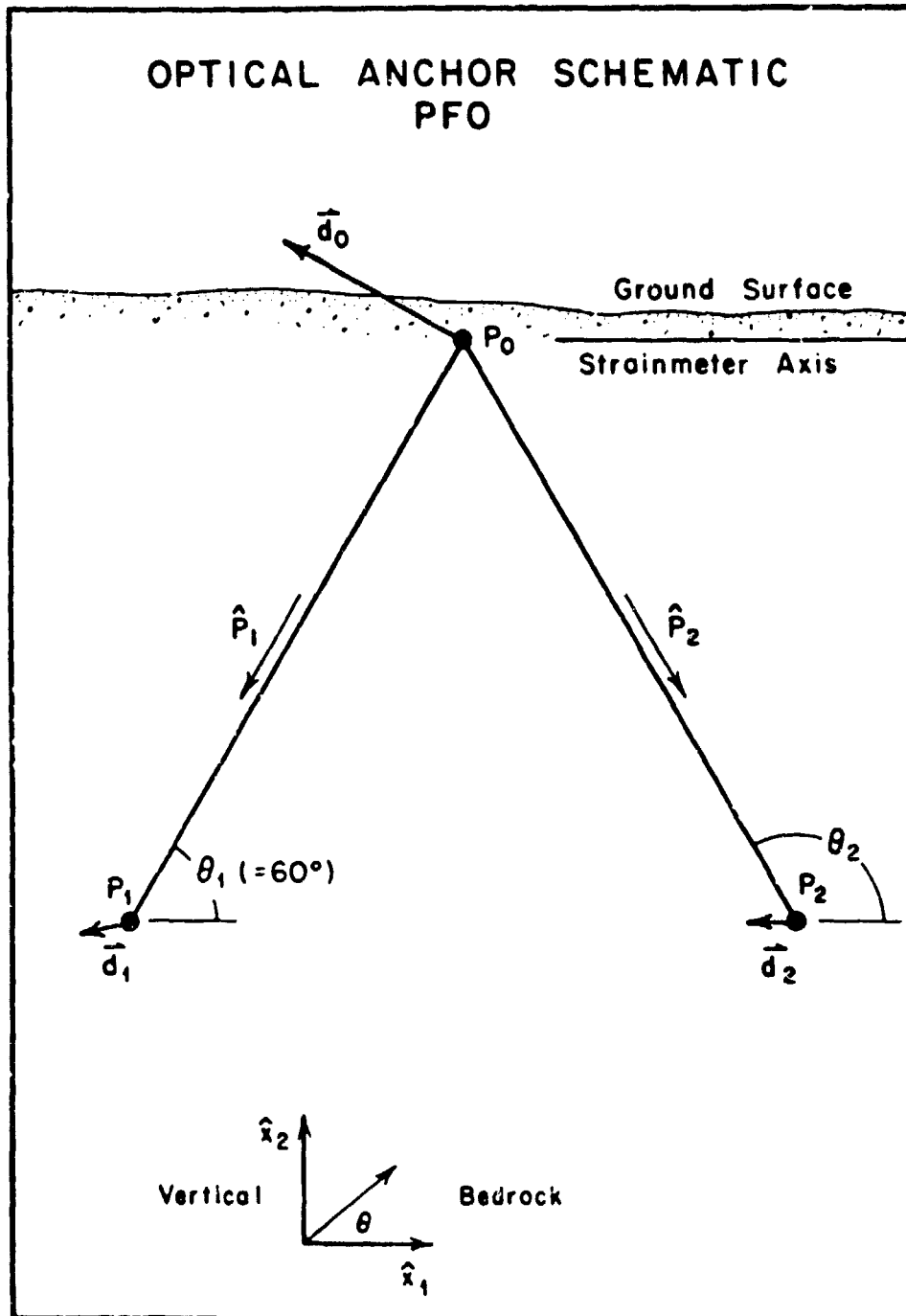


Figure 2.10. Schematic of the optical anchor. Points P_1 and P_2 are located at a depth of 24m. \hat{P}_1 and \hat{P}_2 are unit vectors along the two optical paths (after Wyatt *et al.*, 1982).

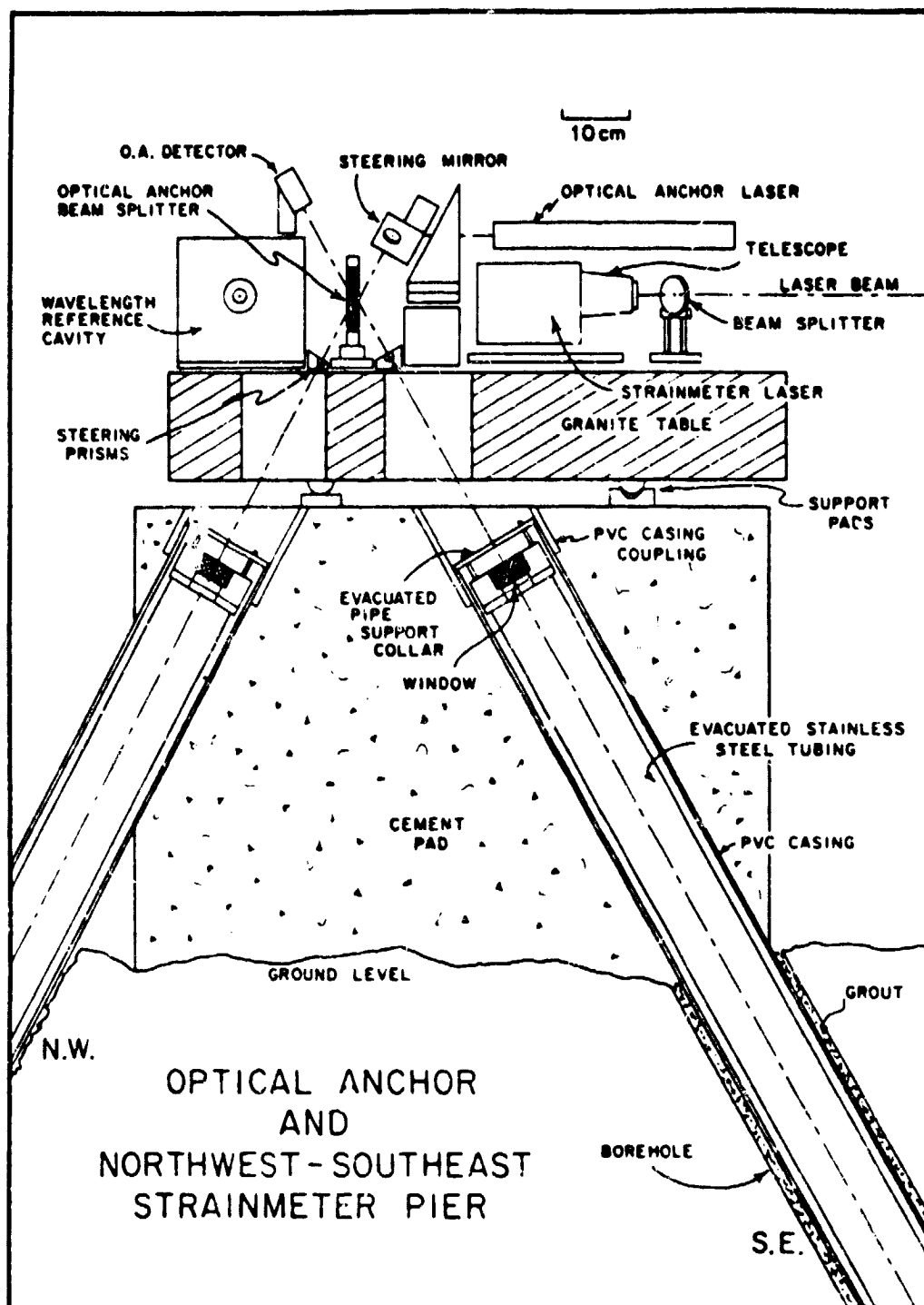


Figure 2.11 Details of the optical anchor interferometer and the reference moment at the north-west end of the Northwest-Southwest strainmeter, Piñon Flat Observatory (after Wyatt *et al.*, 1982)

Table 2.2
Optical Anchor Physical and Instrumental Parameters

Physical Parameters	
Length of optical paths	25 m
Path length difference	.5 cm
Depth of interferometer	2.44 m
Depth of retroreflectors	24.09 m
Borehole angle relative to vertical	$30^\circ \pm 2^\circ$
Borehole azimuthal alignment error	$\pm 3^\circ$
Laser beam intersection aperture	3.5 cm
Borehole inside diameter	16.5 cm
Casing outside diameter	14.4 cm
PVC casing wall thickness	7.1 mm
Evacuated tube outside diameter	10.2 cm
Evacuated tube wall thickness	1.6 mm
Bellows outside diameter	5.7 cm
Bellows spring constant	10^4 N/m
Bellows position imbalance	3 mm
Pressure on casing during cementing	400 kPa

Instrumental Parameters	
Pressure in evacuated tube	20 Pa
Pressure variations in tubing	5 Pa
Laser output power	1 mW
Expanded laser beam diameter	16 mm
Beam divergence over 50m	2.4 mm
Temperature coefficient	10^{-6} m/ $^\circ$ C
Maximum temperature fluctuation	2 $^\circ$ C
Precision of Optical Anchor	7.9×10^{-8} m
Calibration accuracy	.2 %

task is quite difficult in the field. On the time scale of years, creep of the anchoring assembly in response to stress must be considered.

Figure 2.12 presents the detailed cross-section of the anchoring arrangement at the bottom of the inclined holes. Each of the boreholes was cased with PVC pipe, with a 1.2 m stainless steel anchoring assembly threaded onto the end of the casing. The assemblies were machined with many circumferential grooves and were cemented into place using non-shrink grout. Rubber pads were attached to the bottom of the anchors to reduce axial loading caused by borehole rebound and deformation of the cement. The grout was pumped through check valves in the bottom of the stainless steel assemblies and up the outside of the PVC casings until it reached the surface. During this operation the casings were filled with water to prevent the PVC pipe from collapsing. After the grout hardened, the water was evacuated from the casings by injecting compressed air.

Near the upper end of the 1.2 m anchoring assembly, a tapered and threaded insert was machined to guide and secure the retro reflector housing. This housing was attached, by a pair of stainless steel bellows, to the end of a long stainless steel vacuum pipe. The bellows were required both to isolate mechanically the reflector housing from the vacuum pipe and to allow compensating pressure on both sides of the reflector. The vacuum pipe was supported only at the surface, assuring that the reflector housing was not subjected to excessive longitudinal forces (due to the weight of the tubing). Details of the retro reflector housing and the anchoring assembly are presented in Figure 2.13.

Two detectors were monitored during the installation of the vacuum pipes and reflectors. One transducer, mounted on the reflector housing, indicated when the unit was fully screwed into the anchoring assembly. The second detector was used to adjust the position of the vacuum pipe at the surface so that the forces of the bellows were balanced.

A well pump was designed to keep the inside of the borehole casings free of ground water, though this has proven to be unnecessary. The pump consisted of an 8 mm copper tube that extended from the surface to a point below the reflector housing and a second tube (6 mm) that connected to the first at a position 1 m above the bottom. The pump was operated by evacuating the longer tube, with the small diameter tube closed at the surface, so as to draw water up the larger tube to a height of roughly 10 m. Opening the second tube to the atmosphere forced most of the fluid above the joint to the surface. (Surface tension of the water kept the air from simply bubbling through the liquid.) Repeated "burping" of the system would lower the water level inside the casing.

The differential path length measurement is easily accomplished using standard optical techniques (see for example, Strong, 1958). Because the optical paths are nearly equal, the Michelson interferometer does not need a laser with a very stable frequency. The frequency stability of an inexpensive He-Ne laser ($\Delta f/f \sim 10^{-6}$) gives a maximum error of only 5×10^{-9} m for the actual path length difference of .5 cm. The sense of the interference fringe motion was monitored by deliberately retarding, by 1/8 of a wavelength, opposing quadrants of one of the optical paths, and detecting the resulting phase shifted fringe pattern (Berger and Lovberg, 1970). A reversible electronic counter was employed to record changes in length corresponding to 1/8 of a wavelength of He-Ne laser light (7.91×10^{-8} m).

To reduce possible errors, the pressure in the optical paths was lowered by connecting both pipes to the vacuum pipe of the nearby laser strainmeter. The pressure inside the strainmeter vacuum tubing was maintained at 1 Pa (Berger and Lovberg, 1970). A restriction in the vacuum conduit between the strainmeter and the optical anchor assured stability of the strainmeter vacuum pressure. The resulting pressure in the optical anchor vacuum paths was approximately 10 Pa: more than adequate to eliminate temperature differentials in the two paths as a source of error. However, pressure differentials of only 1 Pa correspond to a displacement of 8×10^{-8} m, roughly the limit of resolution of the instrument. Maintaining the absolute pressure below 20 Pa limited the magnitude of the differential pressures to an acceptable level.

ORIGINAL PAGE IS
OF POOR QUALITY

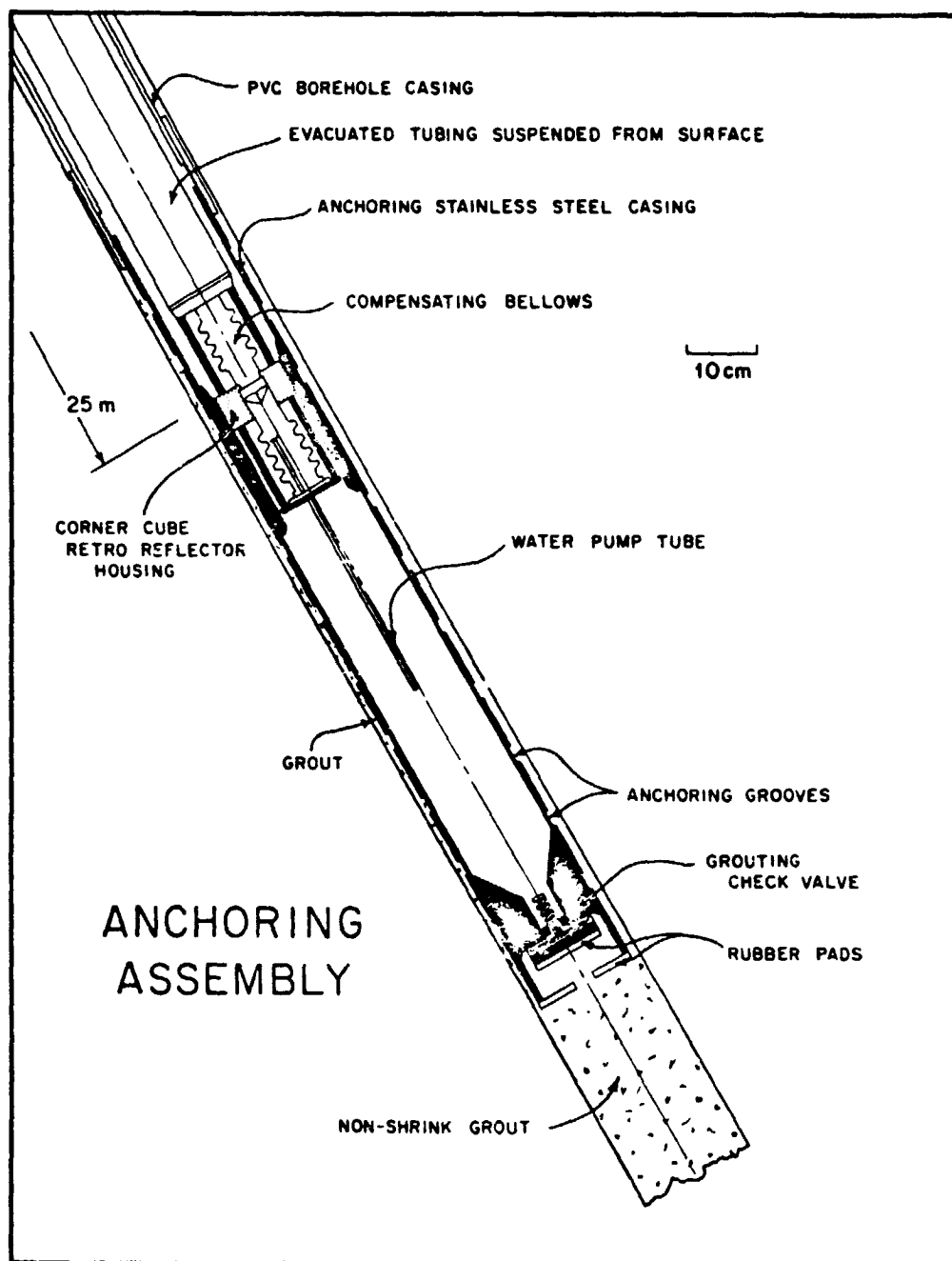


Figure 2.12 Anchoring assembly, shown cemented near the bottom of one of the angled boreholes (after Wyatt *et al.*, 1982).

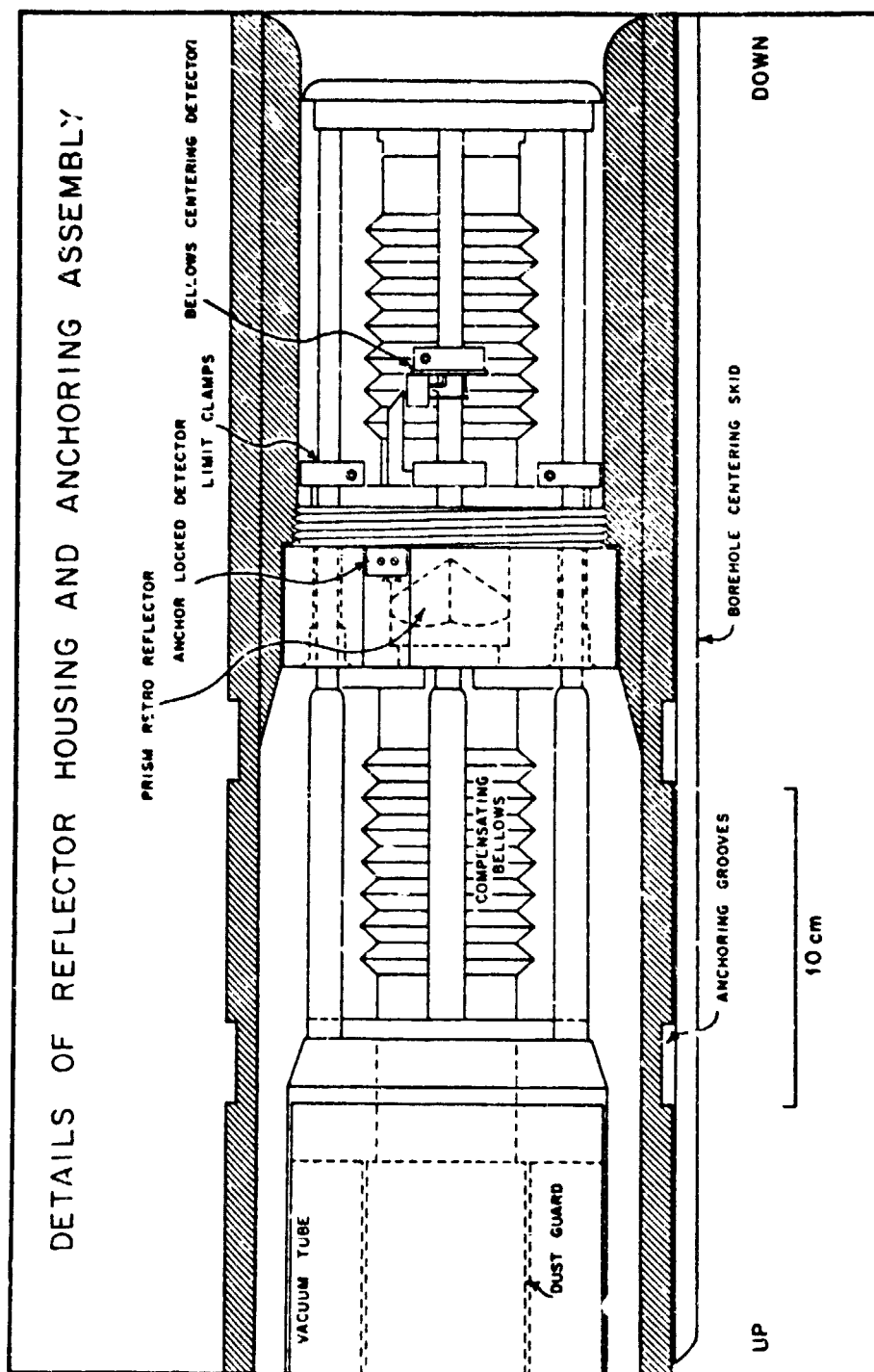


Figure 2.13 Details of the reflector housing and the anchoring assembly (after Wyatt *et al.*).

The completed instrument had a temperature coefficient of (approximately) 10^{-6} m/°C, probably from temperature sensitivity of the optical mounts on the granite optics table. No attempts were made to improve this, because the strainmeter vault was temperature regulated, ameliorating the problem.

The optical anchor was calibrated by comparing the output of the system with the signal from the coaxial NW-SE laser strainmeter. Slight errors in the alignment of the optical paths were the main source of uncertainty in the gain of the instrument. Displacement of the strainmeter end monument provided an immediate calibration, as this displacement was measured (by the NW-SE strainmeter) in terms of the wavelength of He-Ne laser light, known to more than five significant figures. In practice, the accuracy of the calibration was limited by our reluctance to displace the reference monument so much that the bond with the earth might be broken. The final transducer gain was found to be 7.9×10^{-8} m/count.

2.3 Results

In this section, we will report on the results of the laser strainmeters and their ancillary instrumentation. Results from the superconducting gravimeter are reported in Sections 4 and 5 of this report.

One of the first questions addressed in the analysis of the PFO strain observations, and a general question regarding all strain observations, is how do we know that observations on the surface at one place are representative of the regional crustal strain?

Distortions to the regional strain field may arise from inhomogeneities in material properties in the neighborhood of the observing point. Topographic irregularities will also cause an effect, distorting the strain field from that which would be observed on a smooth surface. Berger and Beaumont (1976) investigated the distortions to a homogeneous strain field caused by the local topography at PFO and a crude two-dimensional model of the regional geology. This study concluded that a 10-20 percent variation in the measured linear extensions might be expected, compared to those on the surface of a homogeneous ellipsoidal earth. Clearly, as we move from place to place, even if the applied strain field were homogeneous, we would expect fluctuations on that order.

To test if our point observations of strain come close to matching our theoretical models, we can use the earth tides to "calibrate" the observatory. Because of the well understood theory of the tidal potential and a quite accurate spherically averaged earth structure, it is straightforward to calculate the earth tide strains or tilt at any location for any azimuth. In the real world, however, perturbations to this theoretical earth tide are caused by ocean loads applying an addition signal at the same frequency but not in phase with the potential as well as the distortions to the strain field due to local inhomogeneities such as topography and geology.

In Section 5 we review the work of Berger and Wyatt (1973), Berger and Beaumont (1976), and Agnew (1979), who analyzed the strain tide observations at PFO and made calculations of the ocean load perturbations. Figure 2.17 shows the results for the semidiurnal tidal lines (Agnew, 1979). While there are certainly some errors in the models of the ocean tides used to calculate the ocean loads, it is likely that even larger errors are caused by inadequacies in the modeling of the local inhomogeneities. Nonetheless, the analysis gives us confidence that the observed strains are within 10-20 percent of our theoretical values and we have no reason to suppose that this conclusion cannot be extended to other frequencies.

There is another naturally applied strain field that we believe we can model fairly accurately and thus use as a test of our observations. This is the strain field that is produced when an earthquake occurs. We are considering here the static dislocation of the fault movement rather than the dynamics of the elastic wave generation.

Wyatt (1982b) examined the tilt and strain records recorded at PFO for the October 25, 1979, Imperial Valley earthquake. Although the theoretical displacements for the earthquake utilizing dislocation models are clearly not as accurate as the tidal modeling, the observations agreed to within 25 percent of the model with basically one free parameter, the seismic

moment, adjusted to fit three independent observations. Figure 2.14 shows the offsets recorded on two strainmeters (the third meter was rendered inoperative by the seismic accelerations which misaligned the laser beam). Figure 2.15 shows the residuals after removing the tides and the strains due to the dislocation model of the earthquake.

Both the tidal and seismic dislocation results give us confidence that, at least at periods of a day and less, the strain field we are observing at PFO is a quite accurate measure of the regional strain field.

As we extend our measurements to longer periods, however, and attempt to observe the secular strain over months and years we must face the questions of instrumental instability and local displacements that will cause noise in the records.

The initial design of the laser strainmeter to which the North-South and East-West components were built used long (~ 5 m) columns of block granite as fiducial points or end piers. These were set into holes drilled some 3 m into the surface material as described in Section 2.2 (see Figure 2.8). It was hoped that by this construction, the instruments would be detached from the surface layers that might be subject to environmentally caused displacements. This proved to be a false hope. Whenever there was a rainfall of over 2.5 cm, there would be large apparent strains recorded on both of these meters. A clear correlation with air or ground temperature was not apparent.

In an attempt to correct for these environmentally induced pier displacements, tiltmeters were attached to the piers at either end and the tilt along the axis of the strainmeter monitored (Wyatt, 1982a). Figure 2.16 shows the results for a six year section of the East-West strainmeter. The top curve shows the observed uncorrected strain. The next two curves are the pier tilts (converted to strain units). The pier tiltmeters are calibrated in a manner which allows for direct removal of the displacements due to tilts about the base of the end piers. The curve marked "Corrected Strain" in the figure is obtained by using this calibration when applying the East and West pier tilt corrections to the raw data. The lower curve demonstrates the improvement in the results when the pier tilt records are least squares fit to the strain record. The variance in the residual is decreased by nearly a factor of four and the value of the free parameter in the fit implies that the piers are rotating at a point significantly below their base.

The third of the laser strainmeters to be built was designed differently. As described in Section 2.2, its end piers consisted of nearly cubical granite blocks set on the floor of underground vaults. The base of these piers was approximately 3.5 m below the surface. The idea behind this design was that by eliminating the long thin columns, the sensitivity to pier tilts should be greatly reduced. The observed uncorrected records showed just this. Unfortunately, after the corrections for pier tilts were applied to the NS and EW components, the residual strain was apparently more free from environmental artifacts than the NW-SE. On that component, the pier tilts, not unnaturally, made little difference but yet the corrected strains showed an unrealistic secular trend in addition to usual rainfall effect.

As we discussed briefly in Section 2.2, the inability of the pier tiltmeters to improve the NW-SE strain records led us to install the optical anchor on the NW pier, late in 1979. Shortly after its installation, a $M_L = 5.3$ earthquake occurred on the San Jacinto fault at an epicentral distance of only 14 km from the observatory. Figure 2.17 shows a portion of the strain records for the NS and EW instruments around this time period. The offsets in the strain records have been removed but the residuals clearly show a strain "precursory" to the earthquake which we believe was caused by the heavy precipitation that occurred. (Just prior to the earthquake, 22.5 cm of rain fell on PFO in a nine day interval. The average yearly rainfall over the past nine years has been 25.4 cm.) Figure 2.18 shows the NW-SE strain both observed and corrected by a combination of the NW optical anchor and the SE pier tilt. The optical anchor record reveals that almost all of this anomaly was caused by a local displacement of the NW pier. The residual after removal of the optical anchor signal is remarkably smooth so we are able to see fluctuations on the order of 10^{-9} strain/day! Figure 2.19 shows the residual strains on all three com-

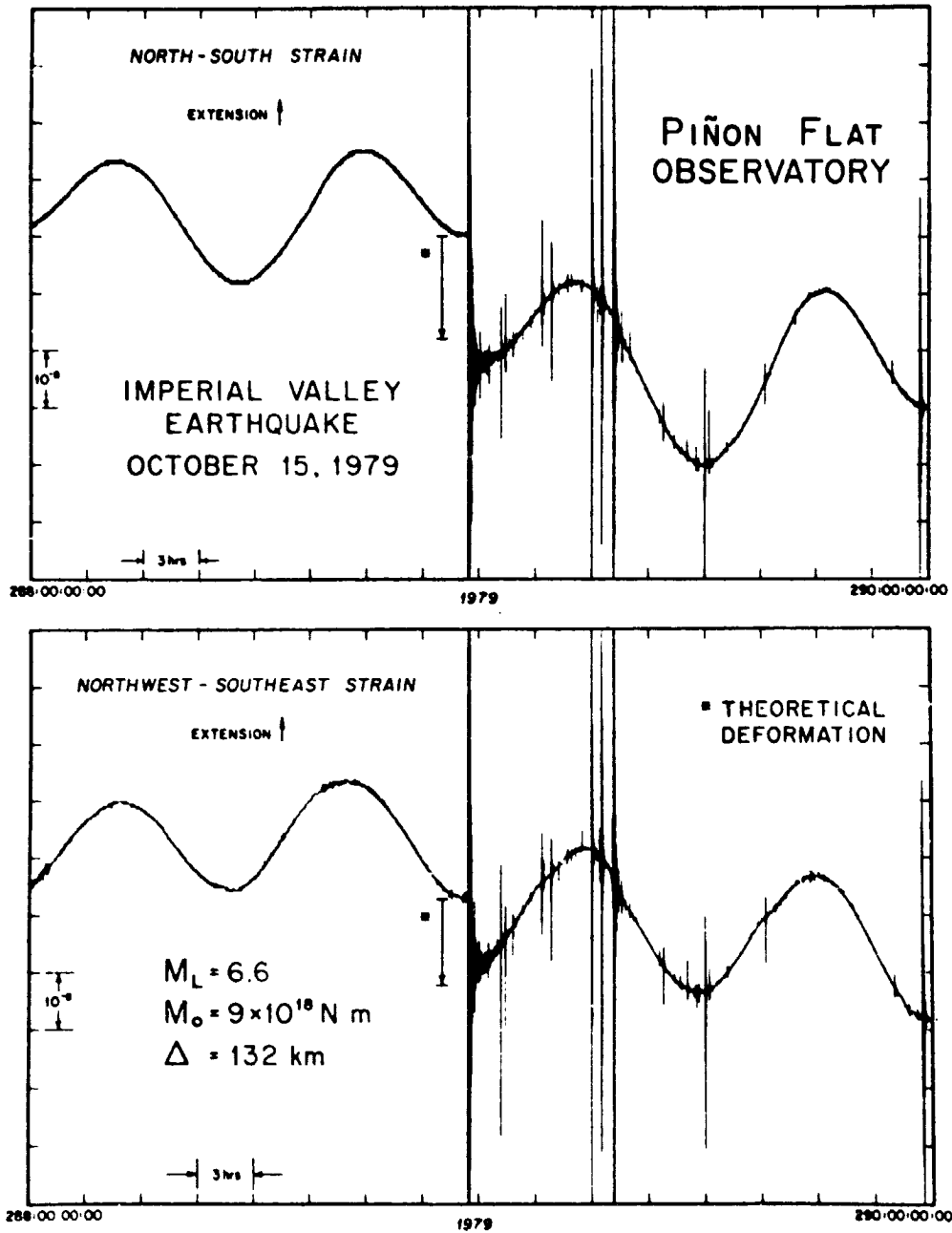


Figure 2.14 Deformation recorded by two of the long baselength strainmeters at PFO for a period of one day before and after the Imperial Valley earthquake (after Wyatt *et al.*)

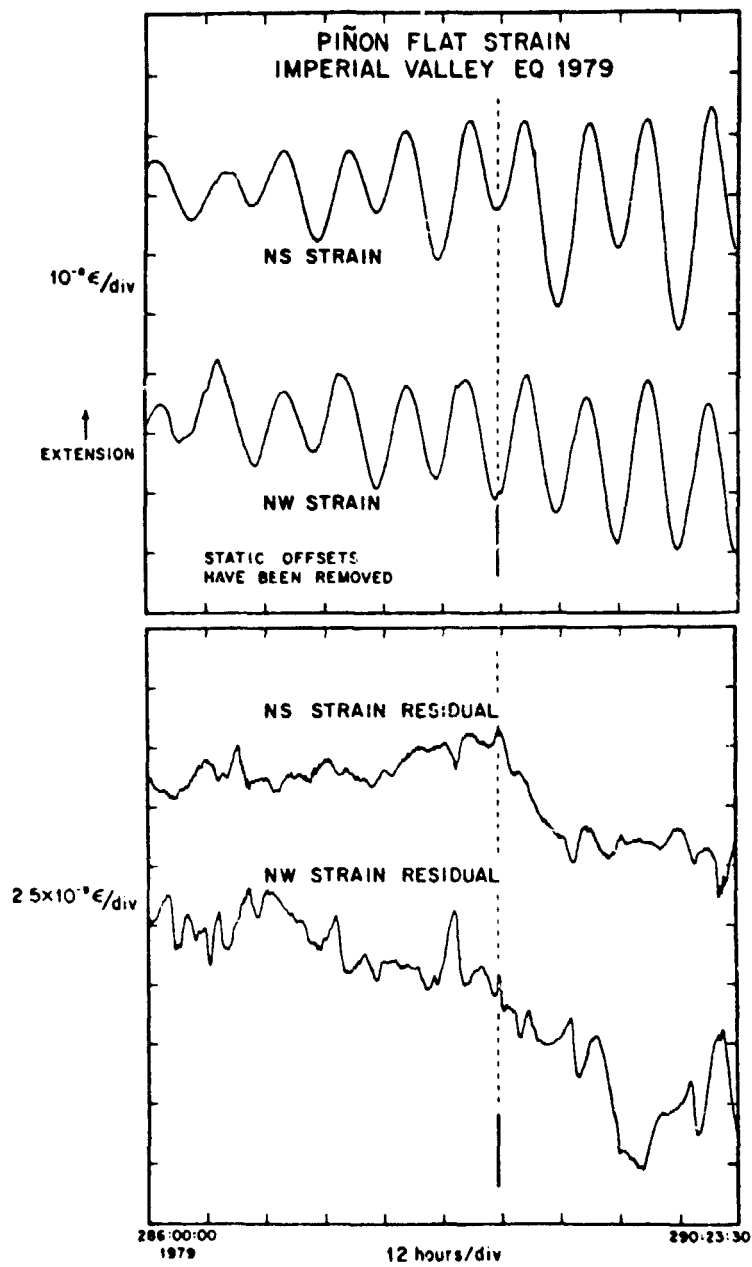


Figure 2.15. Possible post seismic deformation recorded by the North-South and Northwest-Southeast strainmeters at PFO. The lower traces were produced by removing the tidal components from the strain observations (after Wyatt *et al.*, 1982)

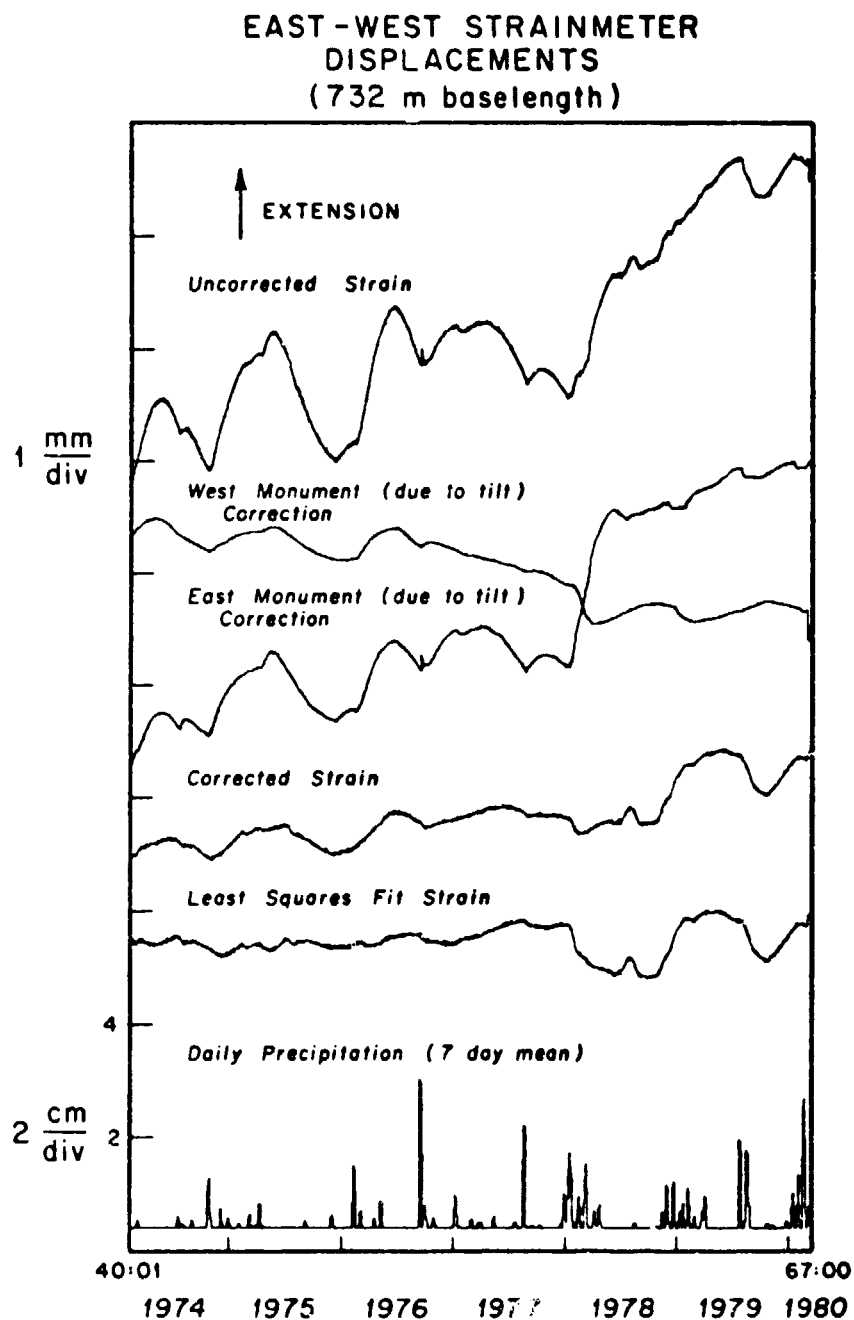


Figure 2.16 Records from the 731m East-West strainmeter at PFO, including the pier tilt series used to correct the strain observations (converted into equivalent displacements), and the strainmeter displacements corrected in two different manners. Also presented is the record of the daily precipitation

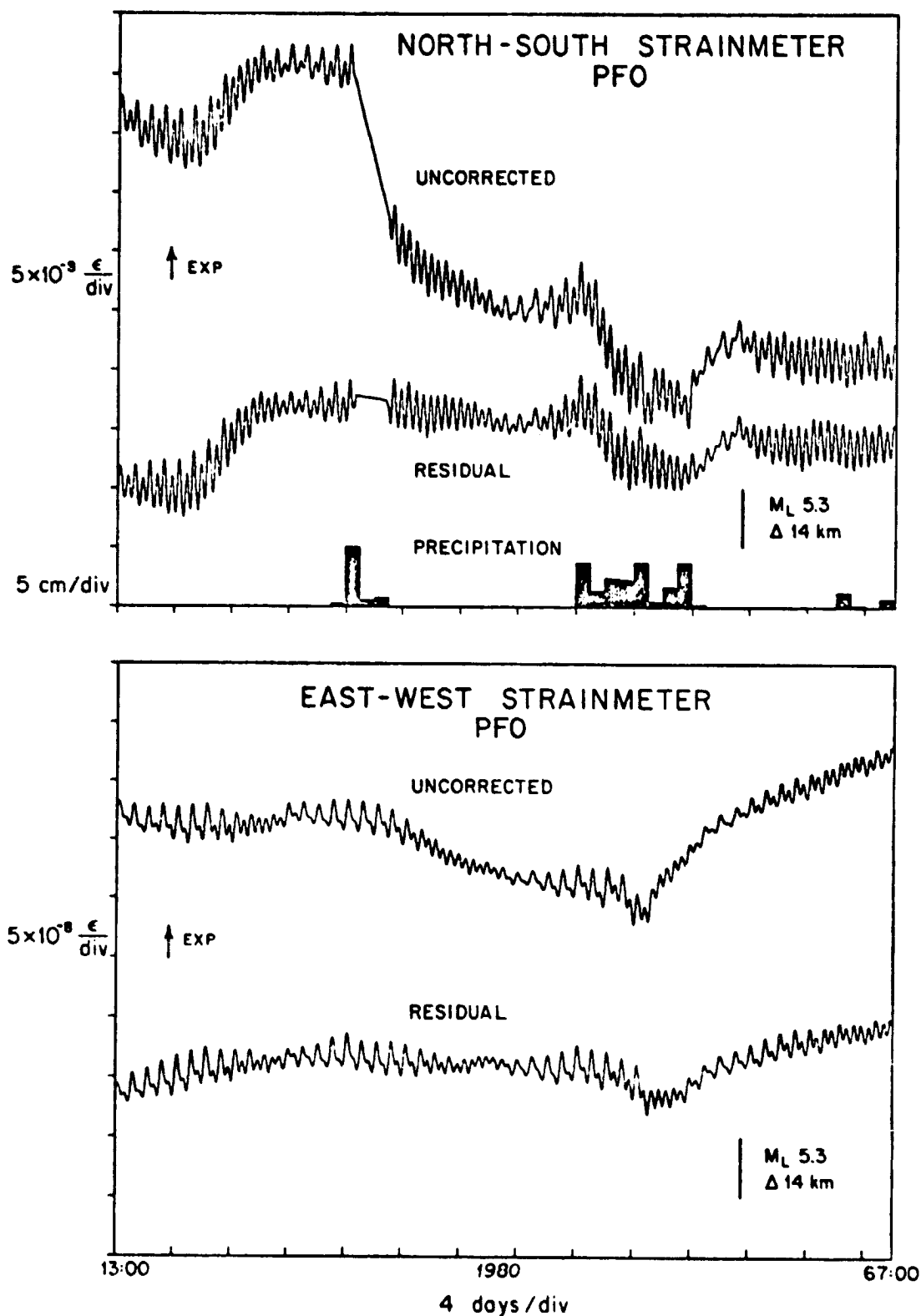


Figure 2.17 Strain records for NS and EW instruments before the $M_L = 5.3$ Horse Canyon earthquake.

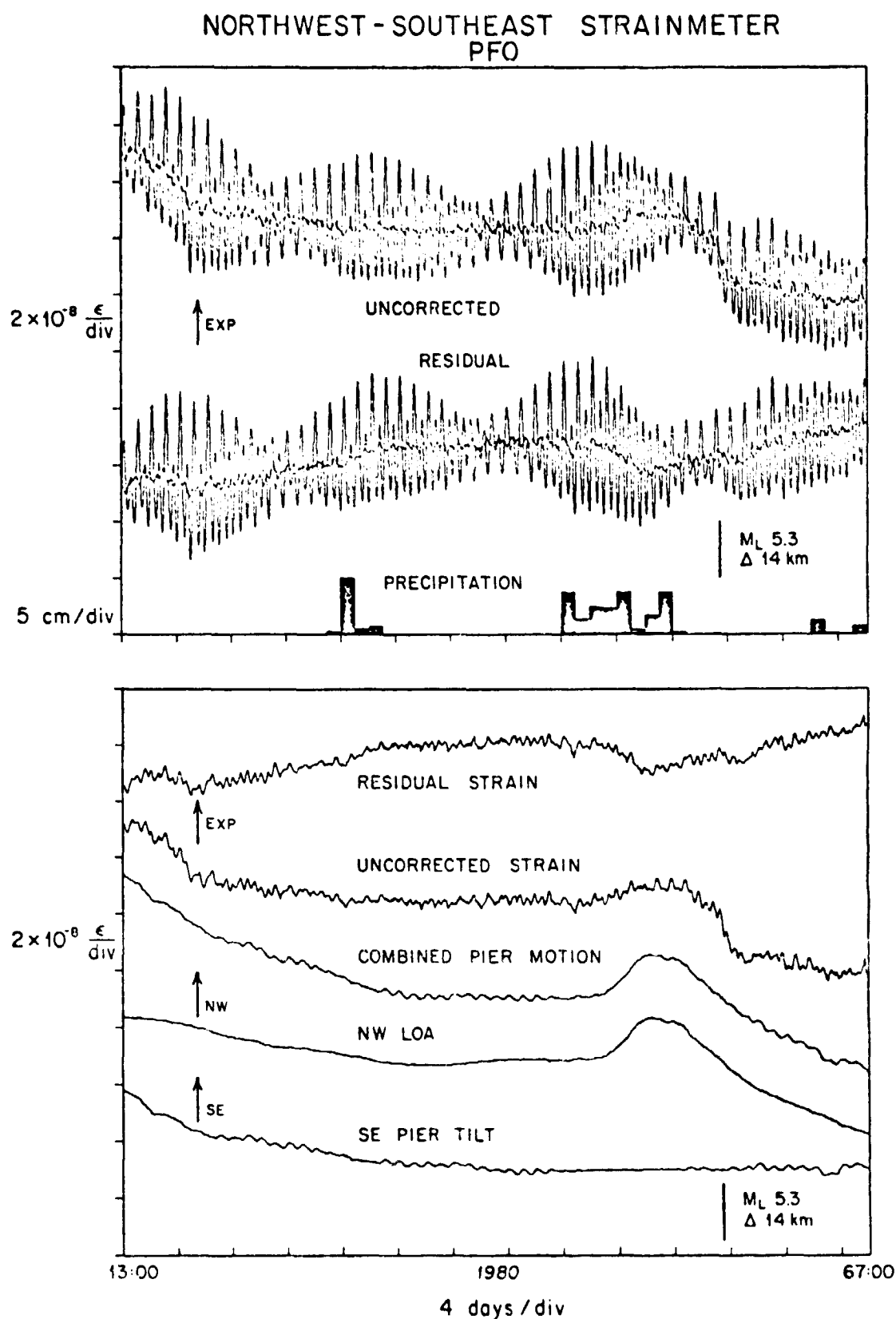


Figure 2.18 NW-SE strain observed and corrected by a combination of the NW optical anchor and SE pier tilt before the $M_L = 5.3$ Horse Canyon earthquake

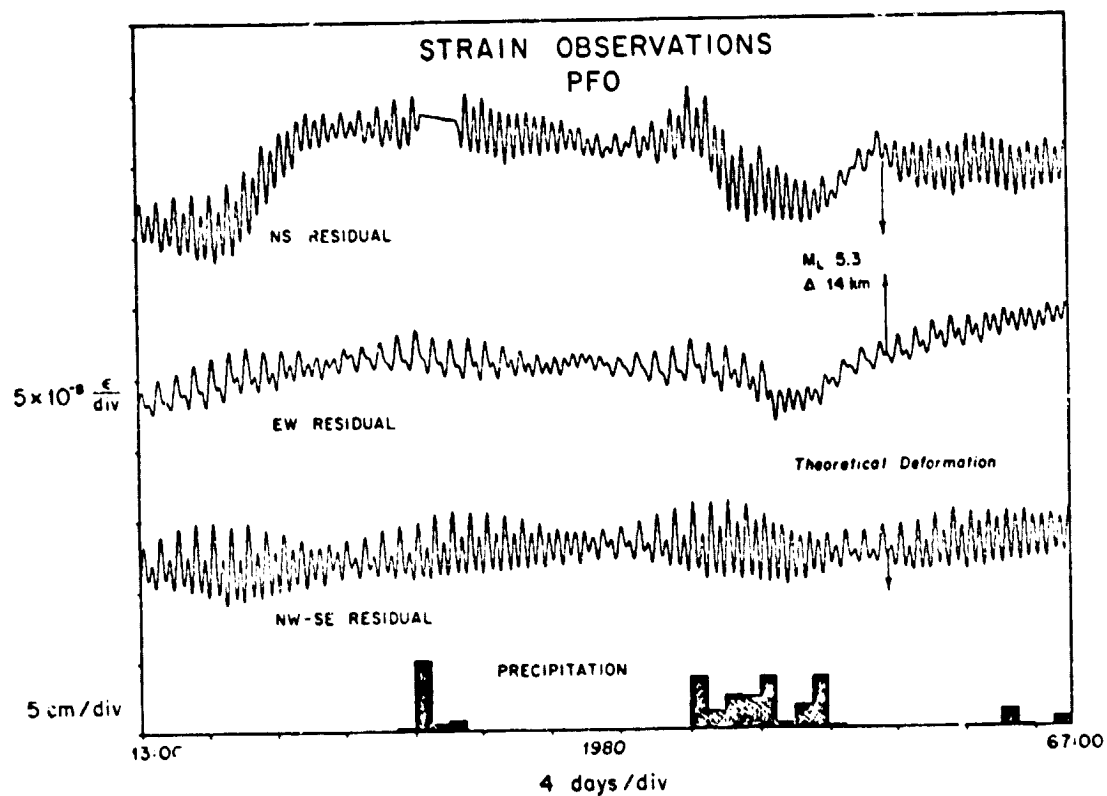


Figure 2 19 Residual strains on all three components for comparison for the $M_L = 5.3$ Horse Canyon earthquake

ponents for comparison. We anticipate that the corrected NW-SE strain signals will be reduced below the level of the current optical anchor corrections ($\sim 10^{-7}$ strain/year) once the SE optical anchor is installed and operating.

Figure 2.20 shows the results of applying the optical anchor corrections over the entire period of operation. To understand fully this data, and the longer record of the NW-SE strain presented in Figure 2.21, we must explain the following:

1. When the optical anchor was installed, the original granite strainmeter pier at the NW end was removed and a cement monument replaced it. (As the strain measurements at this end are now referenced to the points at a 24 m depth via the optical anchor, the surface pier need not be dimensionally stable.) We now believe that the secular strain rate up to this time was caused by a slow movement of the granite pier (which was not well constrained at its base) downslope towards the SE end.
2. Having discovered this, additional cement was added around the base of the SE pier at the start of 1980. This is reflected by the sharp inflection in the strain record at this time. Following this alteration, the SE pier's immediate response to rainfall was considerably reduced so that very little effect of the heavy rain in early 1980 can be seen in the strain record.

From 1980 onwards, the principal feature of the strain record is the bump near 1980.5 and the rise during late 1980. Neither of these two features is removed by the optical anchor correction and represents either continued SE pier motion (soon to be measured by the new SE optical anchor) or a real strain. Figure 2.21 shows the corrected strain observed at PFO over the past seven years. Also plotted in this figure are the strains deduced by analysis of the USGS Pinyon Trilateration Network (Savage, personal communication, 1981) and the local rainfall.

Perhaps the most striking feature of the PFO strains is the large NW-SE secular compression from 1974 to 1978. However, as we have explained in Section 2.2, we believe this result is wholly instrumental, being caused by a local movement of the end piers. The data on this component should have improved after the installation of the optical anchor on the NW end in late 1979. (The optical anchor on the SE pier is under construction at the time of this writing, October, 1981.)

The secular change in the NS and EW components is much less. The agreement with the geodetically determined strains is remarkably good at least up until late 1978. At that time, there seems to have been a change in the normal strain pattern reflected in both sets of data. Indeed, a change in the strain pattern in all of southern California was noted to occur at about this time (Savage *et al.*, 1981). It is not at all unlikely that the differences between the geodetically determined strains and those from the strainmeters of PFO represent spatial inhomogeneities in the strain field.

Figure 2.22 shows the results of the USGS trilateration network called ANZA and a sub-network referred to as Pinyon (see Figure 2.4). The former is a point network spanning the Elsinore, San Jacinto, and San Andreas faults while the latter is an 11 station network centered on PFO. In theory, if the assumptions of homogeneity and temporal stability that are used to reduce the line length changes (Savage *et al.*, 1981) to strains are valid, then one would expect these networks to give the same strains with the smaller network having larger error bars.

In general, the results of the two networks do agree but the differences between the two may reflect spatial inhomogeneities in the strain field on the order of the observed strains. Thus, we are not surprised to see differences in the strains determined at PFO and those of the encompassing trilateration network.

Almost all the major fluctuations of the PFO strain records about their linear trends can be attributed to the local effects of rainfall. There may be one or two fluctuations about the trends not coincident with a local rainfall that can be seen upon close examination of the records but these are of small amplitude and dubious significance. We cannot explain the apparent change in response to rainfall of both the North-South and East-West components

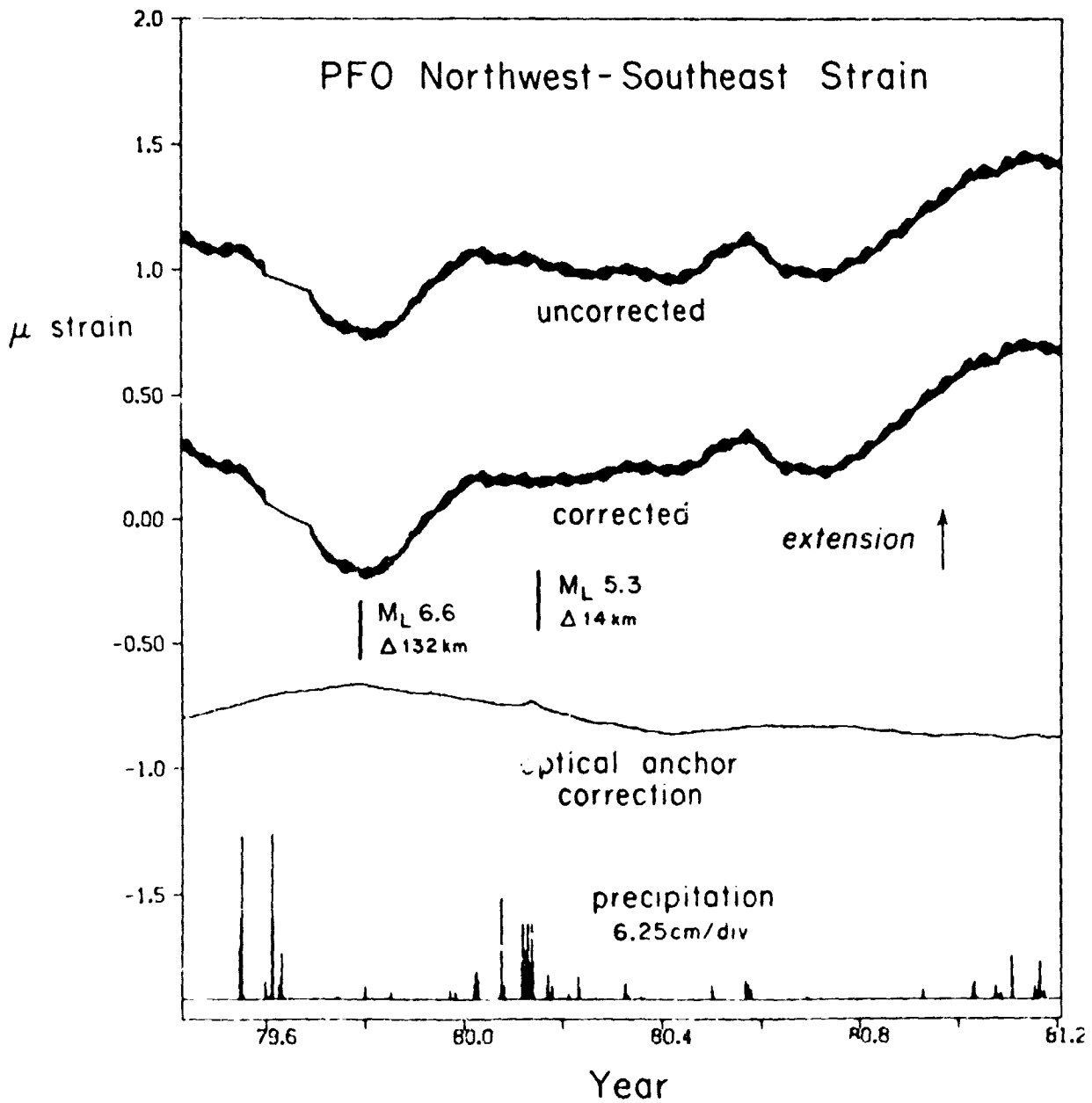


Figure 2.20 NW-SE strain observations corrected for monument displacements at one end only

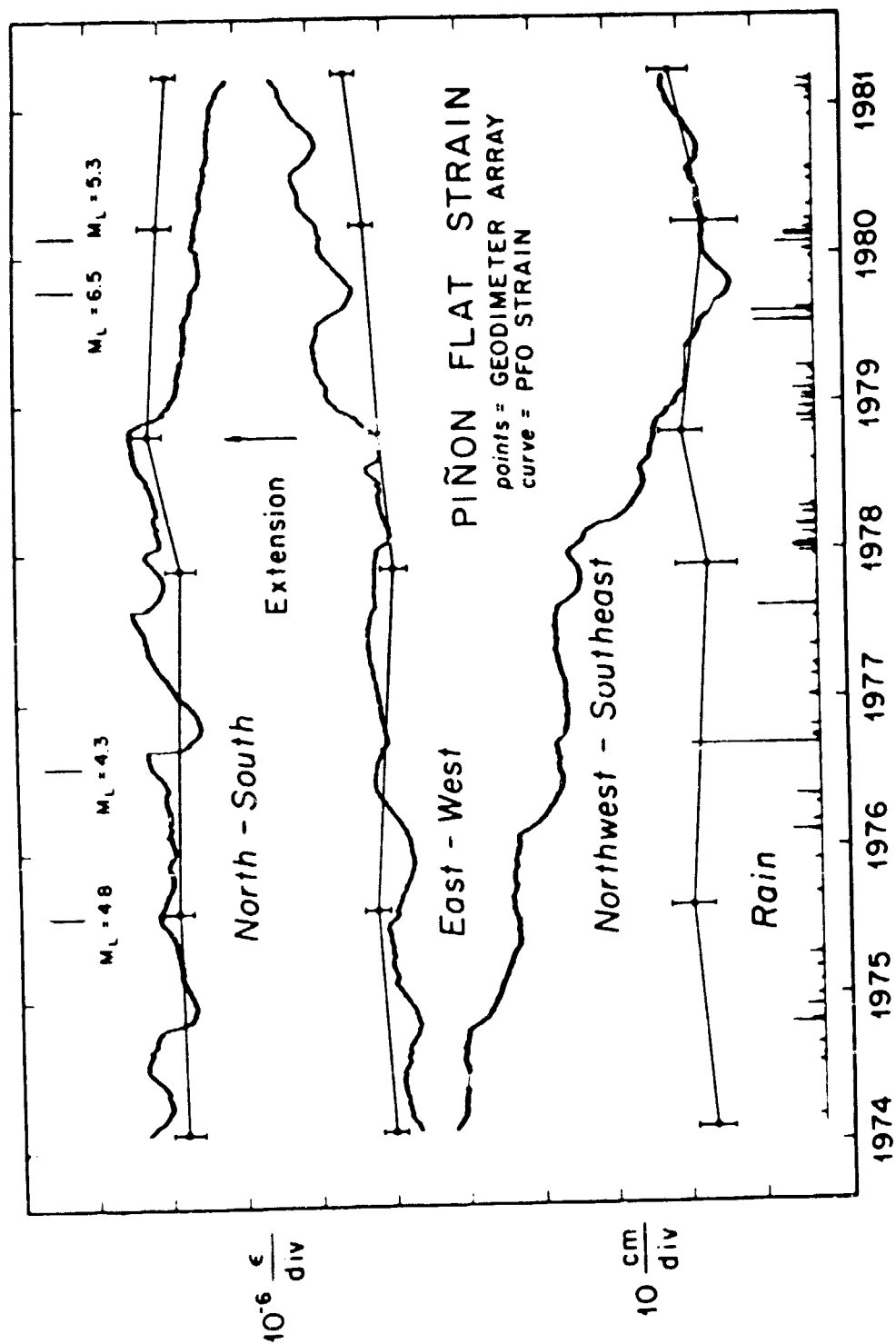


Figure 2.21 Secular strain observed at PFO over the past seven years with results from the Pinyon Geodetic Network.

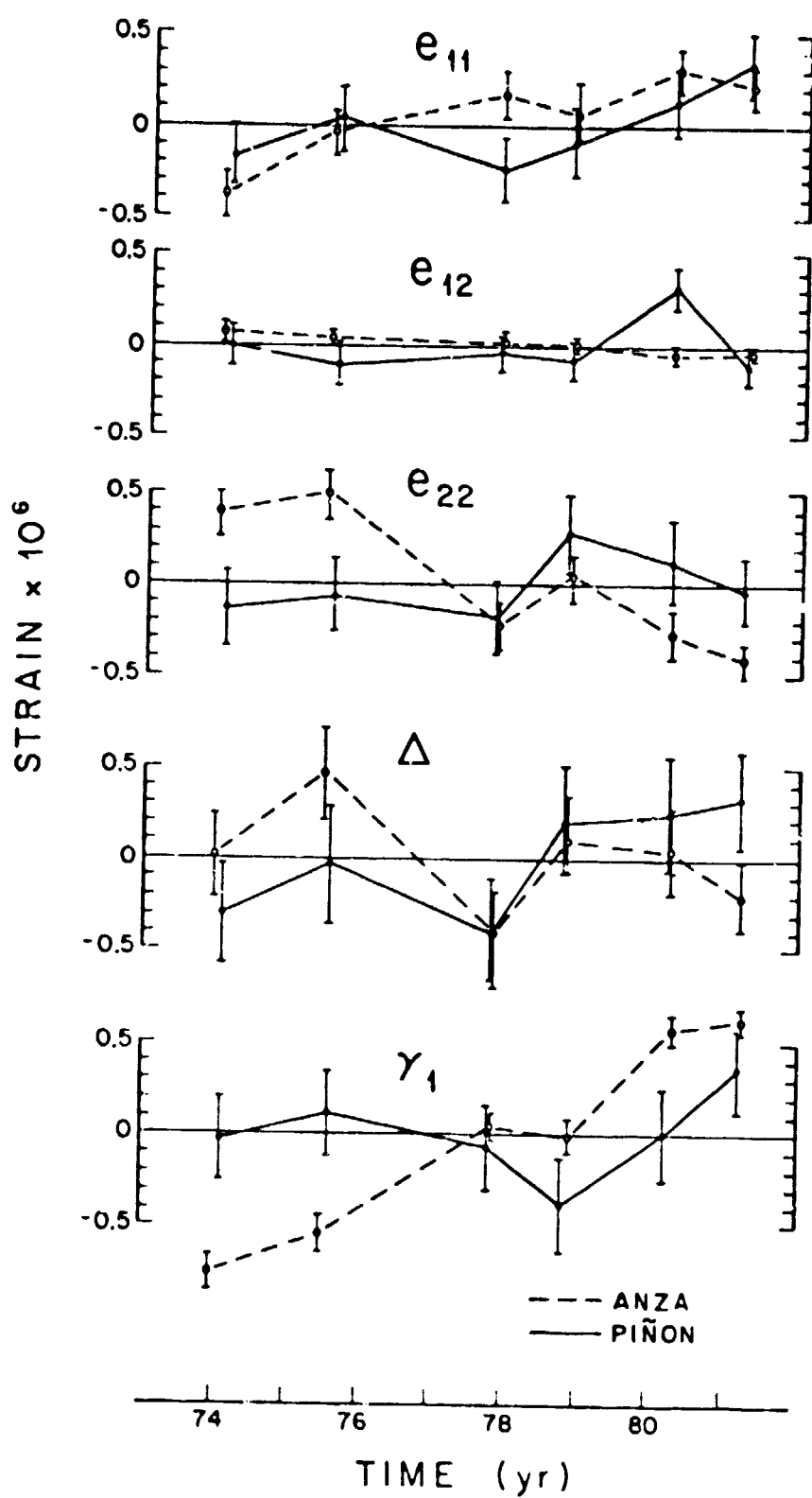


Figure 2.22 Results of USGS Anza trilateration network and the Piñon subnetwork

occurring in late 1978. It seems unlikely that this is connected with the regional change in the strain field mentioned above but may very well be related to the change both locally and in all of southern California from an epoch of drought to one of more normal precipitation.

In summary, using the deformation data from PFO observed over the past seven years we can:

1. Compare deformation observed at PFO with deformation deduced from a trilateration network which encompasses the observatory.
2. Determine upper limits on the rate of change of deformation (strain and tilt) to be expected.

1. Comparison of strain. As we have shown from the strain observations at PFO over the period 1974-1981 and the results from the USGS Pinyon Trilateration Network, the long term secular strain recorded in the North-South and East-West directions agree with the trilateration results as well as might be expected considering the difference of the two techniques. The results from PFO are within two standard deviations of the trilateration net data. The Northwest-Southeast strainmeter, however, has not produced consistent secular strain rates. We believe the reason for this has to do with the details of the attachment of the instrument to the earth (Wyatt, *et al*, 1981). Recent additions to this instrument have improved the characteristics of the records greatly.

2. Rate of strain. With regard to the time variations of the strain, almost all of the obvious fluctuations in the three strain records are correlated with local rainfalls of 2.5 cm and larger. Wyatt (1982a) has made a thorough study of near surface displacements and concluded that these signals are artifacts of the local motion of the end monuments--the strainmeter attachments points. Thus, these records must be taken as overestimates of the normal background strain noise. Perhaps the most succinct way to summarize this data is to calculate the averaged power spectrum of the three records. Figure 2.23 shows the results. Table 2.3 gives the average standard deviation in a one decade bandwidth centered at a set of discrete frequencies. (This bandwidth was chosen to obtain agreement with intuitive estimates of the "amplitude" spectrum for a power spectrum whose frequency dependence is approximately $1/f^2$.) In general, if we eliminate artifacts obviously caused by rain, seismic and tidal signals, we have seen no strain changes at periods shorter than the average repeat time of the trilateration nets greater than 7×10^{-7} that appear on two or more instruments. (While it is possible to produce a deformation that changes only one component of strain, it is extremely unlikely to occur in nature. Hence, we label as instrumental or environmental artifact those strain changes seen on one instrument only.)

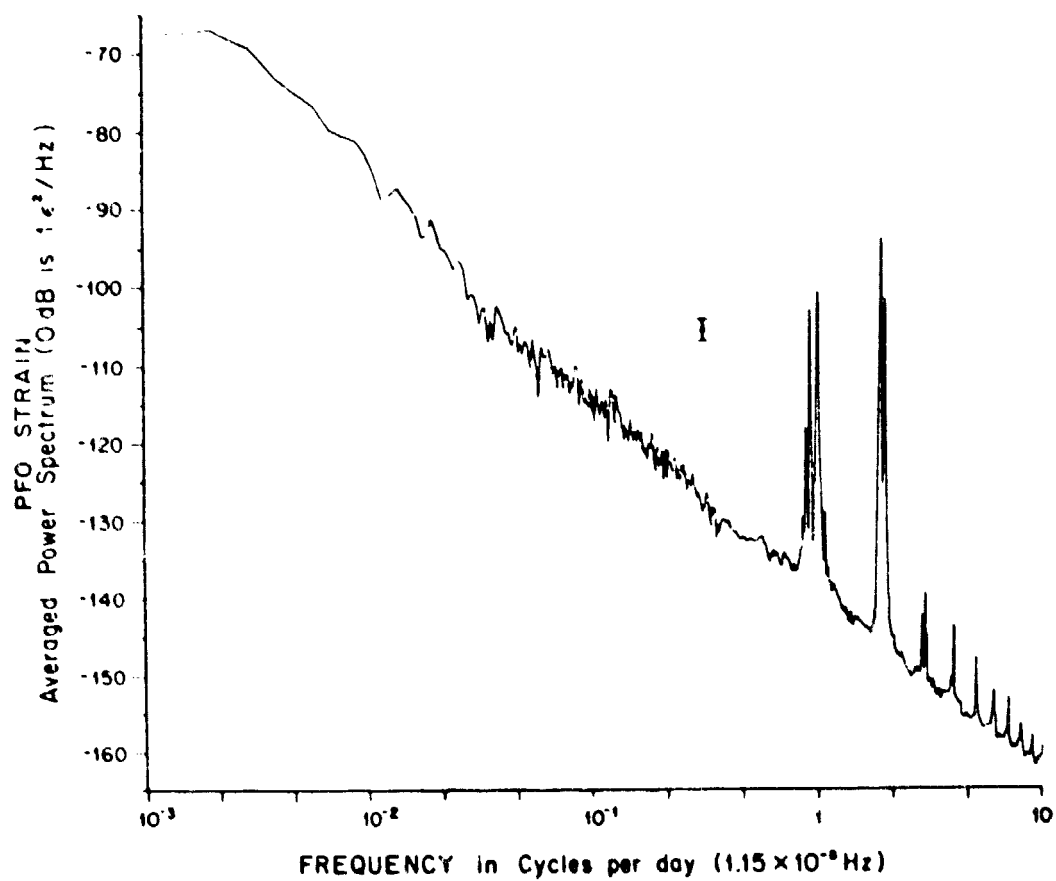


Figure 2.23 Averaged power spectrum of the PFO secular strain

Table 2.3

Average Standard Deviation in a One Decade Bandwidth centered
at a Set of Discrete Frequencies

Frequency Cycles Per Day	Power Spectral Density Relative to ϵ^2/Hz	Standard Deviation In a One Decade Bandwidth
.001	- 68 dB	$1.8 \times 10^{-7} \epsilon$
.01	- 85 dB	$2.8 \times 10^{-8} \epsilon$
.1	-112 dB	$3.3 \times 10^{-9} \epsilon$
1.0	-140 dB	$5.4 \times 10^{-10} \epsilon$
10.0	-162 dB	$1.4 \times 10^{-10} \epsilon$

3.0 Seismicity Studies Related to the Gulf of California

During this project we have had close ties with Mexico in connection with operation of the Northern Baja California seismic array and other seismicity studies in Mexico. One Mexican graduate student in seismology, Luis Munguía, is currently completing his Ph.D. Alejandro Nava completed his Ph.D. in March, 1980. Alfonso Reyes, Chief of the Geophysics Department of CiCESE (Centro de Investigaciones Científicas y de Educación Superior de Ensenada), did his graduate work at IGPP and is now completing his Ph.D. thesis.

We have recently completed studies of the seismicity of Northern Baja California (Brune *et al.*, 1979); the structure of Northern Baja California (Nava and Brune, 1981a); the source mechanism of two Northern Baja California earthquakes (Nava and Brune, 1981b); aftershocks of the Oaxaca earthquake of November 29, 1978 (Reyes *et al.*, 1980); spectra of aftershocks of the Oaxaca earthquake (Munguía *et al.*, 1980); and the location of the hypocenter of the Imperial Valley earthquake of October 15, 1979 (Chavez *et al.*, 1981). At the present time, we are preparing papers on a recent swarm of earthquakes which occurred in the Laguna Salada region (Reichle and Simons, in preparation, 1981), on aftershocks of the Petatlán earthquake of March 1979 (Suarez and Reichle, 1979), and on the source mechanism and aftershocks of the recent Victoria, Baja California, Mexico earthquake of June 1980.

Brune *et al.* (1979) summarized the current evidence relating to seismicity and faulting in Northern Baja California. The area is one of extremely high seismicity, at least 13 earthquakes of magnitude greater than six have been recorded since 1900. Activity on the San Miguel Fault is particularly high. Relocation of the 1954 Baja California earthquakes indicates that they were on the San Miguel Fault (and not on the Agua Blanca Fault as had been suggested earlier). On August 19, 1978, a small earthquake ($M \sim 3.5$) occurred on the San Jacinto Fault zone just southeast of Tijuana, emphasizing the possible hazard to Tijuana and San Diego. The region of the Mexicali Valley is the locale of the main plate boundary and the seismicity there is the highest in the region, posing a severe seismic hazard to the city of Mexicali.

Recently, Nava and Brune (1981a) completed an explosion-earthquake reversed refraction profile in the Northern Peninsular Ranges between Corona, California and Valle de Trinidad, southeast of Ensenada. They found a relatively high velocity crust (6.6 to 7.0 km/sec) and a crustal thickness of ~ 40 km.

Nava and Brune (1981b) also compared two earthquakes, one from the Salton Trough region and the other from the granite Peninsular Ranges. They found that the main difference between the two earthquakes was the complexity and much higher relative excitation of surface waves by the Salton Trough event as compared to the relatively simple nature and low excitation of surface waves for the Peninsular Ranges event.

In a study of the Oaxaca earthquake of November 29, 1978, Reyes *et al.* (1980) analyzed the aftershock sequence distribution along with teleseismic data. The overall analysis suggests that the rupture process associated with this earthquake cannot be interpreted in terms of simple plate tectonic processes. One interpretation explains the fact that the heaviest damage was in the high elevation regions: the rupture probably started at the intersection of two faults, propagating toward the trench axis and therefore, focusing its energy along this direction. The increased stress field due to the propagation of the initial break probably increased the stress on the secondary fault triggering a second event that most likely focused its energy toward the high elevation regions. This secondary fault probably stopped the main fault from extending into the deepest regions of the major plate boundary. However, this explanation does not account for the lack of damage in the lowlands along the coast, where the heaviest damage would be expected because of amplification effects in the low rigidity sediments. A second interpretation consistent with the teleseismic data was formulated. The main rupture started along the secondary fault propagating parallel to the trench axis from the deepest part of the fault toward the high elevation regions. This propagation obtained from the P wave teleseismic data, but it adds complexities to the rupture processes along the subduction zones.

Munguía *et al.* (1980) are currently studying a swarm which occurred in March, 1978 near the town of Victoria, Northern Baja California. They found that many of the larger quakes occurred at depths of ~ 15 km. Hypocenters in the Salton Trough, where the faults are usually covered by ~ 5 km of sediments, are usually relatively shallow (~ 10 km) and in the large part confined to the sedimentary section. Thus, the depth of these earthquakes was surprising, as were the apparent high stress drops for these events, some as high as 1 kilobar (typical stress drops for large earthquakes are ~ 30 -100 bars). We are currently studying this swarm and the study will constitute part of the Ph.D. thesis of Luis Munguía.

Chavez *et al.* (1981) studied the October 15, 1979 Imperial (Mexicali) Valley earthquake, $M_L = 6.6$, which occurred in the vicinity of several permanent seismic networks operating on both sides of the international border. Because the event lay outside the individual arrays, initial locations calculated using the data from any one group of stations were misleading, incorrectly placing the epicenter in the United States. By pooling the arrival times from all systems, however, complete azimuthal coverage was obtained and a reliable hypocentral solution was produced. The mainshock epicenter was located 3 km south of the international border, approximately 10 km east of Mexicali, Baja California Norte, Mexico. The 9.96 km depth obtained is slightly greater than the 6 to 8 km average depth for Imperial Valley earthquakes (Johnson, 1979). The significance, if any, of this is not well understood at this time. The greater depth can help explain, however, the fact that although the earthquake took place within Mexico, the only surface rupture observed was north of the border.

Reichle and Simons are preparing a paper for publication on a lengthy earthquake swarm (December 1975 - June 1976, several $M \sim 5$) which occurred near Laguna Salada, Northern Baja California, Mexico. The swarm is being studied with California Institute of Technology and the then existing Northern Baja California station data. Since this swarm did not occur along the most active branches of the Plate boundary (the Imperial-Cerro Prieto Faults), it may provide insight into the transfer of seismicity from the Gulf of California system to the various Southern California faults.

On 9 June 1980, at 03:28:20 (GMT), an earthquake of magnitude 6.2 (M_L) occurred in Mexicali Valley, Northern Baja California, Mexico. The instrumental epicenter was roughly 10 km southeast of the town of Guadalupe Victoria. Four hours after the main event, the first of a portable array of seven analog and 12 digital seismic event recorders, both from CICESE and IGPP (UCSD), began recording the aftershock activity.

The last recorder was removed from the region on 5 August 1980, following the accumulation of over 50 smoked-paper records and 60 digital cassettes containing aftershock data. The contents of all cassettes have been transferred to computer-compatible tape and time corrections have been determined for all stations. All usable signals have been edited from the computer-compatible tapes and archived.

Investigators at CICESE have located many of the aftershocks of the Victoria earthquake. They are clustered principally on a segment of the Cerro Prieto Fault close to the two communities, Victoria and Pescaderos, which experienced the greatest damage from the mainshock. A number of events are also found scattered throughout the area between the southern end of the Imperial Fault and northern end of the Cerro Prieto Fault. The instrumentally determined epicenter of the mainshock (based on initial P arrivals at nearby USGS and Mexican stations) is near the Cerro Prieto Fault, but is approximately 15 km southeast of the region of aftershocks and major damage. A similar phenomenon characterized the 15 October 1979 event on the Imperial Fault (Chavez *et al.*, 1981).

Additional work at CICESE on the aftershocks of this event includes focal mechanism studies and a comparison of this event with previous events on the same fault system. At IGPP, S-wave spectra are being computed from some of the largest aftershocks.

An important aspect of the Victoria mainshock is the strong motion record obtained at a station in the town of Victoria. Vertical accelerations there exceeded $1g$ in both the positive and negative directions for several cycles, and the horizontal acceleration reached $.85g$.

Soon after the Victoria earthquake, the region was inspected carefully from the air and on the ground by observers from both IGPP and CICESE. Many fissures and sand blows and other surface manifestations were seen striking roughly perpendicular to the strike of the Cerro Prieto fault system. However, no surface features paralleling the fault system were detected. This contrasts sharply with observations of surface faulting on the Imperial fault following the 15 October 1979 Mexicali event.

4.0 Development of the Superconducting Gravimeter

This work was motivated by data obtained with our superconducting gravimeter at PFO. That data indicated that variations in gravity of about $\pm 5 \mu\text{gals}$ could be observed over arbitrarily long periods of time. Using funds from this grant, and several others, five instruments were built in 1978 for deployment to new sites. The object was to measure non-periodic variations in gravity at various locations to attempt to measure vertical crustal motion and to learn what the limitations on such measurements might be. Ultimately, the results were to be interpreted, along with spaceborne measurements of crustal motion, to give complete information on vertical and horizontal motion and associated mass displacement beneath the surface.

Subsequently, instruments were operated at Otay Mountain (San Diego), Lytle Creek (north of San Bernardino), The Geysers (near Santa Rosa), Boulder, Colorado, and Greenbelt, Maryland. At Greenbelt, very severe problems with electrical interference were encountered so that only very short segments of useful data were obtained. The results from the other stations are summarized in Table 4.1. Plots of data after removal of tides and barometric pressure effects are shown in Figures 4.1—4.5. Some comments on the results are included in Table 4.1. We conclude that some "events" were observed on the gravity field at The Geysers, and a slow drift in gravity was observed at Lytle Creek until about two months before the instrument was turned off. The other stations reveal no significant variations in gravity within limits of $\pm 5 \mu\text{gal}$ except at Otay Mountain where large tilts produced artificial variations of $\pm 10 \mu\text{gal}$.

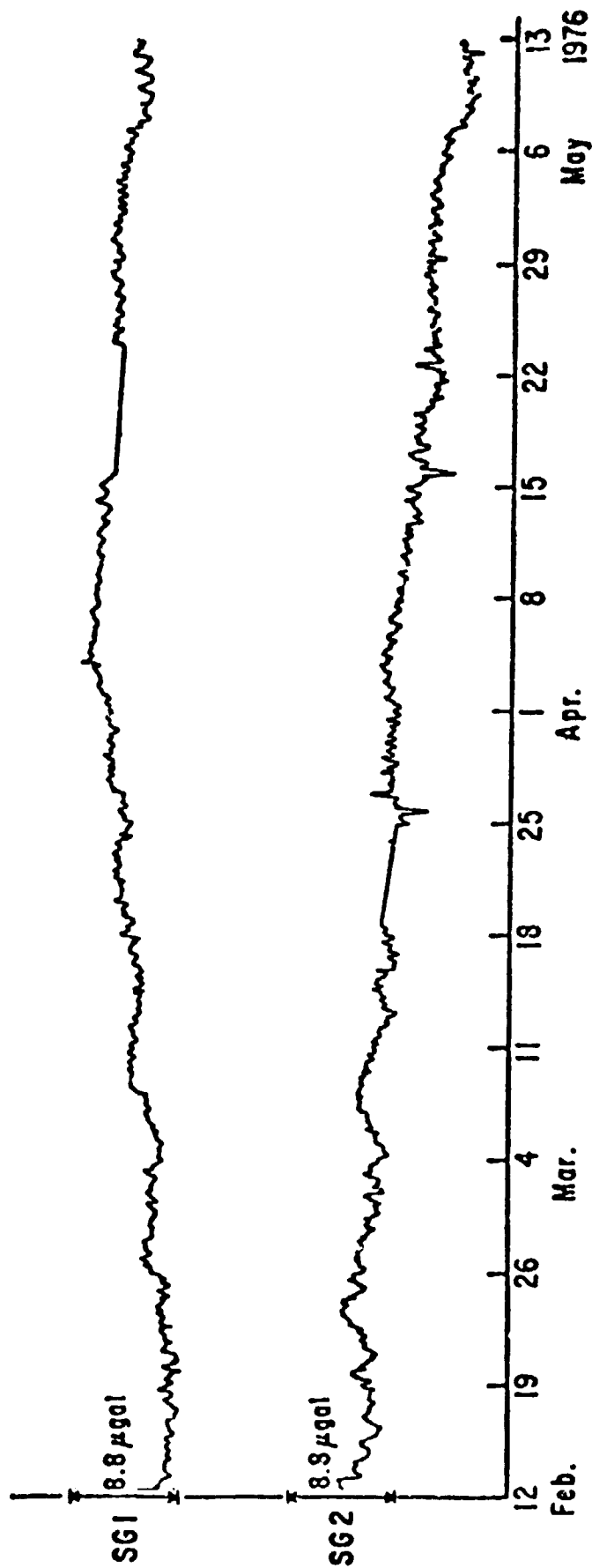
At the time of these measurements all of the instruments were operated singly at isolated locations so that it was not possible to prove that the different results were a consequence of different operating characteristics of the various instruments. Our most recent work has concentrated on this question by returning all of the instruments to the lab for simultaneous side-by-side testing. Some sources of spurious noise have been identified and eliminated and others are still being diagnosed. However, no long term drift has yet been found. It is found that two properly operating instruments produce signals which are identical to within less than $0.2 \mu\text{gal}$. This means that the $\pm 5 \mu\text{gal}$ fluctuations are probably real changes in gravity which must be understood. It also means that long term observations, which average over these fluctuations (characteristic time of order one week), will determine steady gravity variations to better than $5 \mu\text{gal}$.

In summary, the project successfully measured gravity variations at several locations to within $5 \mu\text{gal}$. Subsequent work has shown that the superconducting instruments can measure gravity variations to within about $\pm 0.2 \mu\text{gal}$.

Table 4.1

Superconducting Gravimeter Results

	Length of Record	Noise in tide band μgal per root cycle/day	Peak-to-Peak fluctuation in gravity residual μgal	Net change in Residual gravity over duration of record μgal	Type of tilt correction	Comments:
PINON FLAT	3 year	0.10	< 10	0 \pm 10	Instrument leveled at intervals between 3 and 6 months. No significant changes.	The first 18 months were obtained with the first model of the instrument which lacked stabilizing coils. A steady drift of + 40 $\mu\text{gal}/\text{year}$ was removed from that segment of the data.
OTAY MOUNTAIN	1 year	0.11	< 20 atmospheric effect not yet removed	- 30 during 1st and last month of operation. 0 during 10 month period.	Reveled at intervals. Very large tilts leave large errors in signal during 1st and last month of operation.	Tilt coefficient is uncertain. Further analysis should reveal if drifts during first and last month were due to tilt.
LYTLE CREEK	1-1/2 year	0.15	< 10 < 5 when corrected for tilt	steady -0.28 $\mu\text{gal}/\text{day}$ for 1 year, then 0 for 90 days to end of record	Tilt measured by external tiltmeters during last 6 months of data.	This was the only site at which a steady long term drift was observed. This was followed by an abrupt change of drift to zero for the last 3 months of operation.
THE GEYSERS	150 days 38 days more to be analyzed	0.5	< 10	- 20	Tilt stabilized platform controlled by tiltmeters mounted on top of Helium vessel.	Events as large as 40 μgal which developed over a period of 10 hours are observed here but at no other sites.
BOULDER COLORADO	280 days	0.5 some broadband coherent power in tide band.	< 10	+ 7 \pm 5 for last 170 days of record. 1st 110 days drifted 20 μgal due to electrical problems.	None. Tilts could account for 3 to 5 μgal .	Artificial noise and drift created by electrical problems was eliminated in the middle of the record.



Gravity residuals for SG1 and SG2 at Piñon Flat Observatory after subtraction of the effects of atmospheric pressure. Gravity increases towards the top of the graph.

Figure 4.1 Plots of data after removal of tides and barometric effects.

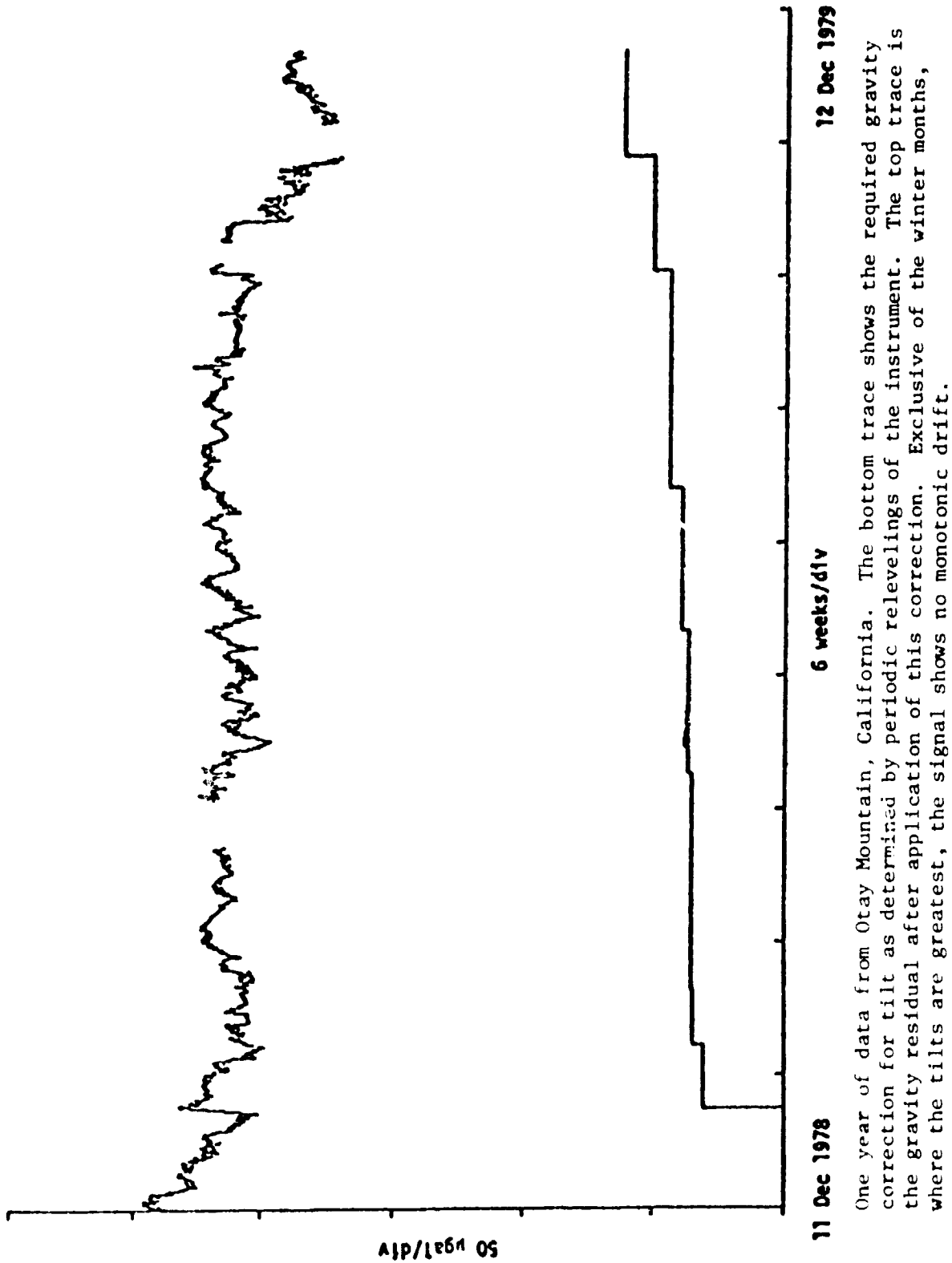
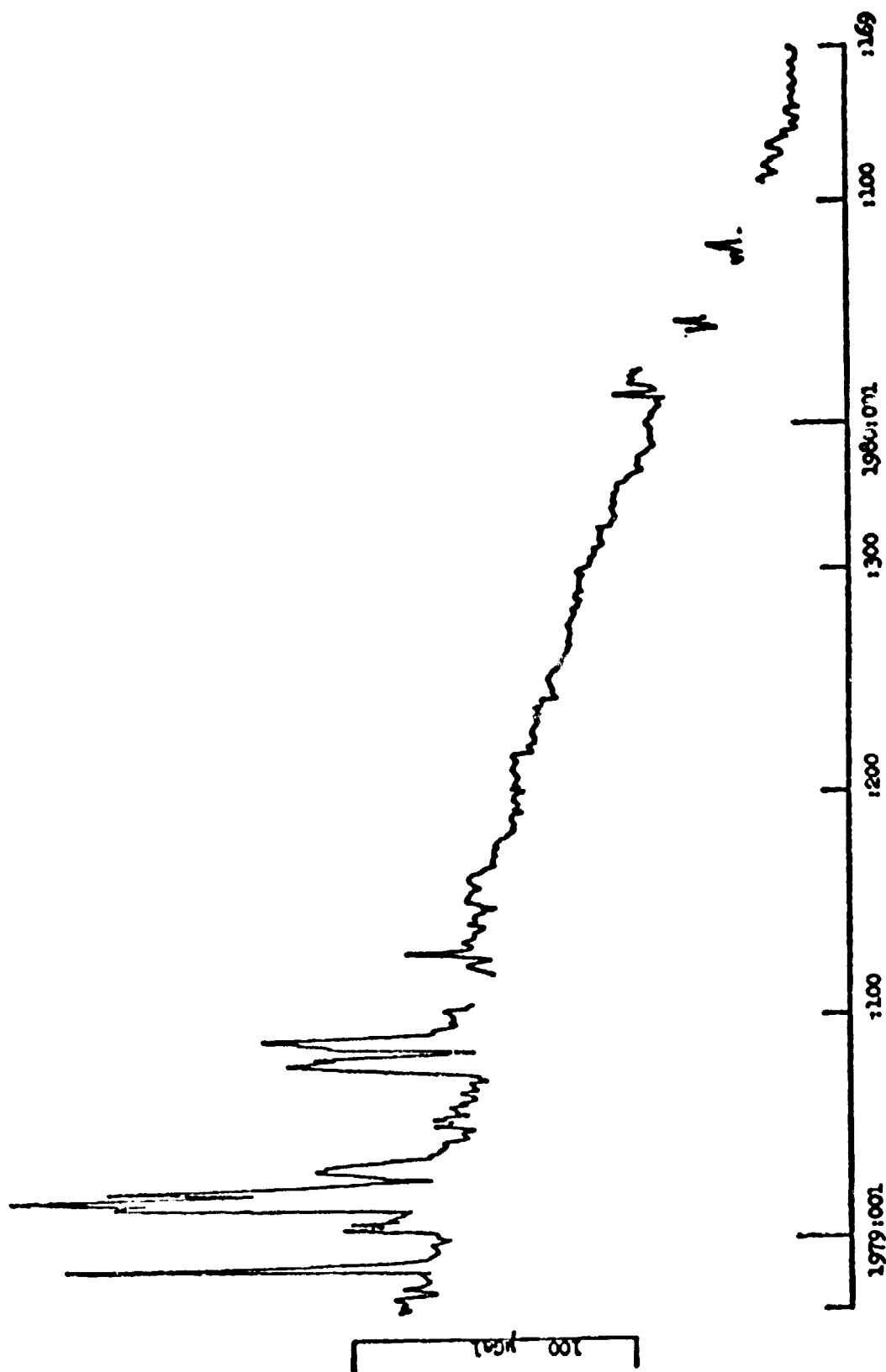


Figure 4.2 Plots of data after removal of tides and barometric effects



A 566-day gravity residual from Lytle Creek, California, beginning November 30, 1978 and ending June 17, 1980.

Figure 4.3 Plots of data after removal of tides and barometric effects.

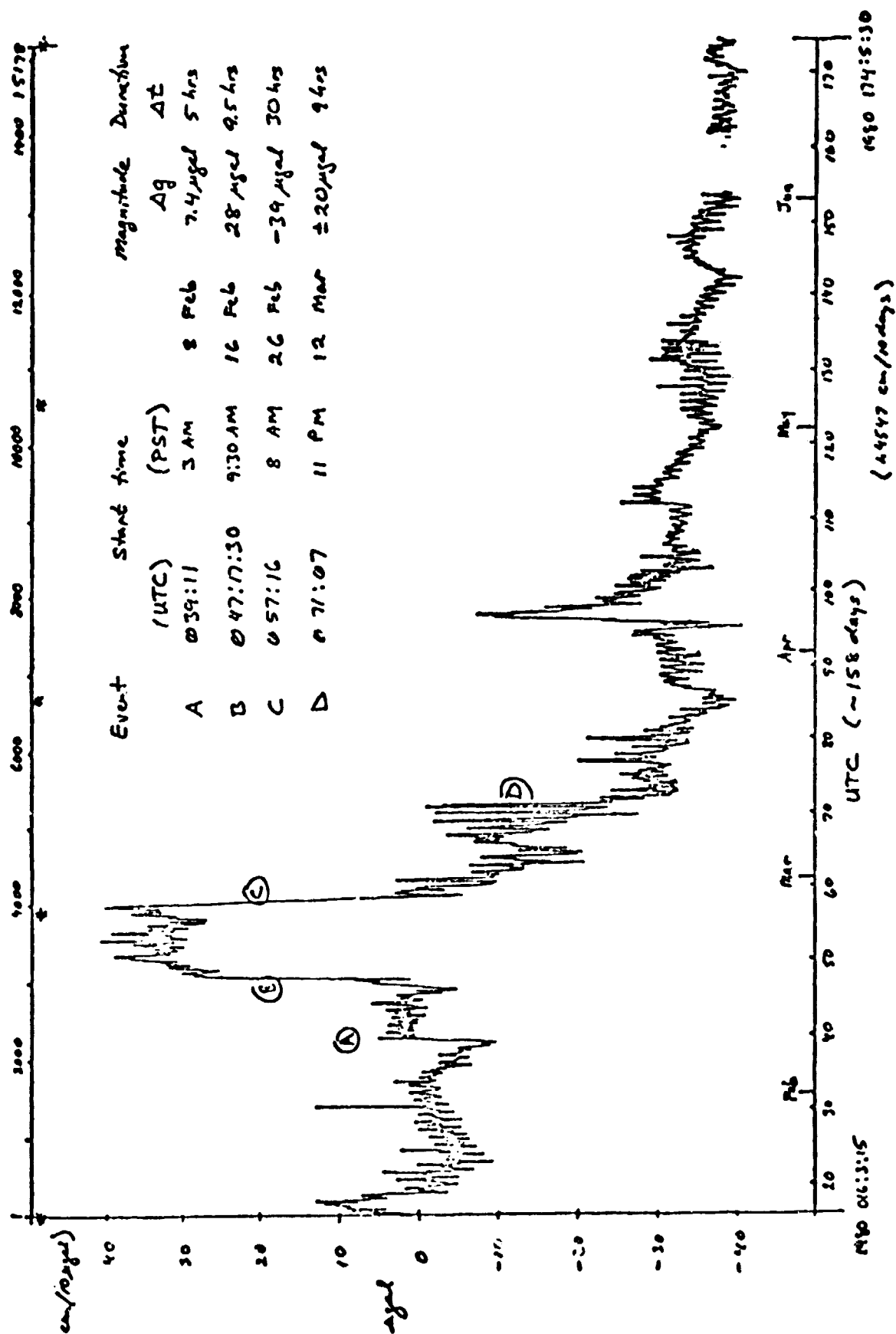
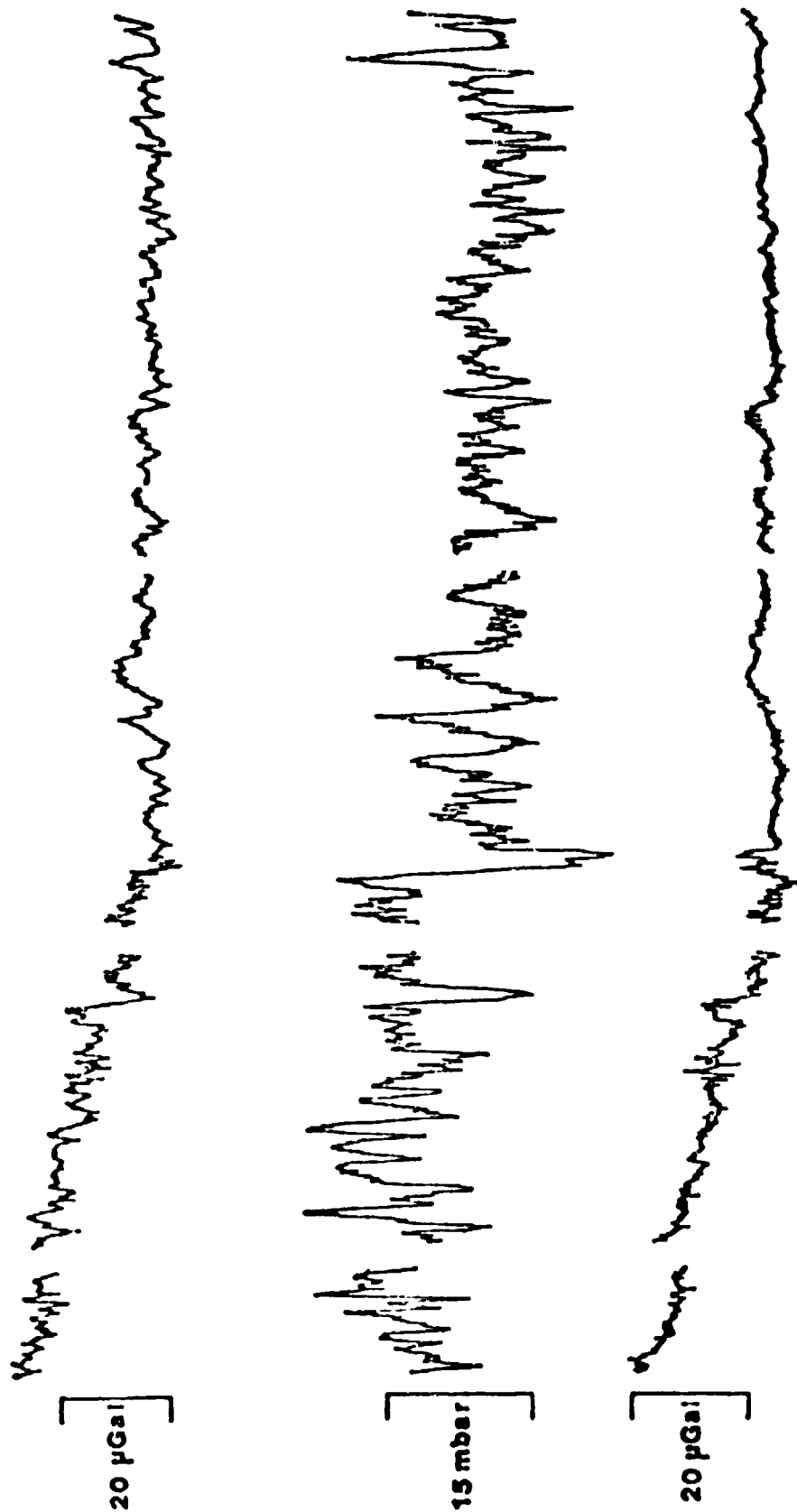


Figure 4.4 Plots of data after removal of tides and barometric effects



023 1979 302

A 279-day record from Boulder, Colorado. The top trace is gravity after removal of the tides, the second is the barometric pressure, and the third is the residual gravity after removal of the pressure effect.

Figure 4.5 Plots of data after removal of tides and barometric effects.

5.0 Earth Tide Studies

The time varying changes in the gravitational potential of the earth caused by the motions of the earth-moon-sun system give rise to the earth and ocean tides. The earth tides are in equilibrium (or nearly so) with the tide potential as the highest frequencies in that potential are far below the lowest elastic eigenfrequency of the solid earth. The laterally averaged elastic properties of the earth are well known from seismological studies and hence the earth tides on such an oceanless earth model may be readily calculated. The ocean tides, in contrast, are nonequilibrium tides as the ocean basins resonate near tidal frequencies. These ocean tides load the earth's surface and cause significant perturbations in the observed earth tides. If the ocean tides were well known, it would be an easy matter to calculate these perturbations as the response of a laterally averaged earth model to such surface loads is known (Farrell, 1972a). Unfortunately, such is not the case. The global ocean tides are not well known nor easy to measure except along coasts.

A second class of perturbations on theoretical earth tides arises from the departure of the earth from radial symmetry. The effects of geology (i.e. changes in rock type and hence elastic parameters), topography, and underground vaults if the instruments are placed therein, are all observable in the analysis of the tides of the real earth. Further, if temporal changes in elastic characteristics take place, as has been suggested to occur prior to earthquakes, then the perturbations on the earth tides due to these changes may be observed.

Our studies of the earth tides then are centered in three areas:

1. The ocean tides--improving and constraining global ocean tide models.
2. Developing three-dimensional models of the elastic structure around tidal observatories.
3. Investigating the temporal stability of nearby elastic structure and its connection with the seismotectonics of the area.

The response of the three basic kinds of instruments used to study the earth tides can be characterized as follows:

1. Gravimeter or vertical accelerometer. This instrument responds to both vertical acceleration and, due to the earth's vertical gravity gradient, to vertical displacement. The tidal vertical acceleration is predominantly due to the direct lunar attraction. On a perfectly rigid earth, this is all that would be observed. On an elastic earth, however, there is an additional effect that amounts to some 16 percent of the direct attraction and is additive. Thus the "gravimetric factor" is 1.16.

The response of a gravimeter to surface mass loads likewise arises from the direct Newtonian attraction of the mass and from the vertical displacement at the observing point caused by the surface load. Figure 5.1 (after Farrell, 1973) illustrates the relative importance of these two effects as a function of distance from the load. They are equal at about 3° (330 km) and at greater distances, the direct attraction dominates, falling off like r^{-1} .

2. The tiltmeter or horizontal accelerometer. This instrument responds to both horizontal acceleration and tilt relative to the local vertical. In the case of the earth tides these effects are in opposition with the tilt (a result of the earth's elasticity) being about 30 percent of the direct effect. Thus the diminishing "tilt factor" is about 0.7. The response to surface mass loads is dominated near the source by the elastic or surface tilt part of the response. At about 5° (500 km) it equals the direct Newtonian attraction. However, the ratio of the horizontal Newtonian attraction to the vertical Newtonian attraction varies like

$$\frac{N_z}{N_r} = -\tan(\theta/2)$$

so that at, say, 5° $N_z = .04 N_r$ and thus the tilt is about 25 times the gravity perturbation. Close to the source, the ratio of total gravity perturbation to total tilt is even smaller and in fact the tilt perturbation is almost solely due to the slope of the surface.

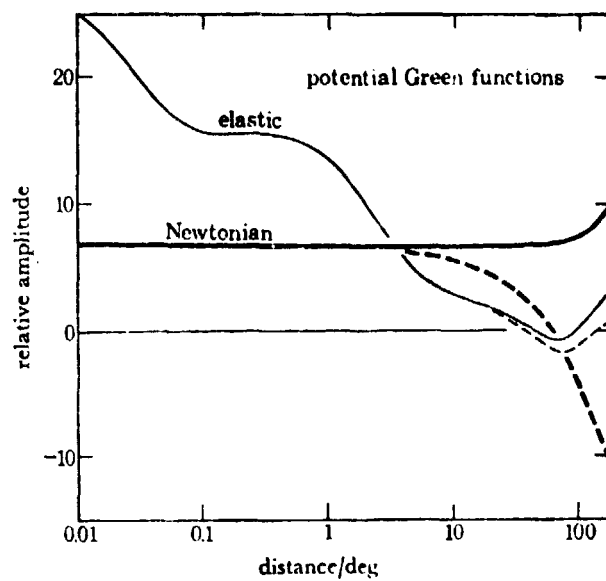


Figure 5.1 The elastic and Newtonian parts of the gravitational potential Green function. The amplitudes have been multiplied by $(a\theta/g) \times 10^{12}$ (a is 6.371×10^6 m, θ is distance in radians, g is 9.8 m s^{-2}) to give relative amplitudes.

3. The strainmeter. This instrument is a linear extensometer, measuring changes in length, ΔL along some base length L . Its response to the tidal potential is controlled solely by the elastic behavior of the earth for if the earth were perfectly rigid there would be no change in length. Lacking the direct effect, the strain tides are thus an order of magnitude smaller than either the tilt or gravity tides. This lack of direct response to gravitational potential attraction may be deemed an advantage if one wishes to study the elastic structure of the earth, as its response to surface mass loads is also purely elastic.

5.1 The Ocean Tides

We believe that precision measurements of the body tides made with calibrated low noise instruments such as the super-conducting gravimeter and the laser strainmeters can significantly contribute to the modeling of the global ocean tides. Both these instruments are well calibrated, the gravimeter to better than 1/2 percent, and the strainmeters by their nature as fringe counting interferometers. It has been demonstrated that they both are limited by only earth noise in the tidal band (Warburton *et al.*, 1975, Berger and Levine, 1974).

As a first effort along these lines we have calculated the theoretical gravitational load tides of two major tidal constituents, M_2 (principal lunar semi-diurnal) and O_1 (principal lunar diurnal) for comparison with the observed tidal gravity signal at La Jolla and Pinyon Flat. These constituents were chosen because they have the best known global distributions, they are well removed in frequency from the effects of radiational tides, and there are no predicted anomalies in the earth tide admittance due to core resonance at these frequencies.

The load tides were calculated by convolving Farrell's Gutenberg-Bullen A gravity load Green's functions (Farrell 1972) with theoretical models of the M_2 and O_1 global ocean tide distribution taken from Hendershott and Munk (1970) and Tiron *et al.* (1967) respectively. These global tide models are numerical solutions of the Laplace Tidal Equations (LTE) using coastal observations as boundary conditions. The models are in general agreement with the few existing deep ocean pressure observations (see for example Munk *et al.* 1970) and island observations. However, the predicted tides in some areas are at variance with the known ocean tide distributions, mainly because significant features in the ocean bottom topography cannot be described in sufficient detail on the coarse finite difference grids (4° to 6°) used in the calculations. Smaller errors also arise because the theoretical results represent incomplete solutions of the LTE, and because the gravitational self-attraction of the tidal water mass has been ignored. More recent attempts (Farrell 1973, Hendershott 1972) to include these factors in the calculations are inconclusive due to a numerical error.

Fortunately, the ocean load tide in southern California is dominated by the tide in the northeast Pacific Ocean. In this area regional models for the M_2 and O_1 tides based on coastal and ocean bottom pressure gauge observations have been developed by Munk *et al.* (1970). Their results were used to modify the M_2 and O_1 global tide models in the north Pacific Ocean. The modifications to the O_1 model are minor because the Tiron, *et al.* chart is in good (perhaps fortuitous) agreement with the observations, Figure 5.2b. The modification of Hendershott's M_2 cotidal chart was, however, more drastic and involved moving his amphidrome, located northwest of Hawaii, to the location proposed by Munk, *et al.* 1500 Km southwest of San Diego, Figure 5.2a.

Calculation of the global load vector is complicated, however, because the Tiron, *et al.* and Hendershott models do not conserve tidal mass. Conservation of mass is unimportant in these solutions of the LTE where a semi-permeable coastline has been used to simulate frictional energy dissipation on the continental shelves. However, for the gravity convolution, tidal mass must be conserved (Farrell, 1972b). Because the distribution of non-conserved tidal mass is not known, an artifice such as distributing this mass equally over all the oceans must be used. This mass is small ($7.01 \text{ gm/cm}^2 - 90.45^\circ$ for M_2 and $0.47 \text{ gm/cm}^2 - 28.30^\circ$ for O_1) but not negligible. In order to estimate errors incurred by this enforced mass conservation, results are presented for three different methods. In the first method the non-conserved mass is distributed uniformly over all oceans. In the second method each of the major oceans is forced to

conserve its own tidal mass. The two methods subtract significantly different tidal masses from some oceans, in particular the Indian Ocean, but the total load vectors are similar. These vectors should be compared with the results of the third method where no attempt is made to conserve mass. We have no way of determining an accurate method of mass conservation but we assume that the errors incurred by this lack of knowledge are no larger than the difference in the vectors computed by methods 1 and 2.

The observational results presented here were calculated from three sets of gravimeter data. Runs 1 and 2 were taken at La Jolla from a 54 day and 100 day record. Run 3 was taken at PFO for a 365 day period.

The complete data records were cosine tapered and Fourier analyzed to determine the observed amplitudes and phases of the O_1 and M_2 tidal constituents. An identical analysis was performed on the theoretical rigid-earth tide which was generated for the same time period as the observed data. The results of the Fourier analysis are shown in Figure 5.3. The amplitude of gravimetric factor $|\delta|$ is the ratio of the observed tidal amplitude to the theoretical amplitude and the local epoch is the phase difference between the observed and theoretical tides. The normalized amplitude $|\Delta\delta|$ and the local epoch of the "measured load vector" were calculated as the vector difference between the observed gravimetric factor δ and an assumed theoretical gravimetric factor of 1.160 with zero phase lag (at the local equilibrium potential). The amplitude of the "measured load vector" is also given in μ gal and is calculated by scaling $|\Delta\delta|$ using the local amplitude of the theoretical gravity tide of the rigid-earth.

The observational results can be compared with the theoretical load vectors and gravimeter factors computed in a number of ways. The sum of the oceanload vector and the computed earth tide, described above, should equal the measured earth tide if the ocean load model is correct, and no other effects contribute to the loading. Using the results of method 1 (conserving total mass of all oceans) the observed O_1 tide is larger than this theoretical tide by 0.15 percent at PFO and smaller by 0.10 percent at La Jolla. Using method 2 (mass of oceans conserved individually) for M_2 the observed tide is smaller by 0.20 percent at PFO and by 0.05 percent at La Jolla. These differences are within our estimated calibration error. The differences between O_1 and M_2 , however, cannot be a consequence of calibration error. The calculation by method 2 appears better than by method 1 since the latter produces discrepancies of 0.49 percent at PFO and 0.33 percent at La Jolla for M_2 . O_1 is little affected by oceans other than the north Pacific and has therefore only been calculated using methods 1 and 3.

A more revealing comparison of the small differences between observation and theory is made by comparing only the ocean load part of the tide, Figure 5.3. In the lower part of this figure the small load tide part of the total vectors (the boxed region in Figure 5.3) is illustrated in greater detail. The origin is therefore the end point of a vector representing the theoretical tide of the solid earth with gravimeter factor 1.160 and zero phase lag. The arrows represent the ocean load vectors calculated by method 1 for O_1 and method 2 for M_2 .

In general the agreement between observation and theory is excellent. The calculated phases of the O_1 load vectors are within the scatter of the data with a maximum deviation of 5° for the 54 day sections and 1° for the complete runs 1, 2, and 3. The calculated amplitudes of the O_1 load vectors fall outside the scatter of the data points and appear to be approximately 5 percent too small. For M_2 load vectors at both locations the maximum deviation between the calculated and observed phase is 8° for the 54 day sections and 3° for the full length runs. At PFO Flat both the M_2 calculated phase and amplitude are within the data scatter. However, at La Jolla the phase is outside the scatter (but only by 3°) and the amplitude is 5 to 10 percent too small. This result suggests that the ocean tide model may be inadequate for M_2 , at least in part, because of some variability in its distribution in the neighborhood of La Jolla.

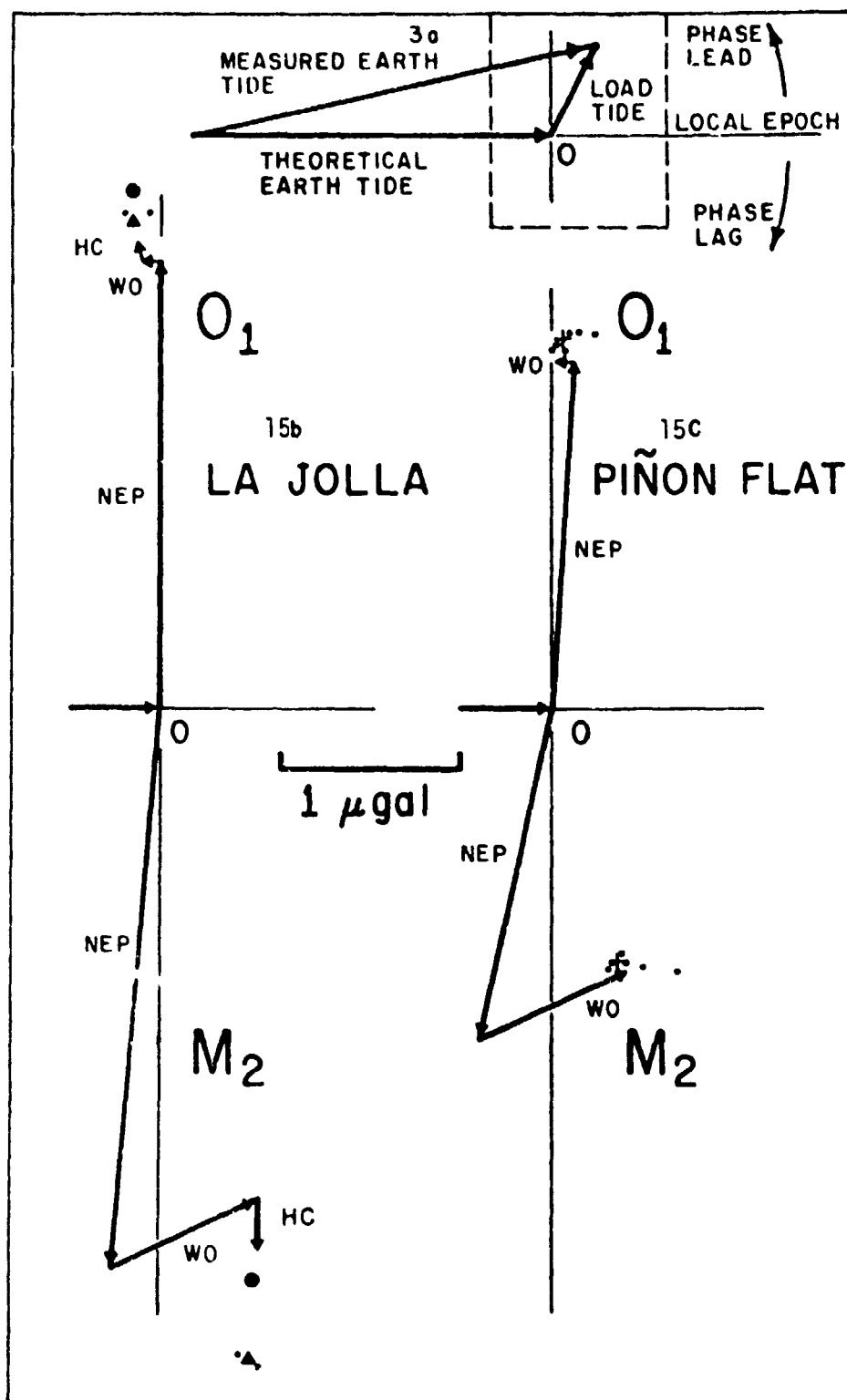


Figure 5.3 Polar plots of ocean loading part of measured and theoretical O_1 and M_2 earth tide at La Jolla and Pinyon Flat. The origin (O) is the end point of a vector representing the local theoretical tide of the solid earth with gravimetric factor 1.160 and zero phase lag. The load tide amplitude is represented by the distance from the origin to the observations (\bullet , \blacktriangle , $+$, \times) or to the tips of the theoretical load vectors. The phase lag is measured clockwise. At La Jolla \bullet is run 1, \blacktriangle is run 2, and \circ are two 54 day sections of run 2. At PFO $+$ is run 3 and \circ are six 54 day sections of run 3. The theoretical load vectors are calculated for the northeast Pacific Ocean (NEP) and for the "rest of the world oceans" (WO) which is identical at the two locations. A correction for the height above the local ocean (HC) is made only at La Jolla.

5.2 Strain Tides†

Although it is common in earth tide investigations to give tidal responses at different frequencies, comparison of these with the ocean tides is rarely attempted. Lambert (1974) suggested that gravity tides measured in Nova Scotia showed the effect of the ocean tide resonance in the Bay of Fundy. Warburton and Goodkind (1978), in a study of gravity tides at PFO, corrected their measurements for ocean loading by using frequency dependent scaling factors for tides in the north Pacific, which were deduced by Beaumont from coastal tide data; they found that employing such corrections reduced the apparent scatter in their determinations of the tidal response. For such simple scaling to work the load tides must be dominated by the effects of a few areas. The Green function for strain falls off with distance more rapidly than does that for gravity, so that strain tides recorded near a coast will be mostly affected by nearby tides while gravity measurements will not. However, records of earth strain have rarely been of sufficient quality or length to enable the tidal response to be determined at any frequencies but those of the largest diurnal and semidiurnal tide. The only expectation is the work of Levine (1978), who found that the strain tide response varied significantly across the diurnal tidal band, but only slightly across the semidiurnal band. Some of the diurnal variation could be explained by the nearly diurnal core resonance (Wahr, 1979); the rest presumably showed the frequency dependence of the ocean load. No attempt was made to explain this variation in terms of ocean tides; because the measurements were made at a mid-continental site, the load was not caused primarily by ocean tides in one area. The strain data from PFO were taken near the coast, so that ocean load signal is dominated by the load from nearby areas, and a scaling of the ocean load vector should have some chance of success.

In any kind of analysis one always wants to maximize the signal-to-noise ratio (SNR). The apparent power spectral density of a sinusoidal signal of amplitude A is $1/2A^2 T$, where T is the record length. Provided that the noise is stationary, the longest possible record will maximize the SNR. If the noise is not stationary it may be better to eliminate the noisy parts of the record, the loss of record length being more than compensated for by the decrease in noise level. Visual examination of the strain data showed enough variability in the noise level to make a further examination worthwhile.

In order to reduce the bulk of data to be processed it was decimated from an interval of 6 to 30 minutes, simultaneously lowpassing it with a filter designed (using the program of McClellan *et al.*, 1973) to have negligible ripple in the tidal bands. To analyze the resulting series it was divided into 100 day sections, overlapped so that each one started 800 hours after the next. For the estimate of the noise in the frequency band between the diurnal and semidiurnal tides not to be biased by sideband energy from the tides themselves, the data sections must be windowed before Fourier transforming (for a discussion of windowing see Harris, 1976). The 4π prolate spheroidal window of Thomson (1977) was used, which suppresses sidebands to be more than 100 dB below the main lobe. Because this window nearly eliminates data from the ends of the series, a 30 percent overlap can be used without the resulting estimates being highly correlated. A 100 day record gave enough separation between the tides that about 60 points in the power spectrum could be used to estimate the intertidal noise level. In order to extrapolate this estimate to tidal frequencies the noise power density to be proportional to f^{-2} was assumed. Though for long periods the intertidal noise level was reasonably constant, all three strainmeters showed times of high noise. Usually these episodes were at times of high drift caused by heavy rain; if the drift rate is high enough it will produce significant energy at tidal frequencies. Because the north-south instrument is most sensitive to rainfall it showed the greatest number of high-noise episodes. The northwest instrument is the least sensitive, and only 4 days of data had to be eliminated because of rain-induced drift, though 47 days were removed because of high noise produced by malfunctioning electronics. The east-west strainmeter showed much higher noise levels for the first year examined than for those following, also presumably a reflection of electronics problems.

†This section is taken from Agnew (1979).

The total length of the data series from the north-south and northwest strainmeters was 2091.4 days, and from the east-west 1926.8 days. All the series began at the same time (day 61 of 1973); the east-west series is shorter because it was very incomplete for the last 160 days of the period analyzed. Because of high noise levels, 46 days were removed from the north-south series, 400 from the east-west, and 49 from the northwest.

Figures 5.4 through 5.6 show power spectra for the three instruments. All three spectra display a roughly similar level of background noise falling off with increasing frequency as f^{-2} . Superimposed on this background are the expected strain tides and also a series of apparent tides at exactly 3, 4 . . . cycles per day (cpd). These presumably reflect temperature effects manifesting themselves as apparent strains through one of the mechanisms described in Agnew (1979). These "thermal tides" are greatest on the north-south instrument and least on the northwest, no doubt because the end buildings and part of the vacuum pipe of the latter are below ground and thus shielded from daily temperature changes. Close examination of the spectra also shows that the level of background noise is about 3 dB less on the northwest instrument than on the other two, suggesting that thermal contamination extends outside the tidal bands. Unfortunately temperature records are not available for the period of the strain data. Levine (1978) found that the strain and air pressure were coherent at periods of a week and longer. Cross-spectral analysis of the strain with a 1.5 year record of air pressure showed no coherence except at multiples of 1 cpd; this is probably a spurious correlation, owing to both the temperature tides and the atmospheric tides being caused by solar heating.

As part of their study of strain tides recorded in the United States, Beaumont and Berger (1975) computed the ocean loading effects at PFO for the O_1 and M_2 tides. We have used a slightly improved version of their computations provided by Dr. C. Beaumont (personal communication). The ocean tide models used for the Pacific Ocean off the western coast of the United States were those derived by Munk *et al.* (1970) from deep-sea measurements. For the rest of the world ocean the M_2 cotidal map of Hendershott (1972) and the O_1 map of Tiron *et al.* (1967) were used. The M_2 tide in the Gulf of California was modeled after the results of Hendershott and Speranza (1971).

Figures 5.7 through 5.9 show how well the computed and observed tidal admittances agree. In each figure, the upper part shows the admittance for the diurnal tides, the lower that for the semidiurnal tides. The complex admittances are shown as on an Argand plot; positive angles (which correspond to phase leads) are plotted counterclockwise. The phases are plotted relative to that of the tidal potential, which is the usual reference in ocean tide studies. The shear strain $e_{\theta\theta}$ is not in phase with the potential; because all three strainmeters partly respond to it none of the elastic strains (denoted by E) have zero phase. The computed ocean loads are given in actual strains for a M_2 (or O_1) tide in the ocean; to normalize these we divided by the values of the elastic strain tides, as given by a harmonic analysis of the theoretical series. We also corrected the computed load tides for the variation in harmonic amplitudes caused by slow changes in the orbital inclination of the Moon. In both figures the vector NP denotes the load tide from the area covered by Munk *et al.* (1970), GC (where present) that from the Gulf of California, and RW that from the rest of the ocean. The sum of these is the computed admittance, shown as an open square. The admittance of the observed tide is shown by a solid dot. The numbers beside these symbols are the tidal group number, the second element in the Doodson number. The O_1 tide is thus marked as -1 in the diurnal plots, and the M_2 tide as 0 in the semidiurnal plots.

It is clear that the observed and computed tides do not agree; the misfit is more apparent than it was in the results of Berger and Beaumont (1976) because the errors on the observed admittance are smaller. Berger and Beaumont discussed a number of possible sources of error, and concluded that the most likely ones were inaccuracies in the ocean tide models used and inadequacies in the representation of strain distortions by inhomogeneities. Though the total load from the oceans other than the north Pacific is small, it is made up of a number of larger and partly canceling loads, some of which, in particular that from the southeast Pacific, are

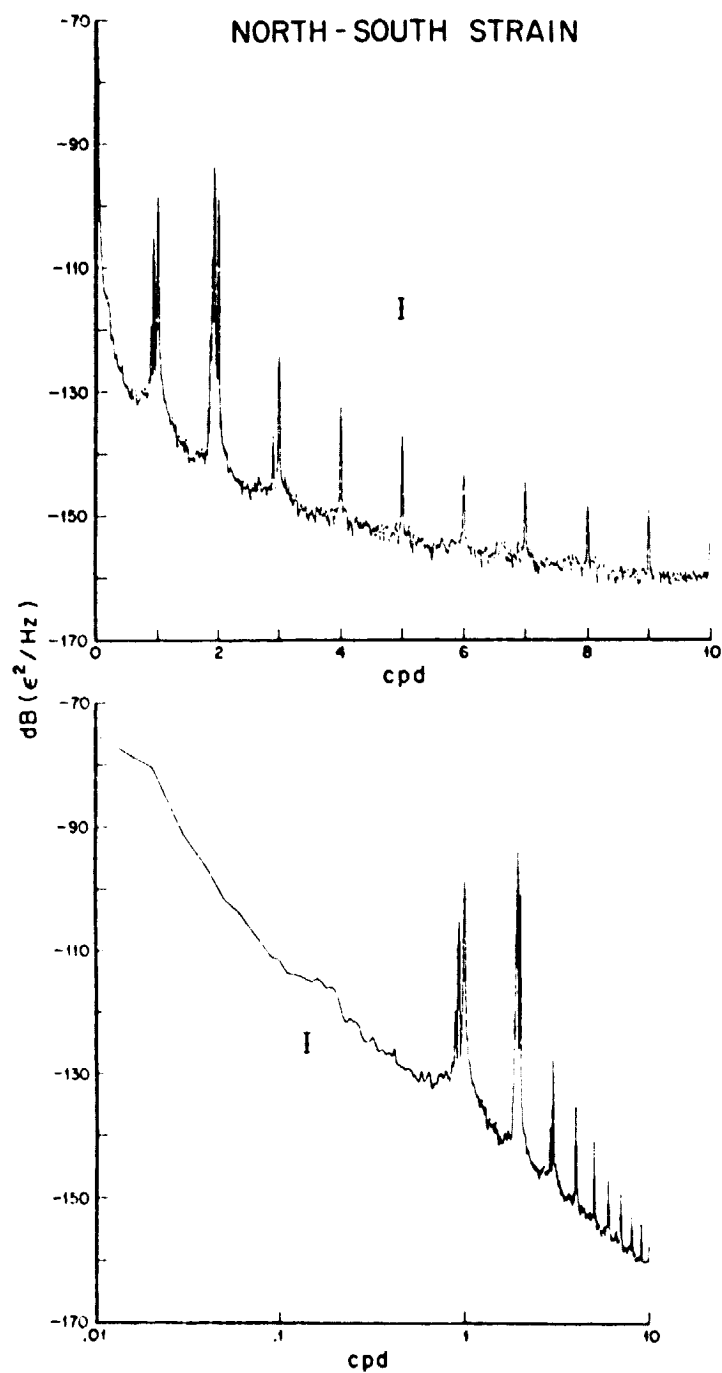


Figure 5.4 Power spectrum of north-south strain. The error bars show the 95% confidence limits on the spectral level.

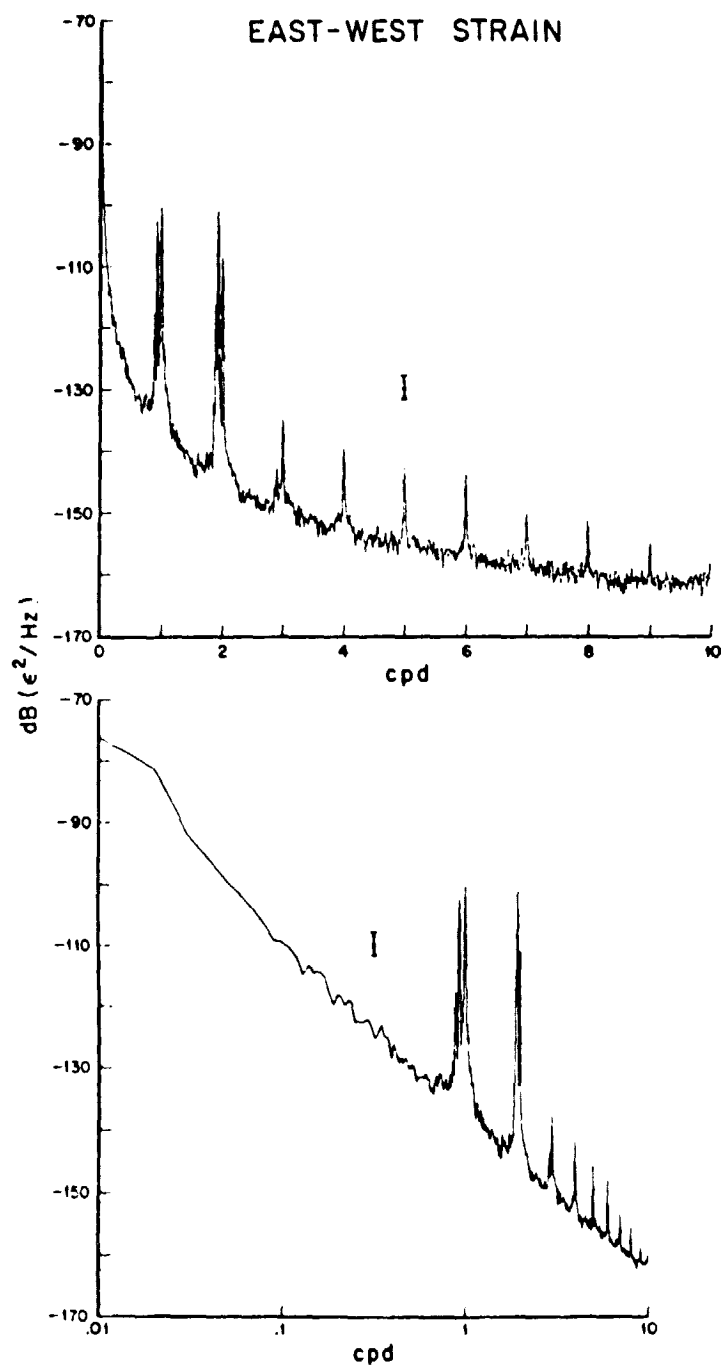


Figure 5.5. Power spectrum of east-west strain. The error bars show the 95% confidence limits on the spectral level.

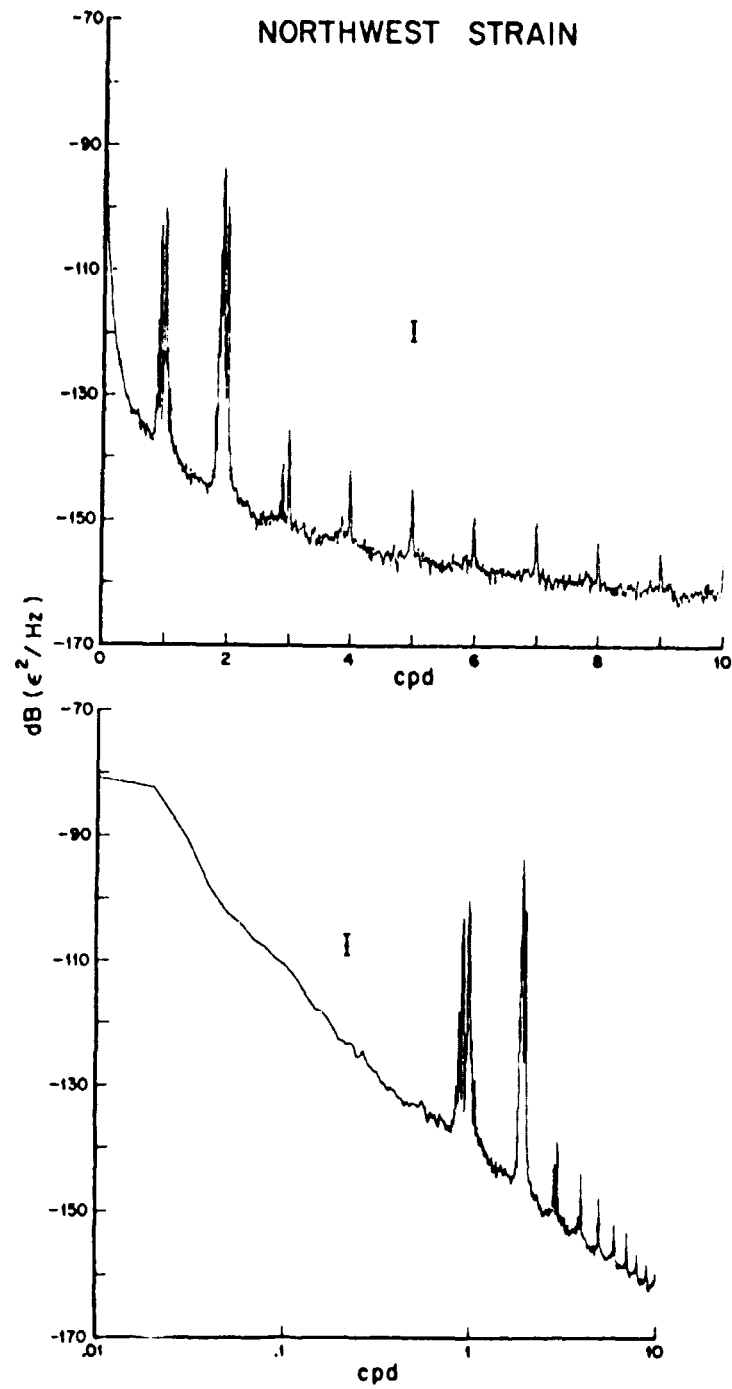


Figure S 6 Power spectrum of northwest strain. The error bars show the 95% confidence limits on the spectral level

NORTH - SOUTH

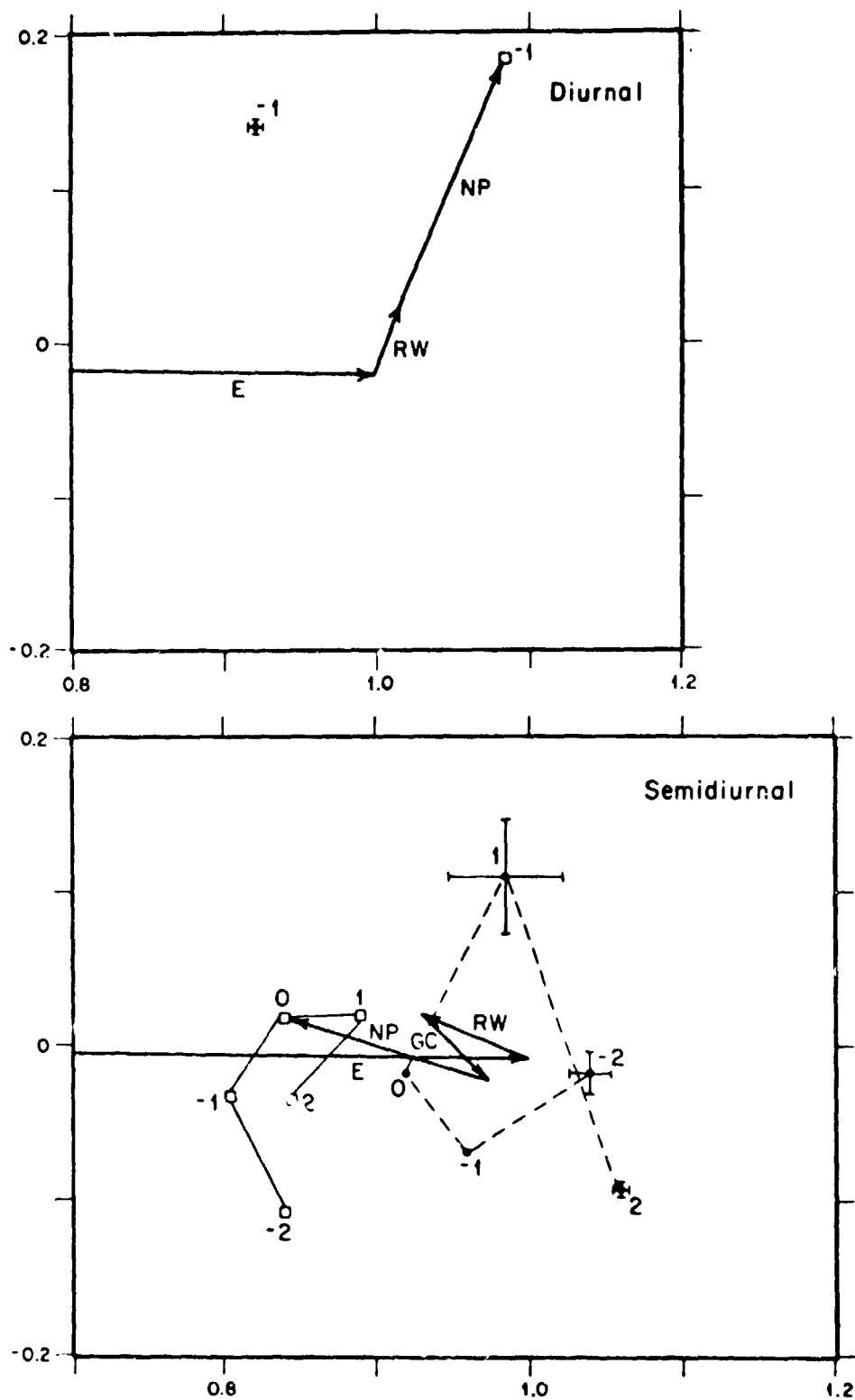


Figure 5.7 Phasor plot of north-south tidal admittance. See text for explanation.

EAST - WEST

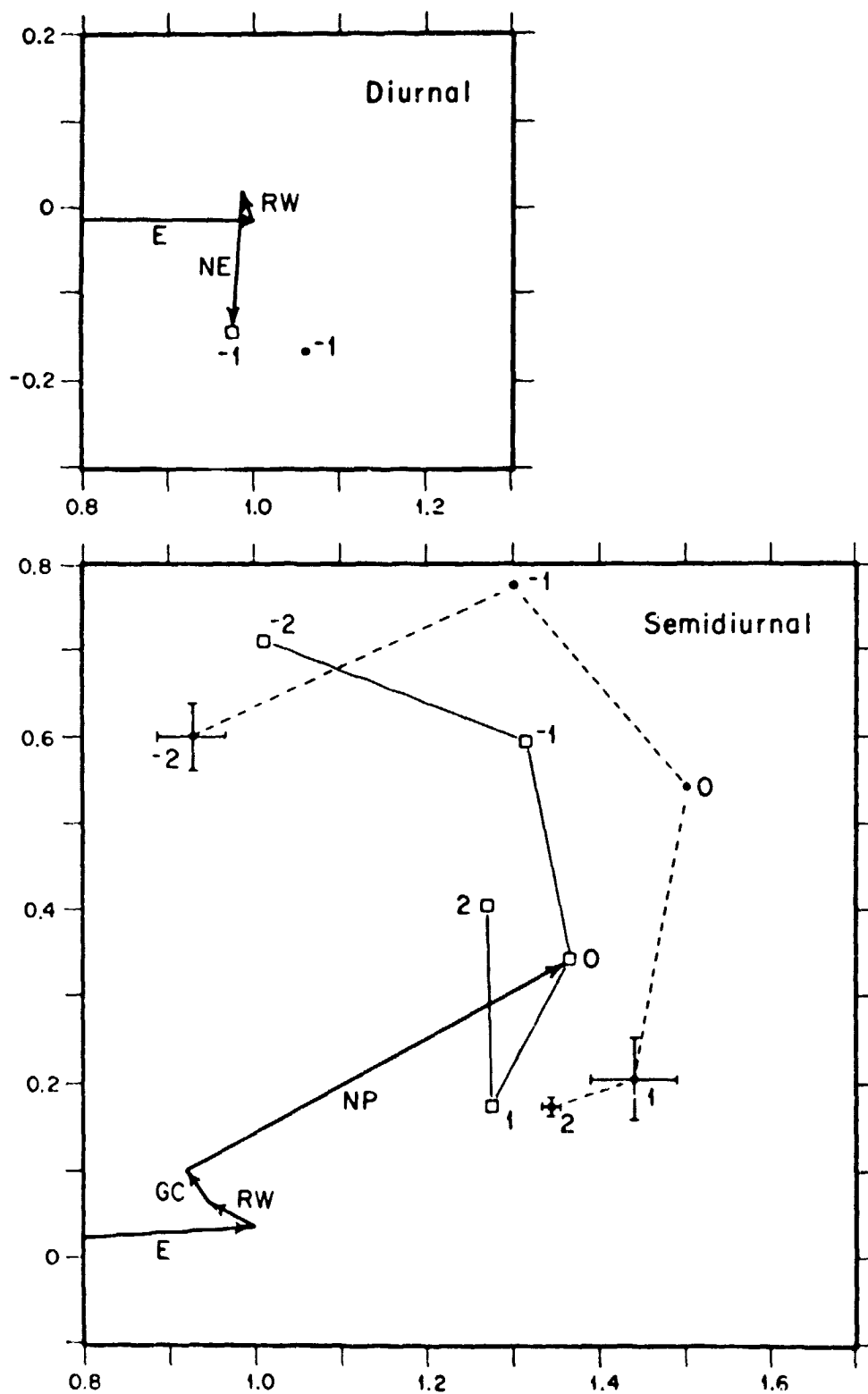


Figure 5.8 Phasor plot of east-west tidal admittance. See text for explanation.

NORTHWEST

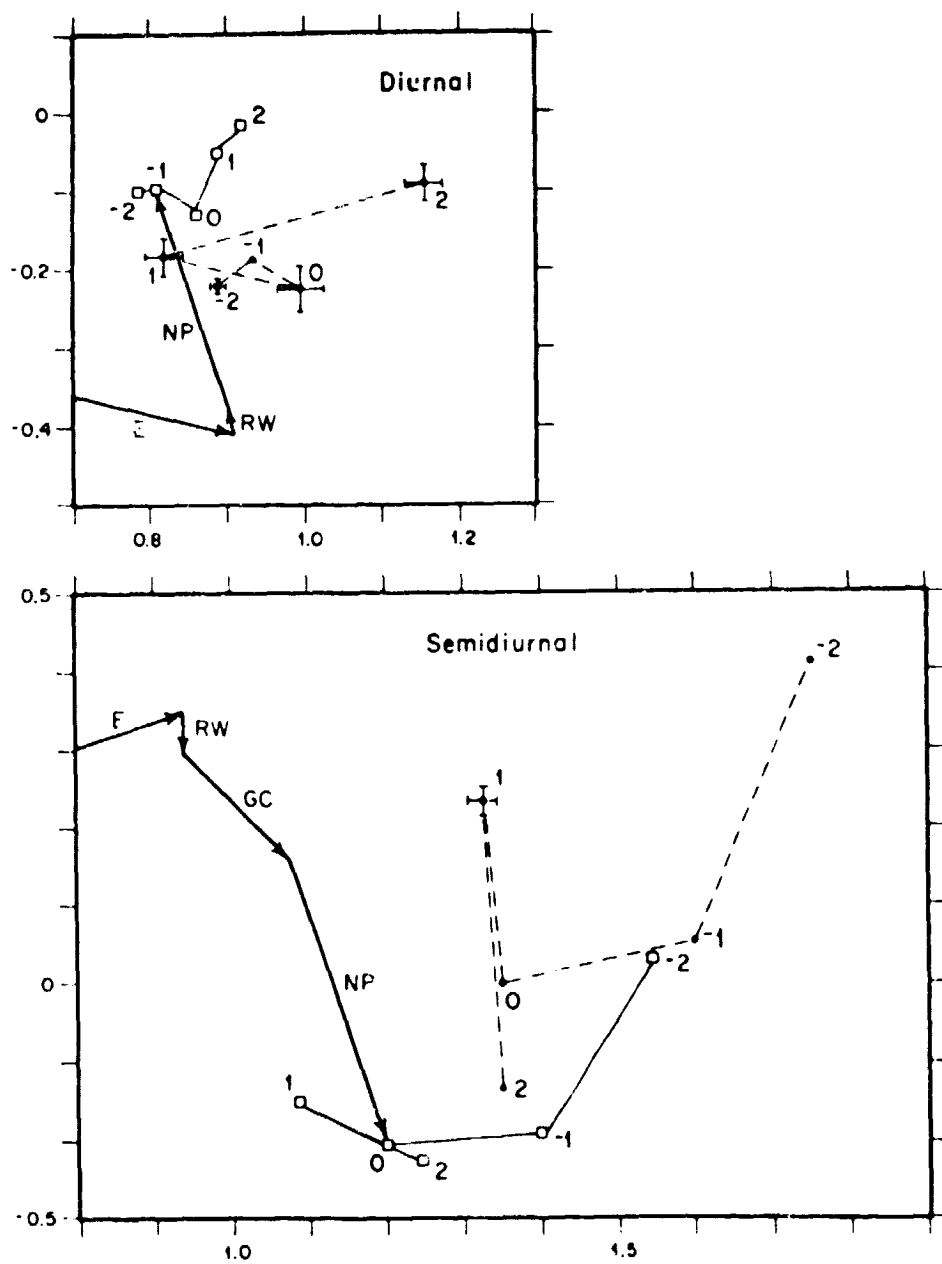


Figure 5.9 Phasor plot of northwest tidal admittance. See text for explanation.

poorly known. It is however very likely that the corrections for inhomogeneities are not in fact correct because of our ignorance of the geology underlying Pinyon Flat.

The semidiurnal plots for all three strain components, and the diurnal plot for the northwest strain, show the admittance for all groups from -2 through 2. The disagreements between observed and computed M_2 strain tides suggest that an elaborate modeling effort to explain the observed frequency variation would not be warranted. We have instead scaled the NP vector by the admittance of the ocean tide at La Jolla (relative to M_2 and O_1), as given by Cartwright *et al.* (1969); and have scaled the GC vector using some approximate factors derived from the results of Stock (1976). Table 5.1 gives the scaling factors used. The resulting computed strain tides are plotted as open squares, identified by group number. For clarity, the observed and computed points have been connected by lines.

Considering the crudeness of the method, the agreement between the frequency dependence of the observed and computed admittances is surprisingly good. The results of Munk *et al.* (1970) show that the frequency dependence of the tides at several points some distance from the coast is fairly similar to that at La Jolla. As the size of the NP vector shows, the loads from this region dominate those of the other areas. The strain tide results thus confirm that over this whole region the frequency dependence of the tidal admittance is well represented by that at La Jolla, though the growing mismatch between the curves for the tidal groups with frequencies above M_2 suggests that this is less true with increasing frequency.

5.3 Elastic Structure - Local Departures from Radial Symmetry

Since the strain tides are not in part composed of a direct effect, fractionally they are much more sensitive to local elastic conditions than are the gravity tides. Further because the strain Green's function for surface mass loads drops off like r^{-2} away from the source, while the gravity Green function attenuates like r^{-1} , strain is relatively more sensitive to "nearby" surface mass load.

Before we can deduce much about these surface mass loads, namely, the ocean tides, we must correct the observed strain tides for local departures from radial symmetry--a condition used to calculate the loading Green's Functions (Farrell, 1970).

The distortions of the strain field due to: a) topographic fluctuations of the free surface in the vicinity of the strain observatory; b) the cavities in which underground instruments are placed; and c) the lateral variations of elastic parameters caused by geological structure, are all manifestations of what may simply be termed as departures from radial symmetry. Perhaps the most obvious form of lateral heterogeneities are due to geology, but recently the other effects have begun to be fully appreciated (Harrison, 1976). The topographic effects are the most amenable to model studies simply because the topography is well known and readily available in the form of large scale topographic maps. Vault geometry in the form of three-dimensional mine workings is, in general, too complex to model practically. Our studies indicate, however, that for most underground strainmeter installations the cavity effect is small. Geological effects are perhaps the most difficult to estimate simply because the three-dimensional distribution of elastic properties is not well known. These effects, unfortunately, are not necessarily small as we will demonstrate of several simple models.

We refer to the "homogeneous applied" strain as the strain applied by the sum of the solid earth tide and the ocean load tide to a radially symmetric earth model. Conveniently, it can be thought of as the strain input to the base of the crust above which lateral variations are confined. We use the term "inhomogeneous" to describe the strains that result on the free surface of an irregular heterogeneous earth and these quantities will be denoted by the subscript /

Finite element models of lateral variations in the elastic properties of the crust and topography cannot accurately represent the total assemblage of such variations on the earth. This does not, however, prevent realistic modeling because it can be shown by analogy to Saint-Venant's principle that each inhomogeneity perturbs the strain field only within a surrounding

Table 5.1
Scaling Factors for Ocean Tides

Group	Gulf of California		Northeast Pacific	
	Amplitude	Phase (deg)	Amplitude	Phase (deg)
1 -2			1.014	5.3
1 -1			1.0	0.0
1 0			0.850	-8.5
1 1			1.111	-14.8
1 2			1.231	-20.9
2 -2	1.0	-14.	1.233	50.8
2 -1	1.0	-7.	1.250	21.5
2 0	1.0	0.	1.0	0.0
2 1	1.15	7.	0.714	-17.0
2 2	1.30	14.	0.908	11.0

region having the same characteristic dimension as the inhomogeneity. At large distances from the inhomogeneity the strain field becomes uniform. Furthermore, the length scale of the homogeneous tide is, in general, much larger than the length scale of the inhomogeneities. Consequently, a valid model is one of a region that surrounds the strainmeter subject to uniform stress, implying a uniform strain field in the absence of inhomogeneities. The region should be large enough to encompass all inhomogeneities that will modify the strain field at the strainmeter site. This model may not be valid where the strainmeters are sited very close to an ocean because local tidal loading produce a homogeneous strain field of wavelength less than or equal to that of the inhomogeneities.

A similar scale argument permits large scale structure to be separated from small scale structure in the form of a series of models. For example, the problem of a strainmeter in a mine tunnel within a large hill can be separated into two superimposable models; the large scale hill, and the smaller scale tunnel. This separation is valid if it can be shown that the stress field on each of the sub-models is uniform. This approach is essential when finite element techniques are used because models that are sufficiently large to include large scale structure yet sufficiently detailed to include small scale structure have an unmanageably large number of finite elements.

In the estimation of the topographic effects on the local strain field we consider the strain components on an irregular free surface. Thus the strain tensor is of rank one and its components may be represented vectorially. We will refer to the complex strain components in the East-North (x_1, x_2) axis system (see Figure 5.10) as the vector $\bar{\epsilon}$, where

$$e_1 = e_{11}$$

$$e_2 = e_{12}$$

$$e_3 = e_{22}$$

The real part of these complex quantities is the part that is in phase with the local equilibrium potential; the imaginary part is that lagging the equilibrium potential by 90° .

The extensions along the strainmeter directions will be referred to by the vector $\bar{\epsilon}$ where the component ϵ_1 is the extension in the direction θ_1 .

We subscript the quantities $\bar{\epsilon}$ and $\bar{\epsilon}$ with H or I to distinguish the homogeneous and inhomogeneous quantities. The results of the calculations will be $\bar{\epsilon}_I$, the topographically perturbed applied extensions.

The results of the finite element modeling of the topography at a particular station are expressed by the transformation matrices T which express the perturbation of the strain components e_H . Thus:

$$\bar{\epsilon}_I = T \bar{\epsilon}_H$$

Strain components in the unprimed coordinate system are given by

$$\bar{\epsilon} = R \bar{\epsilon}'$$

where R is the rotation matrix

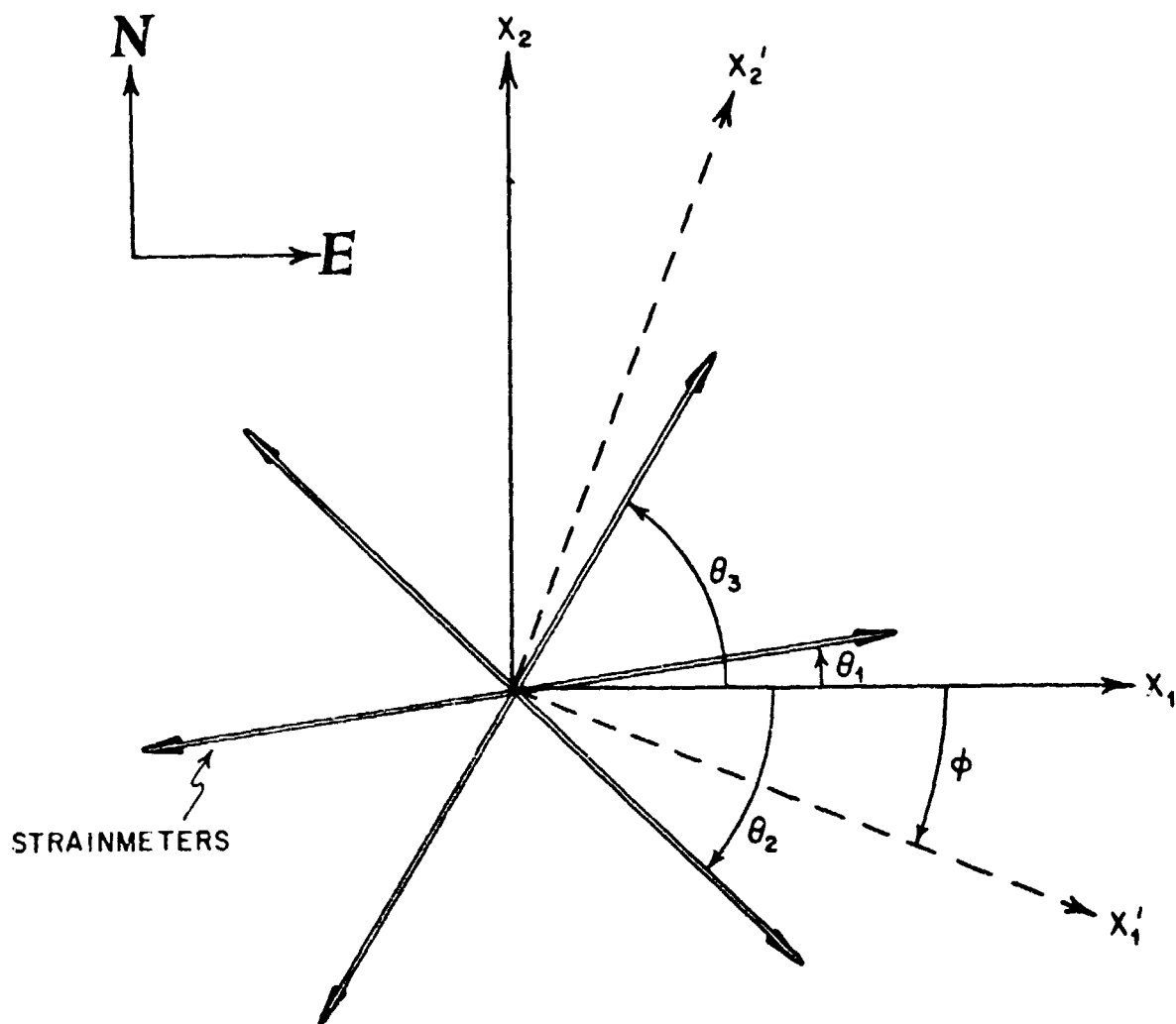
$$\begin{pmatrix} \cos^2 \phi & 2 \sin \phi \cos \phi & \sin^2 \phi \\ -\sin \phi \cos \phi & \cos^2 \phi - \sin^2 \phi & \sin \phi \cos \phi \\ \sin^2 \phi & -2 \sin \phi \cos \phi & \cos^2 \phi \end{pmatrix}$$

Then

$$\bar{\epsilon}_I = T \bar{\epsilon}_H$$

where

$$T = R T' R^{-1}$$



Coordinate System

Figure 5.10 Coordinate system for topographic effect calculations

These matrices are given in Table 5.2 for PFO. For the cases where ϕ is 0° (PFO) the rotation matrix is simply the identity matrix. For a station where there were no topographic effects the matrix \underline{T} would also be the identity matrix.

For PFO we show in Figure 5.11 how various elements of the matrix \underline{T} actually vary in space. This can give some indication when compared with local topography of good and bad sites as far as these effects are concerned.

A third matrix transformation relates the extensions $\bar{\epsilon}$ to the components of strain $\bar{\epsilon}$. That is

$$\bar{\epsilon} = \underline{C}\bar{\epsilon}$$

where

$$C = \begin{bmatrix} \cos^2 \phi_1 & 2 \sin \theta_1 \cos \theta_1 \sin^2 \theta_1 \\ \cos^2 \theta_2 & 2 \sin \theta_2 \cos \theta_2 \sin^2 \theta_2 \\ \cos^2 \theta_3 & 2 \sin \theta_3 \cos \theta_3 \sin^2 \theta_3 \end{bmatrix}$$

Thus we have the expression

$$\begin{aligned} \bar{\epsilon}_I &= \underline{C} \underline{R} \underline{T} \underline{R}^{-1} \underline{C}^{-1} \bar{\epsilon}_H \\ &= \underline{C} \underline{T} \underline{C}^{-1} \bar{\epsilon}_H \end{aligned}$$

For graphical clarity in the presentation of the final tidal phasor plots (Figure 5.12) we express the topographic perturbation effects as an additive vector.

$$\begin{aligned} \bar{\epsilon}_I &= \bar{\epsilon}_H + \bar{\epsilon}_I - \bar{\epsilon}_H \\ &= \bar{\epsilon}_H + (\underline{C} \underline{T} \underline{C}^{-1} - \underline{I}) \bar{\epsilon}_H \\ &= \bar{\epsilon}_H + \bar{P} \end{aligned}$$

where the additive perturbation vector \bar{P} is obtained by transformation on the vector $\bar{\epsilon}_H$.

5.4 Investigating the Temporal Stability

The third aspect of our earth tide studies directs itself to temporal changes in local elastic properties of the crust.

The observation of changes in the ratio of seismic velocities V_p/V_s before earthquakes led to the suggestion that in the epicentral region large changes in bulk elastic properties may take place. A theory is that V_p/V_s anomaly, which appears to be predominantly a change in V_p , is caused by dilatancy in the earthquake source region (Scholz *et al.*, 1973). Dilatancy, as observed in laboratory experiments is an inelastic volume increase of the rock under a stress near its failure point. This volumetric strain is due to the formation of micro-cracks.

We have numerically investigated the effects on the earth's tidal response due to the presence of a zone where V_p/V_s changes. We conclude that the earth's response to tilt and strain will be significantly altered by the presence of this anomalous region. Further, because the fractional change in the strain and tilt tide response is greater than the corresponding change in V_p/V_s , measurements of tilt and strain tides may provide a more sensitive indicator of dilatancy than measurements of seismic velocities.

Recent Russian results have indicated variations in the strain tide prior to an earthquake in Southern Tien Shan of magnitude of 5 at a distance of 20 km. PFO is ideally suited to such a study as it lies between the highly active San Jacinto fault and the main trace of the San Andreas fault in a region of high seismicity.

We have used an axisymmetric model of the earth to determine the changes in the North-South components of the earth tide in the vicinity of an anomalous region. The dimensions of the modeled zone, 200 km deep by 2200 km (20°) wide along the earth's surface are

Table 5.2
Topographic Transformation Matrices

Station		$T_{i1'}$	$T_{i2'}$	$T_{i3'}$	θ
Camp Elliott	$T_{1i'}$	1.035	+0.000	0.005	
	$T_{2i'}$	+0.000	1.013	0.003	-26°
	$T_{3i'}$	-0.003	0.005	1.003	
Piñon Flat	$T_{1i'}$	0.815	-0.053	-0.053	
	$T_{2i'}$	-0.053	0.923	-0.058	0°
	$T_{3i'}$	0.003	-0.063	1.023	
Piñon Flat	$T_{1i'}$	0.788		-0.053	
	$T_{2i'}$	0.002		0.020	-22°
	$T_{3i'}$	0.010		1.025	

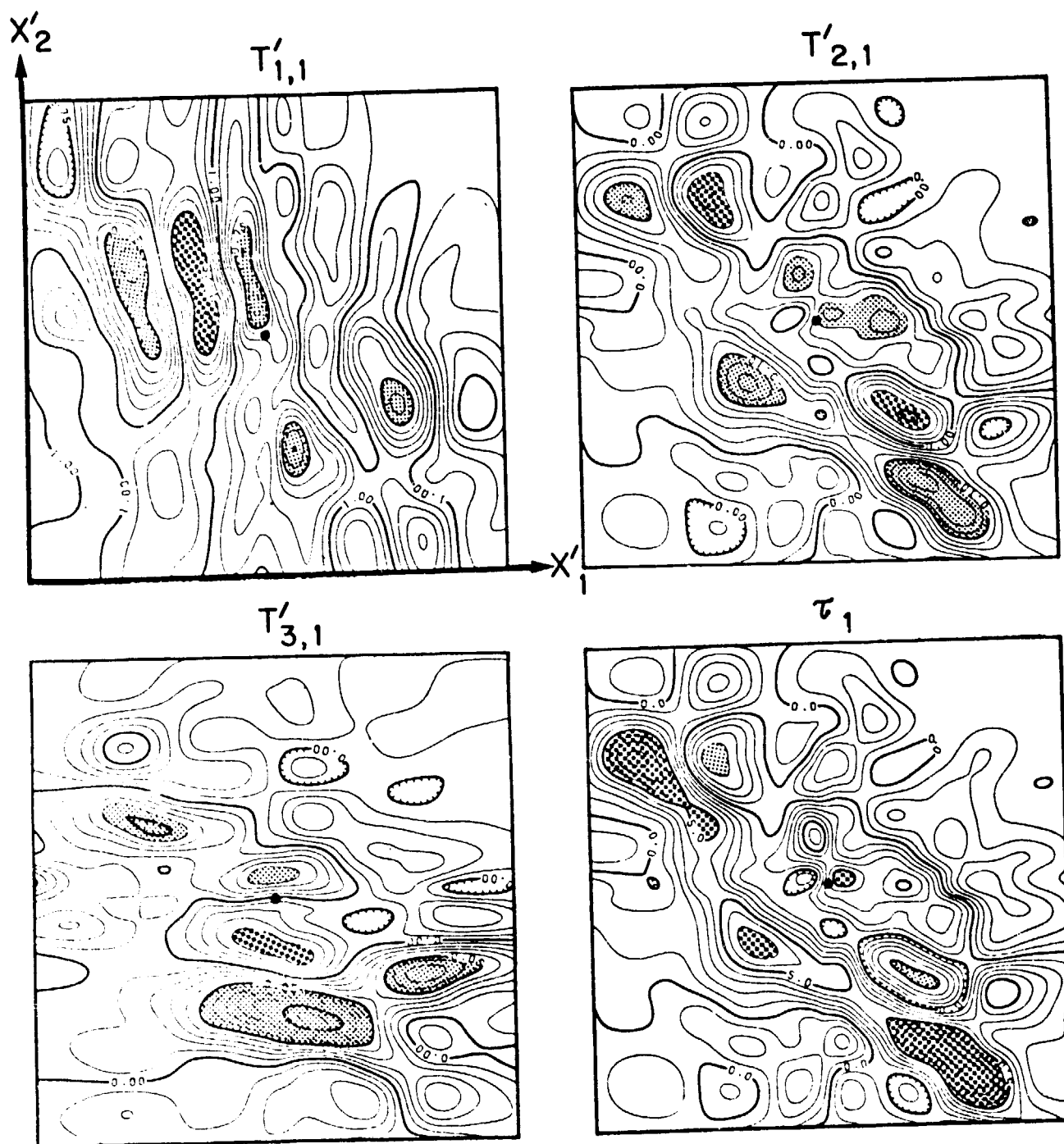
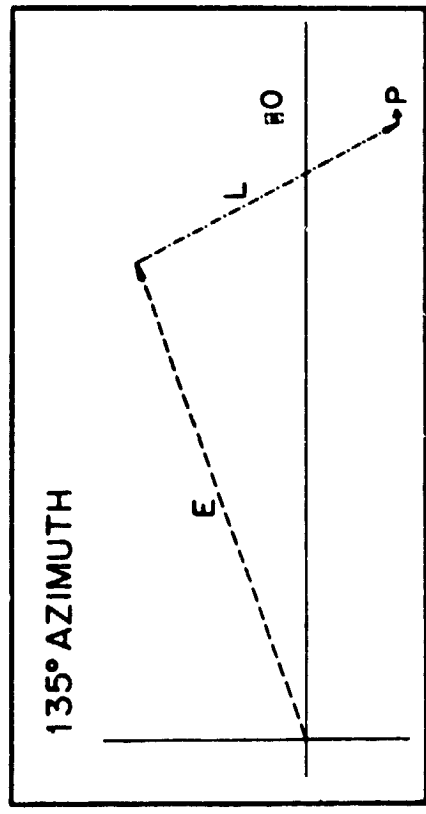
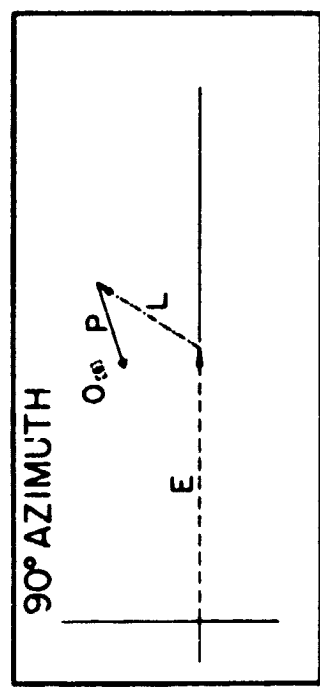
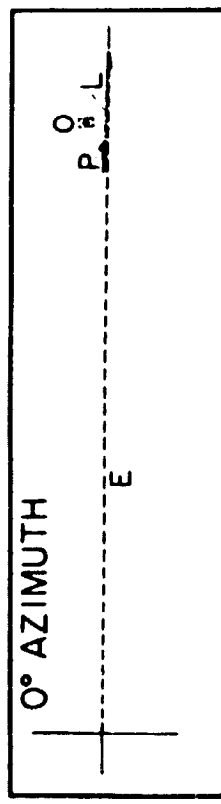


Figure 5.11 Spatial variation of topographic transformation elements.

PIÑON M_2



PIÑON O_1

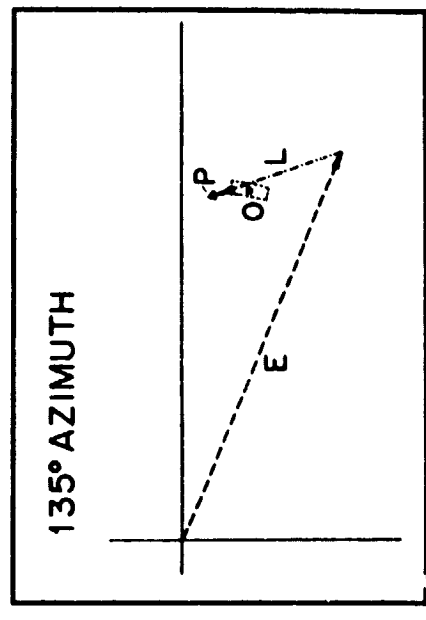
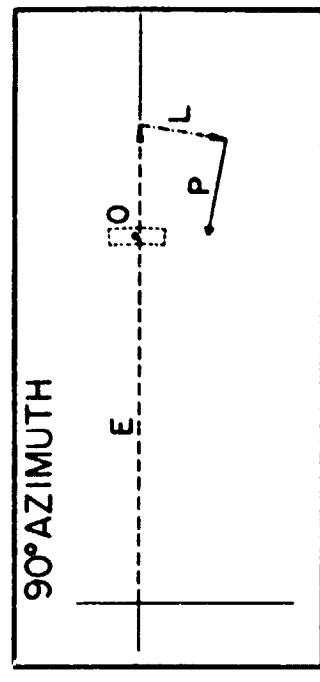
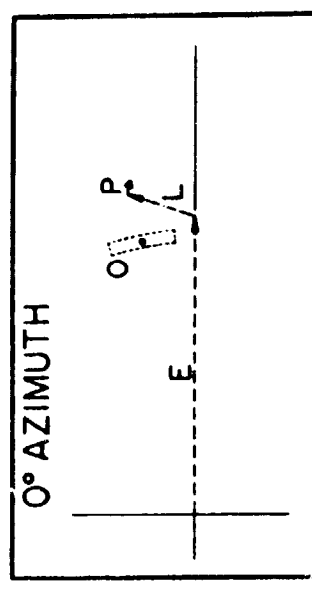


Figure 5.12 PFO (Piñon) M_2 and O_1 phasors.

chosen so that its boundaries are sufficiently distant from the anomalous region that its presence does not effect the strains at the boundaries. We use the boundary conditions appropriate to the M_2 tide on a laterally homogeneous earth. The results are strictly applicable only to the M_2 tide at latitudes 20° to 40° , however, at other latitudes and other tidal components the results are not expected to be altered significantly.

We have used the velocity variations to model Young's modulus, E , and Poisson's ratio, σ , within the anomalous region according to the relations

$$E = \frac{\rho(3V_p^2 - 4V_s^2)}{(V_p/V_s)^2 - 1}$$

$$\sigma = 0.5 \left[1 - \frac{1}{(V_p/V_s)^2 - 1} \right]$$

keeping the density, ρ , constant.

The dimensions of the anomalous region are chosen to be 20 km by 40 km but to a certain degree, the results scale with these dimensions. Further, we have determined that the exact shape and the sharpness of the boundaries do not alter the results greatly.

The finite element solution provides the radial and tangential displacements of each of the surface nodal points. These displacements are differentiated numerically by cubic spline interpolation, to give the north-south components of tilt and strain. Thus, the tilt used here is just the slope of the deformed surface. The earth-tide tilt measured by a tiltmeter is related to the gravitational potential by D , the diminishing factor. $D = (1+k-h)$ where h and k are the Love numbers. Changes in V_p/V_s will modify only the h part of the diminishing factor, that is, the slope of the Earth's surface. There will be no change in the direct acceleration and virtually no change in k as it is dependent on the deformation of the Earth as a whole and not on the small perturbations of the deformation in the anomalous region.

Figure 5.13 illustrates the results for the radial displacement and north-south components of the strain and surface tilt as a function of V_p reduction in the anomalous region. The results are normalized by the radial displacement, tilt and strain for the corresponding homogeneous model, also shown on the figure. The normalized plots represent the fractional changes in the tidal amplitudes caused by the V_p/V_s anomaly. The surface displacement anomaly is too small to be detected with a gravimeter, but both the tilt and strain anomalies will be readily detectable, as we shall demonstrate.

That the tilt and strain anomalies are both edge effects is immediately obvious. As we proceed into a dilatant region both anomalies decrease, and become undetectable toward the center of a very large homogeneous dilatant region. The strain results are particularly encouraging, suggesting that a 15 percent decrease in V_p produces a 2 percent tidal strain anomaly even at a distance of 120 km from the edge of the dilatant region. The narrower tilt anomaly is greater than 2 percent at distances less than 30 km from the boundary. The effects of smoothing the geometry, burial, or grading the velocity changes gradually are similar and result in the removal of the high spatial frequency content of the anomaly. Both the tilt and strain anomalies remain significant, however, several tens of kilometers from the boundaries.

The numerical results may be parameterized in order to relate the changes in elastic properties, due to arbitrary V_p and V_s changes, to the surface displacement, tilt, and strain anomalies calculated by the finite element models. From the results of this parametrization, we conclude that the anomaly maxima are approximately functions of one variable, the Poisson's ratio contrast, for tilt and elevation, and the $(\lambda + \mu)^{-1}$ contrast for tangential displacement and strain. Contrast means the ratio of the values of the parameter inside and outside the anomalous region, at the same depth. $(\lambda + \mu)$ is the areal strain equivalent of the bulk modulus $(\lambda + 2/3\mu)$, and is termed the "areal bulk modulus." For a 40 km \times 20 km anomalous

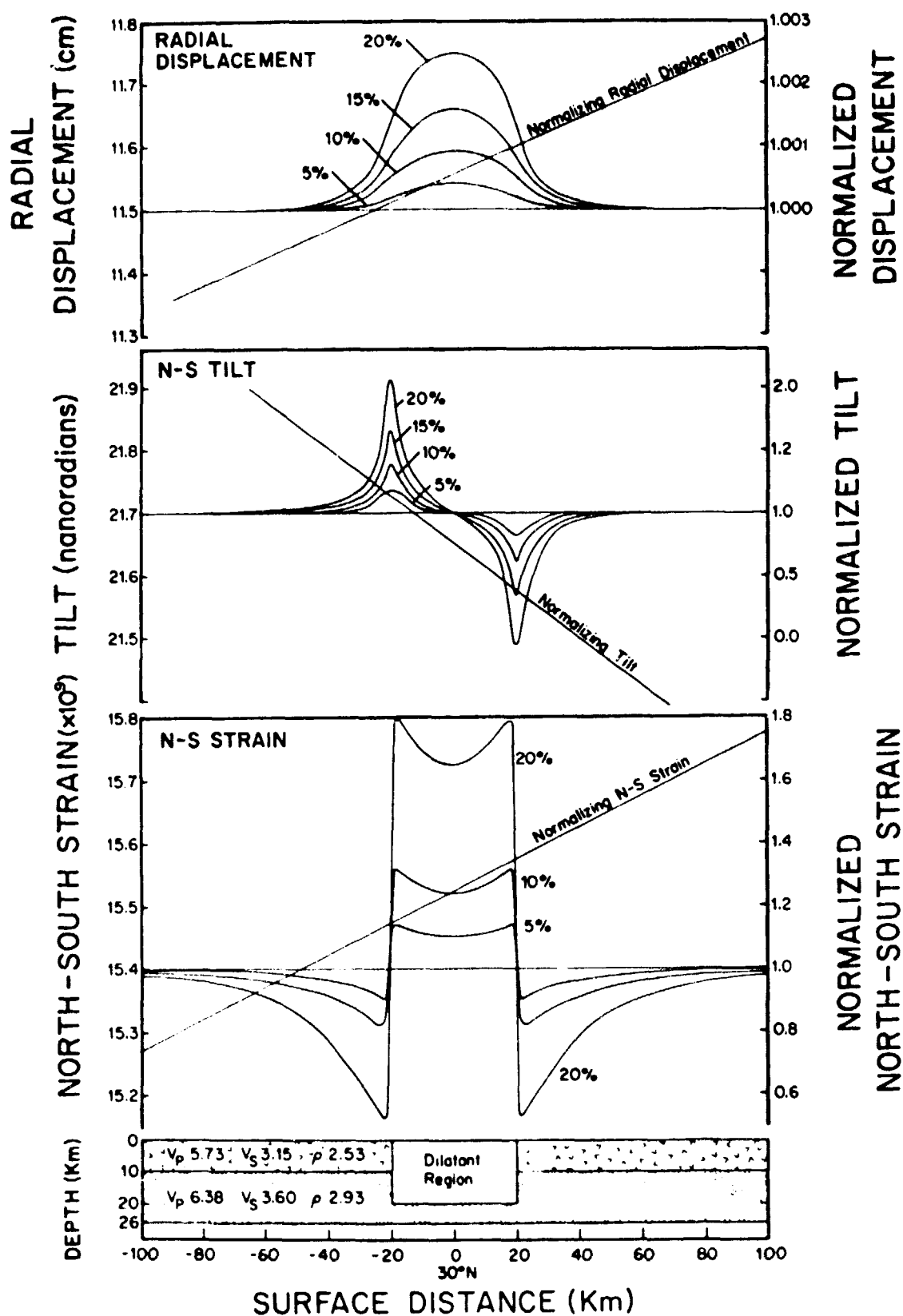


Figure 5.13 North-south components of the radial displacement, tilt and strain tide amplitude for the model shown at the bottom of the figure. Model properties below 26km follow the Gutenberg-Bullen A model. Normalizing functions are those for the same model without a dilatant inclusion. The normalized functions represent the fractional change in radial displacement, tilt and strain, as a function of position, when the P-velocity in the dilatant region is reduced by 5, 10, 15 and 20 percent.

region, we can approximately express the maximum normalized tilt anomaly as a function of the Poisson's ratio contrast $\Delta\sigma$ by

$$T_{\max} = -1.25\Delta\sigma + 2.25$$

so that when for example Poisson's ratio changes to half its normal value in the anomalous region, the maximum normalized tilt change is approximately 1.6. This means that at the edge of such a region, the North-South component of the M_2 tilt tide will be increased by 60 percent.

For the same model we calculate that the maximum normalized strain amplitude is related to the reciprocal of the areal bulk modulus, $k_a = (\lambda + \mu)$, by the expression

$$\epsilon_{\max} = 0.8\Delta \left(\frac{1}{k_a} \right) + 0.2$$

Thus, for example, if the areal bulk modulus changes by 50 percent across the boundary, the maximum normalized strain will be 1.8. This means the north-south component of the strain will be 80 percent bigger than normal.

On the basis of these calculations, Agnew (1979) has examined the strain data from the three component laser strainmeter at the PFO in an attempt either to discover significant changes in the tidal admittance that would be caused by a nearby anomalous region, or to set practical limits on the detectability of changes in the M_2 admittance.

The admittance for the m -th section analyzed was computed as

$$H_m = \frac{\sum X}{\sum Y}$$

where the sum was over harmonics. The section length, (1093 terms), tapering (Hanning), and harmonics averaged over (3, centered on M_2) were the same as were used in computing the cross-spectrum. Areas of high noise were not skipped over; as an estimate of the noise we used the average power spectral density from 1.70 to 1.78 cpd, which is the high-frequency edge of the intertidal band. The standard error of the admittance estimate is then given approximately by

$$\frac{(P_N/T)^{1/2}}{A}$$

where T is the record length, P_N the noise level, and A the amplitude of the harmonic.

The phase and amplitude of the M_2 admittance, for all the strainmeters, is plotted against time in Figure 5.14. There does not seem to have been any significant departure from the mean values for the years 1973-1980. Though the limits on the admittance vary from section to section, a change of more than 2 percent in the admittance for 6 months would probably be detectable.

Warburton and Goodkind (1978) found that the M_2 gravity tide admittance at PFO varied by about 1 part in 10^{-3} from month to month. The ocean load is about 30 percent of the northwest strain tide, and only 2 percent of the gravity tide. If the changes in the gravity tide reflected variations in the ocean load they might therefore be expected to alter the strain signal by perhaps 1.5 percent. Unfortunately the noise level is too high to rule out variations of this size, though any larger variations would conflict with the strain data.

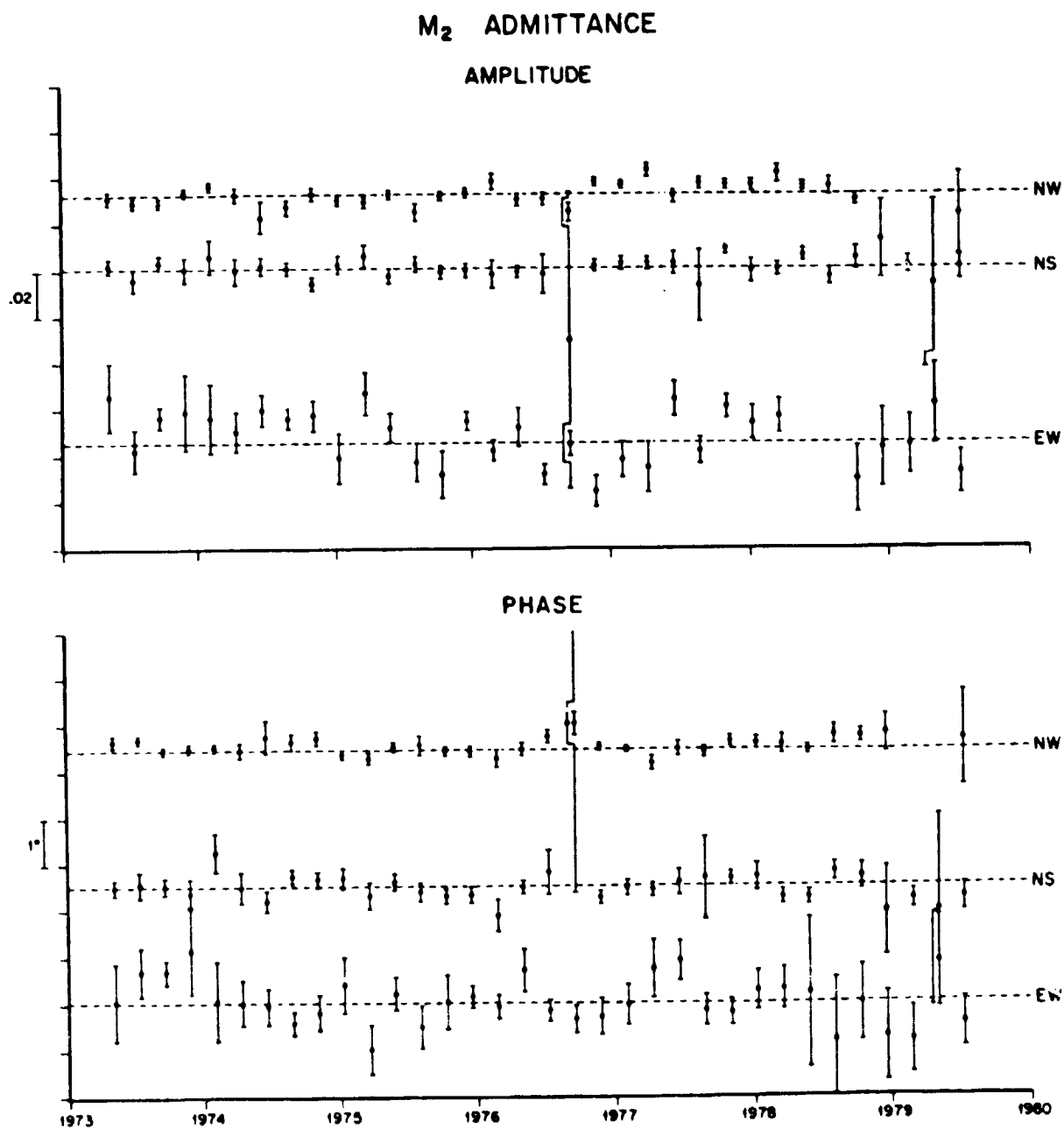


Figure 5.14 M_2 admittance as a function of time

REFERENCES

- Agnew, D.C. (1979). Strain tides at Piñon Flat: Analysis and Interpretation, Ph.D. thesis, Institute of Geophysics and Planetary Physics, University of California, San Diego.
- Allen, C.R., P. St. Amand, C.F. Richter, and J.M. Nordquist (1965). Relationship between seismicity and geologic structure in the Southern California region, *Bull. Seism. Soc. Am.* **55**, 753-797.
- Beaumont, C. and Berger, J. (1975). An analysis of tidal strains from the United States of America: I. The laterally homogeneous tide, *Bull. Seism. Soc. Am.* **65**, 1613-1629.
- Berger, J. and Beaumont, C. (1976). An analysis of tidal strain observations from the United States of America: II. The inhomogeneous tide, *Bull. Seism. Soc. Am.*, **66**, 1821-1846.
- Berger, J. and Levine, J. (1974). Spectrum of earth strain from 10^{-8} to 10^2 Hz, *J. Geophysical Res.* **79**, 1210-1214.
- Berger, J. and Lovberg, R.H. (1969). A laser earth strain meter, *Rev. Sci. Instr.* **40**, 12.
- Berger, J. and Lovberg, R. (1970). Earth strain measurements with a laser interferometer, *Science* **170**, 296-303.
- Berger, J. and Wyatt, F. (1973). Some observations of earth strain tides in California, *Phil. Trans. Roy. Soc. A* **274**, 267-277.
- Birch, F. (1966). Compressibility; elastic constants in S.P. Clark, Jr., editor *Handbook of Physical Constants*, Geol. Soc. of America, Memoir 97.
- Brune, J.N., R.S. Simons, C. Rebolgar and A. Reyes (1979). Seismicity and faulting in Northern Baja California. In National Geological Society of America Field Trip Guidebook, Geological Hazards in the San Diego Area Meeting held November 5-8, 1979, San Diego, California.
- Bufe, C.G. and T.R. Toppozada (1980). California earthquakes: End to seismic quiescence, submitted to *Science*.
- Cartwright, D., Munk, W., and Zetler, B. (1969). Pelagic tidal measurements: a suggested procedure for analysis, *EOS* **50**, 472-477.
- Chavez, David, Javier Gonzalez, J.N. Brune, F. Vernon, III, R. Simons, L.K. Hutton, P. German, C.E. Johnson (1981). Mainshock location and magnitude determination using combined U.S. and Mexican data. Submitted to USGS for publication in Professional Paper on the October 15, 1979 Imperial Valley Earthquake (to be published).
- Cooke, R.U. and A. Warren (1973). *Geomorphology in Deserts*, University of California Press, Berkeley and Los Angeles.
- Crook, C.N., R.G. Mason, and P.R. Wood (1980). Geodetic measurements of horizontal deformation associated with the October 15, 1979, Imperial Valley earthquake, *Abstracts, 75th Meeting Seismological Soc. Am.*, 55.
- Farrell, W.E. (1970). Gravity tides, Ph.D. thesis, University of California, San Diego.
- Farrell, W. E. (1972a). Deformation of the Earth by surface loads, *Rev. Geophys. Space Phys.* **10**, 761-797.
- Farrell, W.E. (1972b). Global calculations of tidal loading, *Nature* **238**, 43-44.
- Farrell, W.E. (1973). Earth tides, ocean tides and tidal loading, *Phil. Trans. Roy. Soc. Lond. A* **274**, 253-259.

- Foster, J. (1976). Geology, in Ting, I. P. and Jennings, W. *Deep Canyon, a Desert Wilderness for Science*, Philip L. Boyd Deep Canyon Research Center, Palm Desert.
- Garmany, J., J.A. Orcutt, and R.L. Parker (1979). Travel time inversion: A geometric approach, *J. Geophys. Res.* **84**, 3615-3622.
- Harris, F. J. (1976). On the use of windows for harmonic analysis with the discrete Fourier transform, *IEEE Proc.* **66**, 51-83.
- Harrison, J. C. (1976). Cavity and topographic effects in tilt and strain measurement, *J. Geophysical Res.* **81**, 319-328.
- Hendershott, M. C. (1972). The effects of solid-earth deformation on global tides, *Geophysical J. Roy. Astron. Soc.* **29**, 389-402.
- Hendershott, M. and W.H. Munk (1970). Tides, *Ann. Rev. Fluid. Mech.* **2**, 205.
- Hendershott, M. C. and Speranza, A. (1971). Co-oscillating tides in long, narrow bays: the Taylor problem revisited, *Deep-Sea Research* **18**, 959-980.
- Isherwood, D. and Street, A. (1976). Biotite-induced grossification of the Boulder Creek Granodiorite, Boulder County, Colorado, *Geolog. Soc. Amer. Bull.* **87**, 366-370.
- Jahns, R.H. (1954). Geology of the Peninsular Range Province, Southern California and Baja California. in R.H. Jahns, editor, *Geology of Southern California*, Calif. Div. Mines Bull., 170, Chapter II, 29-52.
- Johnson, C.E. (1979). Seismotectonics of the Imperial Valley. Ph.D. thesis, part II, California Institute of Technology, 332pp.
- Lambert, A. (1974). Earth tide analysis and prediction by the response method. *J. Geophysical Res.* **79**, 4952-4960.
- Levine, J. (1978). Strain-tide spectroscopy, *Geophysical J. Roy. Astron. Soc.* **54**, 27-41.
- McClellan, J. H., Parks, T. W., and Rabiner, L. R. (1973). A computer program for designing optimum linear phase FIR filters, *IEEE, Trans. Audio Electroacoustics* **21**, 506-526.
- Jordan, T.H. and J.B. Minster (1978). Present-day plate motions *J. Geophys. Res.* **83**, 5331-5354.
- Munguía, L., J.N. Brune, A. Reyes, J. Gonzales, R. Simons and F. Vernon (1980). Digital seismic event recorder records and spectra for aftershocks of the November 29, 1978 Oaxaca earthquake. *Geofísica Internacional* **17**(3), 359-366.
- Munk, W., Snodgrass, F. and Wimbush, M. (1970). Tides off-shore: transition from California coastal to deep-sea waters, *Geophys. Fluid Dyn.* **1**, 161-235.
- Nava, F. Alejandro and J.N. Brune (1981a). An earthquake-explosion reversed refraction line in the Peninsular Ranges of Southern California and Baja California Norte. *Bull. Seism. Soc. Am.* (submitted).
- Nava, F. Alejandro and J.N. Brune (1981b). Source mechanism and surface wave excitation for two earthquakes in Northern Baja California, Mexico. *Geophysical Journal* (submitted).
- Prescott, W.H., J.C. Savage and W.T. Kinoshita (1979). Strain accumulation rates in western United States between 1970 and 1978, *J. Geophys. Res.* **84**, 5423-5435.
- Reichle, M. and R. Simons (1981). Recent seismicity in the Laguna Salada region, southern California and northern Baja California (in preparation).

- Reyes, A., J. Gonzalez, L. Munguía, A. Nava, F. Vernon and J.N. Brune (1980). Locations of aftershocks of the Oaxaca earthquake using smoked paper recorders and digital event recorders. *Geofísica Internacional* **19**(3), 341-358.
- Savage, J.C., W.H. Prescott, M. Lisowski, and N.W. King (1981). Strain accumulation in southern California, 1973-1980, submitted, *J. Geophys. Res.*
- Sharp, R.V. (1967). San Jacinto fault zone in the Peninsular Ranges of Southern California, *Geol. Soc. America Bull.* **78**, 705-730.
- Sharp, R.V. (1981). Variable rates of late Quaternary strike slip on the San Jacinto fault zone, southern California, *J. Geophys. Res.* **86**, 1754-1762.
- Scholz, C.H., L.R. Sykes, and Y.P. Aggarwal (1973). Earthquake prediction: A physical basis, *Science* **181**, 803-810.
- Smith, D.E. (1980). Crustal motion measurements in California (SAFE), in Earth Survey Applications Division Research Report-1979, pp3-40 to 3-42, *NASA Technical Memorandum*, 80642.
- Stock, G. (1976). Modeling of tides and tidal dissipation in the Gulf of California, Ph.D. thesis, Scripps Institution of Oceanography, University of California, San Diego.
- Strong, J. (1958). Concepts of classical optics, W.H. Freeman and Co., San Francisco.
- Suarez, F. and M. Reichle (1979). Aftershock locations of the 14 March 1979 $M = 7.6$ Petatlan, Guerrero, Mexico earthquake, (abstract) *EOS* **60**, 893.
- Thatcher, W., J.A. Hileman, and T.C. Hanks (1975). Seismic slip distribution along the San Jacinto fault zone, Southern California, and its implications, *Geol. Soc. America Bull.* **86**, 1140-1146.
- Thomson, D. J. (1977). Spectrum estimation techniques for characterization and development of WT4 Waveguide - I, *Bell Sys. Tech. Journ.* **56**, 1769-1815.
- Tiron, K. D., Sergeev, Y. and Michurin, A. (1967). Tidal charts for the Pacific, Atlantic and Indian Oceans, (transl.), *Vestn. Leningr. Univ. Ser. Geol. i Geogr.* **24**, 123-135.
- Wah, J. M. (1979). The tidal motions of a rotating, elliptical, elastic and oceanless Earth, Ph.D. thesis, University of Colorado.
- Wahrhaftig, C. (1965). Stepped topography of the southern Sierra Nevada, California, *Geol. Soc. Am. Bull.* **76**, 1165-1190.
- Warburton, R. J., Beaumont, C. and Goodkind, J. M. (1975). The effect of ocean tide loading on tides of the solid Earth observed with the superconducting gravimeter, *Geophysical J. Roy. Astron. Soc.* **43**, 707-720.
- Warburton, R. and Goodkind, J. (1978). Detailed gravity-tide spectrum between one and four cycles per day, *Geophysical J. Roy. Astron. Soc.* **52**, 117-136.
- Wyatt, F. (1982a). Displacements of surface monuments-Horizontal motion, *J. Geophys. Res.* (in press).
- Wyatt, F. (1982b). Distant deformation from the Imperial Valley, California, earthquake 1979, *Bull. Seism. Soc. Am.* (submitted).
- Wyatt, F., Beckstrom, K., Berger, J. (1982). The optical anchor - A geophysical strainmeter, *Bull. Seism. Soc. Am.* (submitted).

List of Papers Supported by NASA 05-009-246

- Agnew, D. (1981). Nonlinearity in rock: evidence from earth tides, *J. Geophys. Res.* **86**, 3969-3978.
- Agnew, D. and K. Sieh (1978). A documentary study of the felt effects of the great California earthquake of 1857, *Bull. Seism. Soc. Am.* **68**, 1717-1729.
- Albores, A., A. Reyes, J.N. Brune, J. Gonzalez, L. Garcelazo, F. Suarez (1978). Seismicity studies in the region of the Cerro Prieto geothermal field, Proceedings of the First Symposium on the Cerro Prieto Geothermal Field, September 20-22, 1978, San Diego, California.
- Beaumont, C. and J. Berger (1974). Earthquake prediction: Modification of the earth tide tilts and strains by dilatancy, *Geophys. J. R. astr. Soc.* **39**, 111-121.
- Beaumont, C. and J. Berger (1975). An analysis of tidal strain observations from the United States of America: I. The laterally homogeneous tide, *Bull. Seism. Soc. Am.* **65**, 1613-1629.
- Berger, J. (1973). Applications of laser techniques to geodesy and geophysics, *Advan. Geophys.* **16**.
- Berger, J. and C. Beaumont (1974). Precision tidal spectroscopy for earthquake prediction, *Proc. of the Uzbek Academy of Sciences, Tashkent, USSR*.
- Berger, J. and C. Beaumont (1975). An analysis of tidal strain observations from the United States of America: II. The inhomogeneous tide, *Bull. Seism. Soc. Am.* **66**, 1821-1846.
- Berger, J. and J. Levine (1974). The spectrum of earth strain noise for 10^{-8} Hz to 10^2 Hz, *J. Geophys. Res.* **79**, 1210-1214.
- Berger, J. and F. Wyatt (1973). Some observations of earth strain tides in California, *Phil. Trans. Roy. Soc. A* **274**, 267-277.
- Brune, J.N., M. Hernandez, J. Gonzalez, L. Munguia, R. Simons, F. Suarez and F. Vernon (1980). Digital seismic event recorders: Description and examples from the San Jacinto fault, the Imperial fault, the Cerro Prieto fault and the Oaxaca, Mexico subduction fault, *Bull. Seism. Soc. Am.* **70**, 1395-1408.
- Hartzell, S.H. and J.N. Brune (1977). Source parameters for the January, 1975 Brawley-Imperial Valley earthquake swarm, *PAGEOPH* **115**, 333-355.
- Hartzell, S. and J.N. Brune (1979). The Horse Canyon earthquake of August 2, 1975 — Two stage stress release process in a strike-slip earthquake, *Bull. Seism. Soc. Am.* **69**, 1161-1173.
- Munguia, L., M. Reichle, A. Reyes, R. Simons, J.N. Brune (1977). Aftershocks of the 8 July 1975 Canal de las Ballenas, Gulf of California, earthquake, *Geophys. Res. Lett.* **4**.
- Nava, F.A. and J.N. Brune (1981). An earthquake-explosion reversed refraction line in the Peninsular Ranges of southern California and Baja California Norte, *Bull. Seism. Soc. Am.* (submitted).
- Nava, F.A. and J.N. Brune (1981). Source mechanism and surface wave excitation for two earthquakes in northern Baja California, Mexico, *Geophys. J. R. astr. Soc.* (submitted).
- Reichle, M. and R. Simons (1981). Recent seismicity in the Laguna Salada region, southern California and northern Baja California (in preparation).
- Reyes, A., J.N. Brune and C. Lomnitz (1979). Source mechanism and aftershock study of the Colima, Mexico earthquake of January 10, 1973, *Bull. Seism. Soc. of Am.* **69**, 1819-1840.

- Warburton, R.J., C. Beaumont and J.M. Goodkind (1975). The effect of ocean tide loading on tides of solid earth observed with the superconducting gravimeter, *Geophys. J. R. astr. Soc.* **43**, 707-720.
- Warburton, R.J. and J.M. Goodkind (1976). A search for evidence of a preferred reference frame, *Astrophysical Journal* **208**, 881-886.
- Warburton, R.J. and J.M. Goodkind (1977). The influence of barometric pressure variations on gravity, *Geophys. J. R. astr. Soc.* **48**, 281-292.
- Warburton, R.J. and J.M. Goodkind (1978). Detailed gravity-tide spectrum between one and four cycles per day, *Geophys. J. R. astr. Soc.* **52**, 117-136.
- Wyatt, F. (1982a). Displacements of surface monuments — Horizontal motion, *J. Geophys. Res.* (in press).
- Wyatt, F. (1982b). Distant deformation from the Imperial Valley, California, earthquake 1979, *Bull. Seism. Soc. Am.* (submitted).
- Wyatt, F. K. Beckstrom, and J. Berger (1982). The optical anchor — A geophysical strainmeter, *Bull. Seism. Soc. Am.* (submitted).
- Wyatt, F. and J. Berger (1980). Investigation of crustal tilts using shallow borehole tiltmeters, *J. Geophys. Res.* **85**, 4351-4362.